Universidade de São Paulo
Instituto de Física

Modos parafermiônicos em sistemas de elétrons correlacionados

Raphael Levy Ruscio Castro Teixeira

Orientador: Prof. Dr. Luis Gregório G. de V. Dias da Silva

Tese de doutorado apresentada ao Instituto de Física da Universidade de São Paulo, como requisito parcial para a obtenção do título de Doutor(a) em Ciências.

Banca Examinadora:
Prof. Dr. Luis Gregório G. de V. Dias da Silva - Orientador (Instituto de Física - USP)
Prof. Dr. Eduardo Miranda (UNICAMP)
Prof. Dr. Eric de Castro e Andrade (IFUSP)
Prof. Dr. Fernando Iemini de Rezende Aguiar (UFF)
Prof. Dr. Thomas L. Schmidt (Luxembourg University)

São Paulo
2023

FICHA CATALOGRÁFICA
Preparada pelo Serviço de Biblioteca e Informação
do Instituto de Física da Universidade de São Paulo

Teixeira, Raphael Levy Ruscio Castro

Modos parafermiônicos em sistemas de elétrons correlacionados. São Paulo, 2022.

Tese (Doutorado) – Universidade de São Paulo. Instituto de Física. Depto. de Física dos Materiais e Mecânica.

Orientador: Prof. Dr. Luis Gregório Godoy de Vasconcellos Dias da Silva

Área de Concentração: Física.

Unitermos: 1. Fisica da matéria condensada; 2. Sistema quântico; 3. Física computacional.

USP/IF/SBI-82/2022

University of São Paulo
Physics Institute

Parafermionic modes in correlated electron systems

Raphael Levy Ruscio Castro Teixeira

Supervisor: Prof. Dr. Luis Gregório G. de V. Dias da Silva

Thesis submitted to the Physics Institute of the University of São Paulo in partial fulfillment of the requirements for the degree of Doctor of Science.

Examining Committee:
Prof. Dr. Luis Gregório G. de V. Dias da Silva - Supervisor (IFUSP)
Prof. Dr. Eduardo Miranda (UNICAMP)
Prof. Dr. Eric de Castro e Andrade (IFUSP)
Prof. Dr. Fernando Iemini de Rezende Aguiar (UFF)
Prof. Dr. Thomas L. Schmidt (Luxembourg University)

São Paulo
2023

Acknowledgments

First and foremost, I would like to thank my family. My mother, Maria Paula Levy Ruscio, and my grandparents, Ellis Levy Ruscio and Myrna Levy Ruscio, for all their support during this PhD, particularly during the pandemic.

I want to extend my utmost gratitude to my supervisor Luis Gregório G. de V. Dias da Silva. I have been working with him since my bachelor's second year. Over the past nine years, I have learned a lot thanks to his guidance, and I was able to research what I found interesting. The liberty I had over the years allowed me to grow into a researcher. I also want to thank him for his continuous support in my everlasting wish to go abroad. I want to thank everyone that was part of the group at some point: Bruna, Dimy, Jesus, Jõao, Lauro, Lucas, and Marcos. It has been a pleasure to work alongside you all. Finally, I want to thank Sandra for helping me with all the bureaucratic matters.

Although I have known him for only one year, I also want to show my most profound appreciation to Thomas Schmidt, my supervisor during my stay in Luxembourg. Thanks to his belief in me, I was able to challenge myself and learn new exciting things while growing as a researcher. The time I spent at Luxembourg University can only be described as amazing. Thomas and his group have always made me feel at home, and for that, I have no words to express my gratitude. I would like to use this space to individually thank everyone from Luxembourg, Andreas, Belen, Byjesh, Christophe, Edvin, Hesky, Justin (Kunmin Wu), Marie, Prathyush, and Sadeq. I like to think that the last hike we did summarizes most of my experiences in Luxembourg. I sincerely hope that you had a good time. Lastly, I want to thank Adamantia for helping me with all bureaucracies and the University of Luxembourg for hosting me.

I want to thank some of my closest friends that supported me over the years and helped me become who I am today. Thanks to the coffee break with Felipe, Gabriel, and Marcia, I could stay focused during the afternoons. Sometimes I felt part of your group for the amount of time I spend with you. It was thanks to you that I had a great time. I also want to thank some of my oldest friends, Daniel, Humberto, Morimoto, Nathalia, and Radharani, for enduring me since high school. I hope to never forget all our shenanigans over the 13 years we have known each other. Lastly, I want to thank Laís, although we stayed together briefly, our friendship felt great.

Last but not least, I want to thank the funding agencies São Paulo Research Founda-

tion (FAPESP) and Brazil's National Council for Scientific and Technological Development (CNPq). Without them, none of this work would have been possible and for that I'm grateful. In particular, thanks to the core mission of FAPESP and the investments in research by the state of São Paulo, I was able to stay one year in Luxembourg. The present work was supported by Brazil's National Council for Scientific and Technological Development, CNPq grant 141556/2018-8 and grants 2019/11550-8 and 2021/07602-2, São Paulo Research Foundation (FAPESP).

"[...] man will only attain existence when he is what he purposes to be. Not, however, what he may wish to be."

Jean-Paul Sartre, Existentialism Is a Humanism

Abstract

Obtaining non-abelian anyons is one of the primary goals within the field of topological states of matter. The simplest of these anyons, Majorana bound states (MBSs) [1], have been proposed as candidates for implementing topological quantum computation relying on its non-abelian statistics [2–5]. Parafermions bound states (PBSs) can be regarded as $\mathbb{Z}_N$ generalizations of the $\mathbb{Z}_2$-symmetric MBSs [6, 7].

PBS have richer non-abelian exchange statistics compared to MBS and would thus offer advantages for quantum computation. In contrast to MBS, PBS usually require strong interactions between electrons and has been proposed to exist, for instance, in fractional quantum Hall insulators with induced superconductivity [8–10]. Tight-binding models have also been suggested to host PBSs [11–13], although in some cases they are non-topological [14]. Recently, Kondo devices have also been proposed to host parafermionic states [15, 16]. Nonetheless, in all setups, many-body interactions are necessary for the existence of PBS.

In this thesis, we are concerned with the properties of PBSs that can be used in experimental setups. While most of the work developed here concerns fermionic models [17, 18], we also investigate a continuous model of fractional quantum Hall insulators with induced superconductivity [19]. This work is, therefore, divided into two parts.

In the first part, we examine the fermionic models using Density Matrix Renormalization Group (DMRG) [20–22] as well as some properties of Fock-parafermion [11]. We start with a proposal on how to use Quantum dots (QDs) to probe the existence of $\mathbb{Z}_4$ parafermions and differentiate it from 2 MBSs ($2\text{x}\mathbb{Z}_2$). Then, we introduce two fermionic models that host $\mathbb{Z}_3$ parafermions. We show the topological equivalence of the models and their properties. In the second part, we use a combination of analytical (semiclassical instanton approximation) and numerical (quantum Monte Carlo simulations) techniques to determine the effective parafermion Hamiltonian and its ground state splitting in a fractional quantum Hall insulators with induced superconductivity.

Keywords: Parafermions, Topological materials, Strong correlated materials, DMRG.

Resumo

A busca por anyons não-abelianos é um dos principais tópicos no campo de matéria condensada topológica. O mais simples destes anyons, estados de Majorana (MBSs) [1], foi proposto como candidato para a implementação de computador quântico topológico que se baseia em estatística não-abeliana [2–5]. Estados de parafermions (PBSs) podem ser entendidos como $\mathbb{Z}_N$ generalizações do $\mathbb{Z}_2$-simétrico MBSs [6, 7].

PBS possuem uma estatística não-abeliana de troca mais rica que o MBS e portanto oferece vantagens para computação quântica. Em contraste ao MBSs, PBSs normalmente necessita de fortes interações entre os elétrons, e foram propostos existir em, por exemplo, isolantes Hall quânticos fracionários com supercondutividade induzida [8–10]. Foi sugerido que alguns modelos tight-biding podem hospedar PBS [11–13], apesar de em alguns casos os PBS não são topológicos [14]. Recentemente, alguns dispositivos Kondo foram propostos como hospedeiros de estados parafermionicos [15, 16]. De toda forma, em todos os sistemas, interações de muitos-corpos são condições necessárias para a existência de PBS.

Nessa tese, estamos interessados nas propriedades dos PBS que podem ser usadas em experimentos. Enquanto a maioria do trabalho refere-se a modelos fermiônicos [17, 18], nos também investigamos modelos contínuos, como isolantes Hall quânticos fracionários com supercondutividade induzida [19], de forma que esse trabalho é dividido em duas partes.

Na primeira parte, nos examinamos modelos fermiônicos usando o método de grupo de renormalização de matriz de densidade (DMRG) [20–22] e propriedades de Fock-parafermions [11]. Começamos com uma proposta de como utilizar pontos quânticos (QD) para examinar a existência de $\mathbb{Z}_4$ parafermions e diferenciá-los de 2 MBS ($2\text{x}\mathbb{Z}_2$). Continuamos com a introdução de dois modelos fermiônicos que possuem $\mathbb{Z}_3$ parafermions e mostramos a equivalência topológica entre os modelos, bem como suas propriedades. Na segunda parte, usamos uma combinação de técnicas analíticas (aproximação semi-clássica de instantons) e numéricas (simulações de Monte Carlo quânticas) para determinar o Hamiltoniano efetivo de parafermions e sua separação de níveis fundamentais em isolantes Hall quânticos fracionários com supercondutividade induzida.

Palavras-chave: Paraférmions, Materiais topológicos, Sistemas fortemente correlacionados, DMRG.

List of Figures

List of Acronyms

DMRG - Density Matrix Renormalization Group
EE - Entanglement entropy
FQH - Fractional quantum Hall
FPF - Fock-parafermion
FPF-SF - Fock-parafermion spectral function
FM - Ferromagnetic
JW - Jordan-Wigner
LDOS - Local density of states
l.h.s. - Left hand side
MBS - Majorana bound state
MZM - Majorana zero mode
PBS - Parafermion bound state
PZM - Parafermion zero mode
QD - Quantum dot
r.h.s. - Right hand side
SC - Superconducting
SF - Spectral function

List of Publications

The thesis is based on the following papers co-authored by myself:

1. Raphael L. R. C. Teixeira, Luis G. G. V. Dias da Silva
   "Quantum dots as parafermion detectors", Phys. Rev. Res. 3, 033014 (2021)

2. Raphael L. R. C. Teixeira, Luis G. G. V. Dias da Silva
   "Edge $\mathbb{Z}_3$ parafermions in fermionic lattices", Phys. Rev. B 105, 195121 (2022)

3. Raphael L. R. C. Teixeira, Andreas Haller, Roshni Singh, Amal Mathew, Edvin G. Idrisov, Luis G. G. V. Dias da Silva, Thomas L. Schmidt
   "Overlap of parafermionic zero modes at a finite distance", Phys. Rev. Res (2022)

Other publication not included in this thesis:

4. Raphael L. R. C. Teixeira, Dushko Kuzmanovski, Annica M. Black-Schaffer, and Luis G. G. V. Dias da Silva
   "Gap oscillations and Majorana bound states in magnetic chains on superconducting honeycomb lattices", Phys. Rev. B 99, 035127 (2019)

5. Raphael L. R. C. Teixeira, Dushko Kuzmanovski, Annica M. Black-Schaffer, and Luis G. G. V. Dias da Silva
   "Enhanced Majorana bound states in magnetic chains on superconducting topological insulator edges", Phys. Rev. B 102, 165312 (2020)

6. Marcos H. L. de Medeiros,Raphael L. R. C. Teixeira, Guilherme M. Sipahi, and Luis G. G. V. Dias da Silva
   "Electric field induced edge-state oscillations in InAs/GaSb quantum wells", Phys. Rev. B 104, 195307 (2021)

Contents

Chapter 1

Introduction

Currently, one of the major enterprises in condensed matter physics is the quest for anyons [24–26], in particular, those with non-Abelian statistics, i.e. exchange is not commutative, and two exchanges do not go back to the same state. The reason for this wide search is both theoretical and practical. While it is possible to learn about quantum materials and new states of matter, it was also suggested that they could be applied in topological quantum computers [2, 5, 27].

Due to its simplicity, and recent investments by Microsoft, Majorana bound state (MBS) are one of the most studied non-Abelian states in condensed matter. Non-Abelian anyons can be classified into different types using topological quantum field theory [2]. Of those types, the Ising type is one of the simplest. MBS has exchange statistics of the Ising type [1, 4, 28]. The problem is that it has been known that qubits with non-Abelian anyons of Ising type can't go to any point in a Bloch-sphere with only gates made by braiding. In other words, a topological quantum computer made of it wouldn't be universal in the sense that some computations wouldn't have the "topological protection" [3, 4]. To have a universal quantum computer is necessary to have Fibonacci anyons [7, 29]. Those are much harder to get [29–31]. However, it is possible to have a "middle-ground" that has more protected operations, but not all, since they are still of Ising type. Those are the $\mathbb{Z}_n$ parafermions and the main topic of this thesis.

Parafermions were first introduced in the context of clock-models [32] and later it was recognized as a good description to some fractional quantum Hall excitations [33]. Only after the seminal paper of Paul Fendley [6], showing the parafermions, like its $\mathbb{Z}_2$ Majorana counterpart, could form a zero-energy state in a chain, that the field gained a lot of attention. Since then, parafermion modes have been studied in the context of fractional quantum Hall edges [10, 34–37], 1D systems [12–14, 38–45] and others [44, 46–52]

In this thesis, we look into some of the most intriguing questions about parafermions and what makes them unique. In chapter 2 we explore the possibility of detecting fermionic $\mathbb{Z}_4$ parafermions using quantum dots. In chapter 3, we propose two models to realize fermionic $\mathbb{Z}_3$ parafermions, and we investigate their properties. Finally, in chapter 4, we

look into finite-size effects of parafermions in fractional quantum hall edges and how it differs from its Majorana counterpart.

1.1 Preliminaries

Before we start looking into parafermions, it is wise to begin with the well-known Majorana. First proposed by Ettore Majorana in 1937 as a real solution to Dirac's equation [53], "Majorana fermions" have the intriguing property of being its own anti-particle. The search for such particle spanned from neutrinos[1] in high-energy physics to quasi-particles in condensed matter physics. Majoranas[2] have appeared in different contexts of condensed matter such as edges of quantum Hall systems [55, 56], two-channel Kondo devices [57, 58].

Nonetheless, only in 2001 with the proposal by Alexei Kitaev of a simple tight-biding model of spinless electrons with p-wave superconductivity [1] that researchers started realizing the potential of Majorana bound states. Kitaev's toy model was followed by a somewhat more realistic nanowire model [59–62] that had the advantage of being realizable in experiments. Since 2012, with the first paper claiming to observe Majorana zero modes [63], many papers made similar claims [64–68]. Although some of them have had "expressions of concern" or have been retracted [69–71]. Recently, a Microsoft team wrote that they found Majorana bound states and they used complex models to predict and prove that this is indeed a topological phase [72], although some people have expressed scepticism about the result. For now, much of the work has been modelling and theory behind Majoranas while the experimental has been filled with a myriad of issues, which shows how difficult is to obtain clear proof of MBS.

In this section, we will give an overview of Majorana bound states. We will go from the Ising model to Kitaev's chain up to nanowires while discussing some aspects that are also important in parafermion bound states [6].

We begin with the quantum Ising chain, a two-state quantum system with 1/2 "spin" particle at each L site. The Hamiltonians consists of two interactions, the first term flips the spin at a given site, the second term describes the interaction between neighbours spins,

$$H_{\text{ising}} = -h\sum_{j=1}^{L}\sigma_j^x - J\sum_{j=1}^{L-1}\sigma_j^z\sigma_{j+1}^z, \tag{1.1}$$

where $\sigma_j^{x,y,z}$ acts with a Pauli matrix on the two-state system at site j and commutes with all other sites. At $h = J$, there is a critical point in the quantum Ising model. The above

[1] It is an open question if neutrinos are an example of Majorana fermion [54].

[2] Here, we take some liberty to generically call Majoranas different entities such as Majorana bound states, Majorana zero modes (sometimes used intertwined with the previous) and Majorana fermion. The latter is not commonly used since in condensed matter we only have electrons, although it is sometimes used to describe an operator.

Hamiltonian is invariant under a spin-flip of all spins. For this reason, we can define the operator

$$(-1)^F = \prod_{j=1}^{L} \sigma_j^x, \tag{1.2}$$

that squares to 1 and satisfy $[(-1)^F, H_{\text{ising}}] = 0$, therefore the Hamiltonian has a $\mathbb{Z}_2$ symmetry. We can perform a Jordan-Wigner transformation to a basis in which the operators anticommute [73]

$$\gamma_{A,j} = \left(\prod_{k=1}^{j-1} \sigma_k^x\right) \sigma_j^z, \qquad \gamma_{B,j} = i \left(\prod_{k=1}^{j} \sigma_k^x\right) \sigma_j^z = i\gamma_{A,j}\sigma_j^x, \tag{1.3}$$

the γs are Majorana fermion operators, that satisfy $\gamma_{A(B),j}^\dagger = \gamma_{A(B),j}$ and $\{\gamma_{\alpha,j}, \gamma_{\beta,k}\} = 2\delta_{\alpha,\beta}\delta_{j,k}$. In this new basis, the Ising Hamiltonian (at the critical point) becomes

$$H_{\text{ising}} = -iJ \sum_{j=1}^{L} \left(\gamma_{B,j}\gamma_{A,j+1} + \gamma_{A,j}\gamma_{B_j}\right). \tag{1.4}$$

It is interesting to notice that in the Majorana basis, the Hamiltonian is bilinear and, therefore, the spectrum can be easily calculated. In this new basis, the symmetry generator assumes the product of all Majorana operators, $(-1)^F = \prod_j i\gamma_{A,j}\gamma_{B,j}$.

The problem of the Majorana basis is the absence of occupation number for Majorana fermions since $\gamma_{A(B),j}^\dagger \gamma_{A(B),j} = 1$. Thus, it is wise to write the Hamiltonian on a basis with an associated Fock-space. This is done by rewriting the Majorana operators in terms of spinless fermions, $c_j^\dagger = (\gamma_{A,j} + i\gamma_{B,j})/\sqrt{2}$. We can rewrite the Ising model to obtain

$$H_{\text{ising}} = -J \sum_j \left(c_j^\dagger c_{j+1} + c_j^\dagger c_{j+1}^\dagger - 2c_j^\dagger c_j\right) + \text{H.c.} \tag{1.5}$$

Where we dropped the constant term. The symmetry generator is now given by the total parity of the system $(-1)^F = \prod_j (1 - 2c_j^\dagger c_j)$. The model Kitaev proposed [1], identified each term with its physical meaning and allowed them to change independently,

$$H_{\text{kitaev}} = \sum_j -tc_j^\dagger c_{j+1} + \Delta c_j^\dagger c_{j+1}^\dagger - \mu c_j^\dagger c_j + \text{H.c.}, \tag{1.6}$$

with t the hopping, Δ the p-wave superconducting order parameter and μ the chemical potential. This model has two distinct topological phases. For $t = \Delta$ we have a trivial phase ($2t > |\mu|$) and a non-trivial phase[3]($2t < |\mu|$). This can be easily observed when we

[3]A non-trivial topological phase cannot be adiabatically deformed into an insulator without closing the gap.

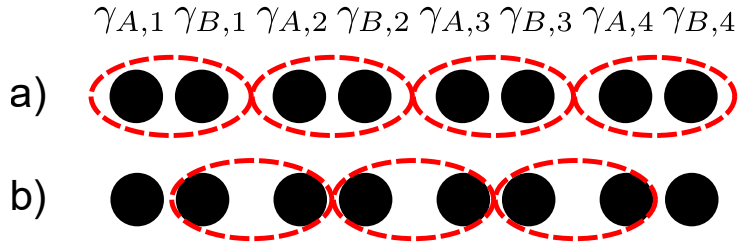

Figure 1.1: Illustration of two limits of the Kitaev model. Each site is split into two Majorana fermions, $\gamma_{A,j}, \gamma_{B,j}$. (a) Trivial phase, $t = \Delta = 0$ and $\mu \neq 0$, in which the Majorana Fermions interact only at the same site. (b) non-trivial phase, $t = \Delta \neq 0$ with $\mu = 0$, in which one Majorana fermion interacts with the neighbour site. Because of this, two dangling Majorana fermions don't contribute to the energy.

go back to the Majorana basis,

$$H_{\text{kitaev}} = \frac{i}{2}\sum_j -\mu\gamma_{A,j}\gamma_{B,j} + (t + |\Delta|)\gamma_{B,j}\gamma_{A,j+1} + (-t + |\Delta|)\gamma_{A,j}\gamma_{B,j+1}, \tag{1.7}$$

and take two limits, $t = \Delta = 0$ with $\mu \neq 0$ and $t = \Delta \neq 0$ with $\mu = 0$. These two limits are illustrated in Fig. 1.1. While in the former case, we have all Majorana fermions locally coupled in the same site, Fig. 1.1(a), in the latter case, we have Majoranas interacting with the neighbour site at the same time that the Majoranas at the ends don't couple, Fig. 1.1(b), such that we have two states with zero energy associated with the chain's ends. Theoretically, we could construct a non-local fermion $c_{\text{nl}}^\dagger = (\gamma_{A,1} + i\gamma_{B,L})/\sqrt{2}$ and store information in the parity, since creating or destroying this electron doesn't change the energy and local-perturbations don't affect it. Indeed this is one of the aspects important for topological quantum computation [74–76]. The other one is non-Abelian exchange statistics [5, 77].

So far, we briefly looked at one of the simplest models that have Majorana zero modes at the edges. Although useful for studying some properties, the Kitaev model is unrealistic in experimental setups other than optical lattice. Not only is p-wave superconductivity uncommon, but to have spinless fermions would be necessary to have high magnetic fields that would destroy the superconductivity. This was realized early on, and a few years later, a new model that considers a nanowire with spin-orbit coupling close to an s-wave superconductor was proposed,

$$H_{\text{nano}} = (-\partial_x^2 - \mu(x))\tau_z + V_z\sigma_z + i\alpha\partial_x\sigma_y\tau_z + \Delta\tau_x, \tag{1.8}$$

where τ is the vector of Pauli matrix associated with electron-hole subspace and σ is the vector of Pauli matrix associated with spin. The first term is the Kinetic part with a chemical potential μ, V_z is a Zeeman field that corresponds to the magnetic field, α is the spin-orbit coupling, and Δ is the induced superconducting gap.

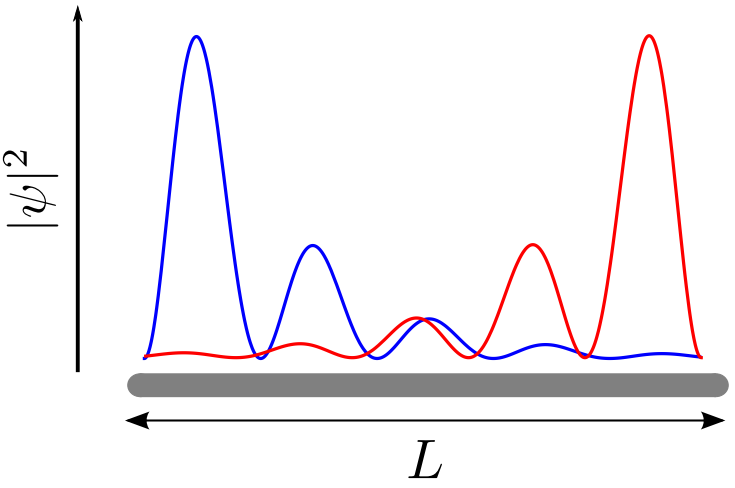

Figure 1.2: Illustration of the left and right Majorana wavefunction spread over a nanowire (in grey). The wavefunctions' overlap is responsible for splitting in the ground state energy.

The advantage of this model is that it could be realized, and around one year after it was proposed, some experiments claimed to see Majorana bound states[4]. On the other hand, the Majorana in the nanowires are not perfectly localized at the ends. This leads to an overlap of Majorana bound states, Fig. 1.2, that open a gap that can be tuned with chemical potential and magnetic field [82],

$$\Delta E \approx k_f \frac{e^{-2L/\xi}}{m\xi} \cos(k_f L), \tag{1.9}$$

where k_f is a function of the chemical potential μ and Zeeman field V_z and ξ is a coherence length. These are sometimes called "Majorana oscillations" and were thought to be an explanation for some experiments without clear zero energy states[5] [65].

1.2 Parafermions

Based on the preliminaries section, we can now introduce parafermions in the same way we did for Majorana fermions. Here, however, we don't use the Ising model. Instead, we use clock-models, that can be thought of as a $\mathbb{Z}_n$ generalization of Ising with n different spins[6], $1, \omega, \omega^2, ...\omega^{n-1}$, with $\omega = e^{i2\pi/n}$.

Similar to Pauli matrices, we can define new matrices called "clock-variables" [6, 32], that satisfies the following properties

$$\sigma^\dagger = \sigma^{n-1}, \qquad \tau^\dagger = \tau^{n-1}, \qquad \sigma^n = \tau^n = 1, \qquad \sigma\tau = \omega\tau\sigma. \tag{1.10}$$

[4]Today is accepted that what was observed was probably not Majorana bound states, but Andreev bound states mostly due to disorder [78–81].

[5]Although nowadays it is thought to be Andreev bound states.

[6]For $n = 2$ we have the Ising model with the usual ± 1 spin.

In a basis that σ is diagonal, the clock-variable's matrices are

$$\sigma = \begin{pmatrix} 1 & 0 & 0 & \dots & 0 \\ 0 & \omega & 0 & \dots & 0 \\ 0 & 0 & \omega^2 & & 0 \\ \vdots & \vdots & & \ddots & \vdots \\ 0 & 0 & 0 & \dots & \omega^{n-1} \end{pmatrix} \qquad \tau = \begin{pmatrix} 0 & 0 & 0 & \dots & 0 & 1 \\ 1 & 0 & 0 & \dots & 0 & 0 \\ 0 & 1 & 0 & & 0 & 0 \\ \vdots & \vdots & \ddots & & \vdots & \vdots \\ 0 & 0 & 0 & \dots & 1 & 0 \end{pmatrix} \tag{1.11}$$

We now write the most general Hamiltonian that preserves $\mathbb{Z}_n$-symmetry when we "increase" the "spins", $\sigma \to \omega\sigma$. At each site, the clock-variables satisfy Eq. (1.10) and the operators at different sites commute.

$$H_{Zn} = \sum_j \sum_{m=1}^{n-1} \left[-f\alpha_m \tau_j^m - J\hat{\alpha}_m \left(\sigma_j^\dagger \sigma_{j+1} \right)^m \right] \tag{1.12}$$

where the phases must satisfy $\alpha_m^* = \alpha_{n-m}$ and $\hat{\alpha}_m^* = \hat{\alpha}_{m-n}$ for H_{Zn} to be Hermitian. While the first term generalizes the onsite spin-flip from Ising, the second term generalizes the neighbour's interaction. Varying the phases allows us to interpolate between ferromagnetic and antiferromagnetic phases without changing f, J. However, differently from Ising, the ferromagnetic and antiferromagnetic phases are not necessarily equivalent. For instance, depending on n there might be more spins interacting in one phase than another [6].

The phases $\alpha, \hat{\alpha}$ also control the integrability of the system. Consider the case $n = 3$, when $\arg(\alpha) = \arg(\hat{\alpha}) = 0$ we have the quantum version of three state Potts models that have a critical, integrable, and self-dual point at $f = J$ that separates ordered from disordered phases[6]. For nonzero $\alpha, \hat{\alpha}$ we have more intricate phases [83].

The symmetry generator for the clock-model is

$$\omega^P = \prod_j^L \tau_j^\dagger, \tag{1.13}$$

which satisfy $(\omega^P)^n = 1$, and is a clear generalization of Eq. (1.2). Following the steps from Majorana fermion, we can define new operators called *parafermion* using the Fradkin-Kadanoff transformation [32] that multiply ordered and disordered clock-variables. At each site, we need to define two parafermion operators, χ_j and ψ_j, that generalize Majorana Fermions, $\gamma_{A,j}$ and $\gamma_{B,j}$,

$$\chi_j = \left(\prod_{k=1}^{j-1} \tau_k \right) \sigma_j, \qquad \psi_j = \omega^{(n+1)/2} \left(\prod_{k=1}^{j} \tau_k \right) \sigma_j = \omega^{(n-1)/2} \chi_j \tau_j. \tag{1.14}$$

Following the properties of σ and τ, Eq. (1.10), parafermion do not square to one, instead it power n equals one, and different parafermion operators do not (anti-)commute.

By contrast, swapping the operators leads to a phase ω,

$$\begin{aligned} &\chi_j^\dagger = \chi_j^{n-1}, \qquad \psi_j^\dagger = \psi_j^{n-1}, \qquad \chi_j^n = \psi_j^n = 1, \qquad \chi_j\psi_j = \omega\psi_j\chi_j \\ &\chi_j\chi_k = \omega\chi_k\chi_j, \qquad \psi_j\psi_k = \omega\psi_k\psi_j, \qquad \chi_j\psi_k = \omega\psi_k\chi_j \qquad j < k. \end{aligned} \tag{1.15}$$

Interesting, parafermion operators of different sites do not commute like clock-variables, this happens because of the strings at the r.h.s. of Eqs. (1.14) and the restriction $j < k$ comes from the commutation due strings[7].

Inverting the definition of parafermion operators,

$$\tau_j = \omega^{-(n-1)/2}\chi_j^\dagger\psi_j, \qquad \sigma_j^\dagger\sigma_{j+1} = \omega^{-(n-1)/2}\psi_j^\dagger\chi_{j+1}, \tag{1.16}$$

we can easily obtain the terms of the Hamiltonian H_{Zn} by applying it to Eq. (1.12). The generalized parafermion Hamiltonian is given by

$$H_{Zn} = \sum_j \sum_{m=1}^{n-1} \omega^{m(m-n)/2} \left(-f\alpha_m \chi_j^{\dagger m}\psi_j - J\hat{\alpha}_m \psi_j^{\dagger m}\chi_{j+1} \right). \tag{1.17}$$

It is usual to consider a simplified parafermion Hamiltonian,

$$H_{pf} = \sum_j -f\chi_j^\dagger\psi_j - J\psi_j^\dagger\chi_{j+1} + \text{H.c.} \tag{1.18}$$

that is the generalization of Eq. (1.4) when we substitute $\gamma_A \to \chi,\ \gamma_B \to \psi$. The next step is to consider a Fock-space for parafermions, dubbed "Fock-parafermion space" [11]. Although this Fock-space *is not* like the usual fermions[8] it allows us to write an expression for the ground state's wavefunction and understand many aspects of H_{pf}. Recently, some papers started looking into models that only consider Fock-parafermion demonstrating its versatility as a research theme [84–87].

In the fermionic case, we have the vacuum and a single occupied state ($|0\rangle, |1\rangle$), here, however, we have n states ($|0\rangle, |1\rangle, ..., |n-1\rangle$). We can define a Fock-parafermion creation ($d^\dagger$) and annihilation (d) operators [11] that respectively rises and lowers the state, with the condition $d^\dagger |n-1\rangle = 0$ and $d|0\rangle = 0$[9], such that for multiple "orbitals" we have

$$\begin{aligned} d_j^\dagger |n_1, n_2, ..., n_j, ..., n_L\rangle &\equiv \bar{\omega}^{\sum_{k<j} n_k} |n_1, n_2, .., n_j + 1, ..., n_L\rangle \\ d_j |n_1, n_2, ..., n_j, ..., n_L\rangle &\equiv \omega^{\sum_{k<j} n_k} |n_1, n_2, .., n_j - 1, ..., n_L\rangle, \end{aligned} \tag{1.19}$$

[7]The case $j > k$ can also be easily calculated and instead ω we have the complex conjugate $\bar{\omega}$.

[8]The Fock-parafermion satisfy the $\mathcal{F}_n(L)$ algebra, i.e. the n-Grassmann algebra with L generators (number of different orbitals, sites,...). For $n = 2$, $\mathcal{F}_2(L)$ is the standard Fock-space of indistinguishable electrons.

[9]This is a p-exclusion that generalizes the Pauli Exclusion Principle of electrons.

where the string comes from the normal ordering due to commutation between operators of different sites, similar to the $(-1)^{\sum n}$ phase in electrons. All these properties can be summarized by [11],

$$\begin{aligned} d_j^{\dagger n} = 0, \qquad d_j^\dagger d_k^\dagger = \omega d_k^\dagger d_j^\dagger \qquad j < k \\ d_j^{\dagger m} d_j^m + d_j^{n-m} d_j^{\dagger n-m} = 1 \qquad m = 1, .., n-1. \end{aligned} \tag{1.20}$$

The last line generalizes the anti-commutation of fermions, $\{c_j^\dagger, c_j\} = 1$. With some manipulation, we can obtain the relation.

$$d_j d_j^{\dagger m} d_j^m = d_j^{\dagger m-1} d_j^m \tag{1.21}$$

Other than creation and annihilation operators, we also need to consider the number operator, N, such that $N\left|k\right\rangle = k\left|k\right\rangle$. More generally, for L orbitals,

$$N_j \left|n_1, n_2, ..., n_j, ..., n_L\right\rangle = n_j \left|n_1, n_2, ..., n_j, ..., n_L\right\rangle, \tag{1.22}$$

in terms of Fock-parafermion operators, the number operator is

$$N_j = \sum_{m=1}^{n-1} d_j^{\dagger m} d_j^m, \tag{1.23}$$

and it follows from previous properties that N_j satisfies the commutation relation

$$[N_j, d_j^\dagger] = d_j^\dagger, \qquad [N_j, d_j] = -d_j. \tag{1.24}$$

Note that all properties reduce to the usual fermionic relation for $n = 2$. Finally, the parafermion operators are easily written in the Fock-parafermion space,

$$\chi_j = d_j + d_j^{\dagger n-1}, \qquad \psi_j = -\omega^{-1/2}\left(d_j \omega^{N_j} + d_j^{\dagger n-1}\right), \tag{1.25}$$

where the phase, ω^{N_j} can be expanded in terms of Fock-parafermion operators

$$\omega^{N_j} = 1 + (\omega - 1)\sum_{m=1}^{n-1} \omega^{m-1} d_j^{\dagger m} d_j^m. \tag{1.26}$$

To conclude this section, we go back to H_{pf}, Eq. (1.18), with $f = 0$. The ground state of a L-site chain, for this particular, case can be write as a sum of all states such that the

total number of Fock-parafermion is i [88],

$$|g_i^L\rangle = \frac{1}{\sqrt{n^{L-1}}} \sum_{\substack{\{N_j\} \text{ such that} \\ \sum_j N_j = i \ mod \ n}} \bigotimes_{j=1}^{L} |N_j\rangle, \tag{1.27}$$

where the sum is understood to be over all possible combination of N_j that satisfy $\sum_j N_j = i \ mod \ n$. As a consequence, each site of *any* ground state is given by a sum of all Fock-parafermion numbers.

1.3 Parafermions in condensed matter

So far, we have explored different theoretical aspects of parafermions. Therefore, it is essential to look into physical systems that host parafermions modes that can be experimentally realized. The first thing to notice is that parafermions are $\mathbb{Z}_n$-symmetric which is not covered in the tenfold classification of topological systems [14, 89]. This implies that the physical system will probably be strongly interacting instead or will have long-range interaction.

Indeed, in tight-biding models, we observe both characteristics [12, 18]. Such systems could, in principle, be realized in optical lattices [90] and maybe in synthetic dimensions [91]. A more realistic approach is to consider charge-Kondo devices [15, 92, 93] or fractional quantum Hall systems with regions of different spectral gaps. Recent experiments [23, 94–97] were able to create a "superconducting finger" on an FQH system, Fig. 1.3(a), and it was reported a crossed Andreev reflection compatible with fractional charge [23].

In this section, we show how $\mathbb{Z}_{2m}$ parafermion modes appear in fractional quantum Hall edges. Generically, we need two counter-propagating modes[10], with filling factor $1/m$[11], and regions with different spectral gaps. Although the idea used here can be generalized to other systems [50], we consider one of the first proposals to have localized parafermion modes at the interfaces [8, 9, 101, 102], Fig. 1.3(b). Note that since the parafermions are located in the interfaces, we can't circle one parafermion around the other to do braiding. Instead, it is necessary to use a different approach, such as fusion and nucleation [8, 36, 103].

We start with two counter-propagating electrons with opposite spins[12] [9]. We can write the electron operators in terms of a chiral bosonic field, $\varphi_{R/L}$, $\psi_{R/L} \sim e^{im\varphi_{R/L}}$ that satisfies the commutation relation $[\varphi_{R(L)}(x), \varphi_{R(L)}(x')] = \pm(i\pi/m)\ \mathrm{sgn}(x - x')$ and

[10] A single state is not enough as the edge cannot be gapped.

[11] The filling factor $1/m$, m odd, corresponds to Laughlin states that has excitations with charge e/m, thus providing a building block to parafermions [98–100].

[12] This can be done by having each FQH with g-factor of opposite sign.

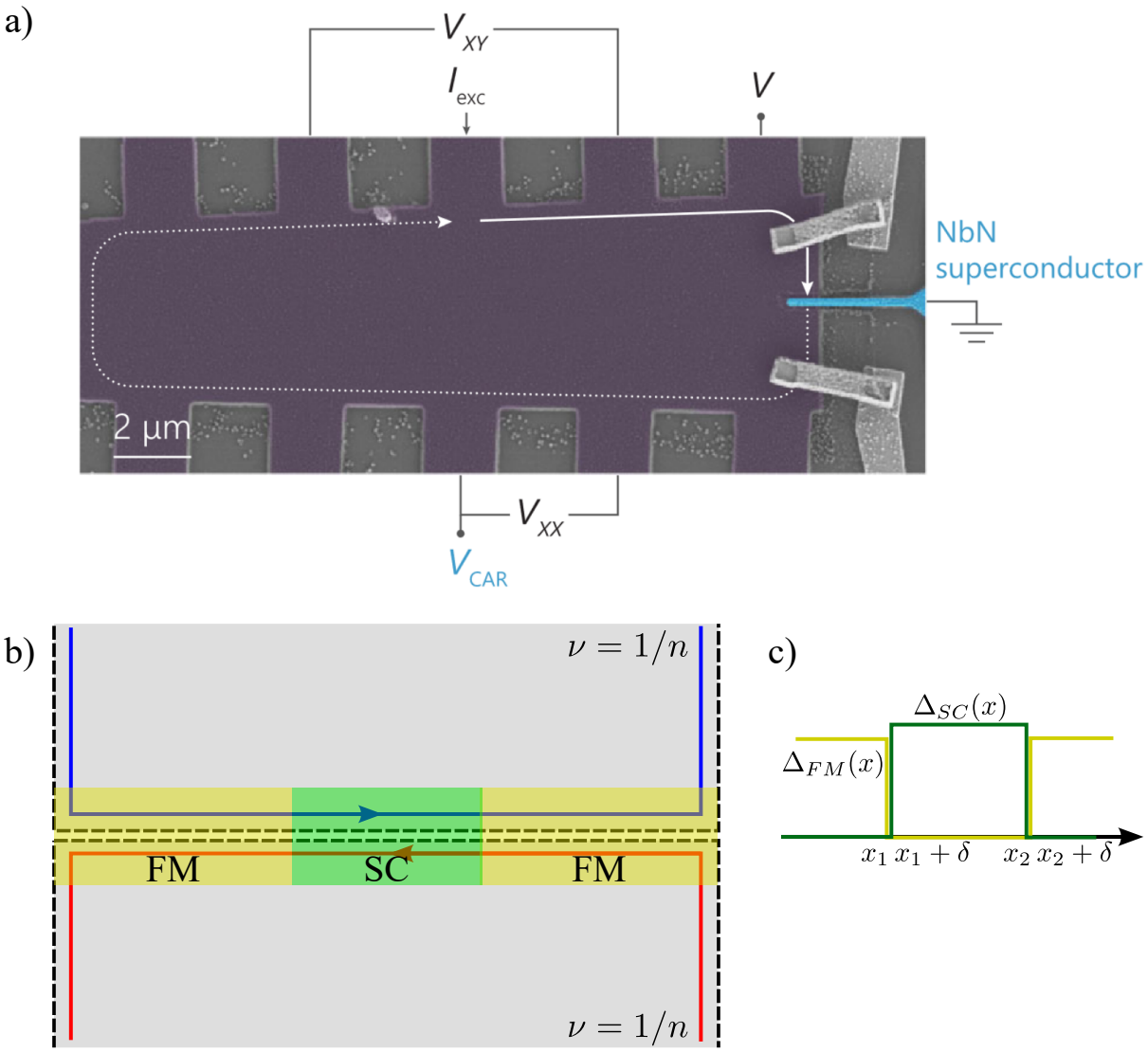

Figure 1.3: (a) Adapted from Ref. [23]. A Graphene device encapsulated with boron nitride dielectric and graphite with an NbN superconductor of less than 100nm. The gate voltage, V, can be used to tune the system into fractional quantum Hall state with filling factor 1/3 [23]. (b) Typical experimental proposal to realize $\mathbb{Z}_{2m}$ parafermion bound states [9]. Two counter-propagating edges of FQH with filling factor $1/m$ and regions with different spectral gaps. (c) Profile of the different couplings along the edge in (a). The FM region has a backscattering amplitude Δ_{FM} and the SC region has an electron pairing Δ_{SC}.

$[\varphi_L(x), \varphi_R(x')] = i\pi/m$ [104–106], see Appendix A.

Then we consider three regions, such that we have a FM-SC-FM junction. In the two regions dubbed FM, $x < x_1$ and $x > x_2 + \delta$, there is backscattering due to the close proximity of an insulator with spin-orbit coupling such that we have an interaction $\Delta_{FM}\psi_L^\dagger\psi_R + \text{H.c.}$. In the region dubbed SC, $x_1 + \delta < x < x_2$, the electrons interact to form a cooper pair, and we have a term $\Delta_{SC}\psi_L^\dagger\psi_R^\dagger + \text{H.c.}$. Finally, at the interface $x_1 < x < x_1 + \delta$ and $x_2 < x < x_2 + \delta$ where both couplings go to zero[13].

Now, it is useful to rewrite the chiral fields in terms of two new fields, $\varphi_{R/L} = \phi \pm \theta$, where the electron density is $\rho = \partial_x\theta/\pi$ and the new fields satisfy

$$[\phi(x), \theta(x')] = \frac{i\pi}{n}\Theta(x - x') \tag{1.28}$$

The edge Hamiltonian can be modeled as $H = H_0 + H_I$, where

$$H_0 = \frac{mv}{2\pi}\int dx \left[(\partial_x\phi)^2 + (\partial_x\theta)^2\right], \tag{1.29}$$

corresponds to gapless counter-propagating edge mode with speed v. The Hamiltonian that describes the backscattering and copper pairs is

$$\begin{aligned} H_1 &= -\int dx \Delta_{SC}(x)\psi_L^\dagger\psi_R^\dagger + \Delta_{FM}(x)\psi_L^\dagger\psi_R + \text{H.c.} \\ &\sim -\int dx \left[\Delta_{FM}(x)\cos(2n\theta) + \Delta_{SC}(x)\cos(2n\phi)\right], \end{aligned} \tag{1.30}$$

where $\Delta_{SC(FM)}(x) = \Delta_{SC(FM)}$ in the SC(FM) region and 0 otherwise. In the limit that the couplings Δ_{SC} and Δ_{FM} are sufficiently large, the fields ϕ and θ will be pinned to one of the 2m minima of the cosine above in the SC and FM regions respectively. In this case, we can write the fields as $\theta_{x<x_1} = \pi\hat{n}_\theta^{(1)}/m$, $\phi_{x_1+\delta<x<x_2} = \pi\hat{n}_\phi/m$ and $\theta_{x>x_2} = \pi\hat{n}_\theta^{(2)}/m$ and n_ϕ, $n^(1/2)_\theta$, are integer-valued operators. From Eq. (1.28), we have

$$\left[\hat{n}_\phi, \hat{n}_\theta^{(1)}\right] = \frac{in}{\pi}, \qquad \left[\hat{n}_\phi, \hat{n}_\theta^{(2)}\right] = 0. \tag{1.31}$$

Now, we will look at the first interface, and the same procedure can be done to the second one provided that we consider that the interface will be SC-FM instead of FM-SC and that the commutation relations are not the same, Eq. (1.31). At the interface $\Delta_{SC(FM)} = 0$ and the effective Hamiltonian is

$$H_{\text{eff},1} = \frac{mv}{2\pi}\int_{x_1}^{x_1+\delta} dx \left[(\partial_x\phi)^2 + (\partial_x\theta)^2\right]. \tag{1.32}$$

This Hamiltonian can be diagonalized by expanding the ϕ, θ fields into bosonic ladder

[13]This is not necessary but makes the calculation easy.

operators, a_k that satisfy $[a_k, a_{k'}^\dagger] = \delta_{k,k'}$,

$$\phi(x) = \frac{\pi \hat{n}_\varphi}{n} + \sqrt{\frac{2}{n}} \sum_{k=0}^{\infty} \frac{\cos(\lambda_k(x))}{2k+1}(a_k + a_k^\dagger), \tag{1.33}$$
$$\theta(x) = \frac{\pi \hat{n}_\theta^{(1)}}{n} + \sqrt{\frac{2}{n}} \sum_{k=0}^{\infty} \frac{\sin(\lambda_k(x))}{2k+1} i(a_k - a_k^\dagger),$$

where $\lambda_k = (2k+1)\pi(x - x_1)/2\delta$. Note that this expansion preserves the boundary condition as well as the commutation relation of both fields. The Hamiltonian, in terms of this new operator, is

$$H_{\text{eff},1} = \sum_{k=0}^{\infty} \epsilon_k (a_k^\dagger a_k + 1/2), \qquad \text{where } \epsilon_k = \frac{\pi v}{\delta}(k + 1/2). \tag{1.34}$$

Although we see a finite gap, inversely proportional to δ, for bosons a_k, the domain wall admits zero modes. To show that, we go back to the chiral field

$$\varphi_{R/L}(x) = \frac{\pi}{n}(\hat{n}_\phi \pm \hat{n}_\theta^{(1)}) + \sqrt{\frac{2}{n}} \sum_{k=0}^{\infty} \frac{\left(e^{\pm i\lambda_k(x)} a_k + \text{H.c.}\right)}{\sqrt{2k+1}} \tag{1.35}$$

which satisfy the relations

$$\varphi_L(x_1) = \varphi_R(x_1) - \frac{2\hat{n}_\theta^{(1)}}{n}, \tag{1.36}$$
$$\varphi_L(x_1 + \delta) = -\varphi_R(x_1 + \delta) + \frac{2\hat{n}_\phi}{n}.$$

Using both Eqs. (1.34) and (1.35) it is possible to show that

$$\left[H, e^{i\varphi_{R/L}(x)}\right] = \pm iv\partial_x e^{i\varphi_{R/L}(x)}. \tag{1.37}$$

Integrating over x, we obtain

$$\left[H, \int_{x_1}^{x_1+\delta} e^{i\varphi_{R/L}(x)}\right] = \pm iv\left(e^{i\varphi_{R/L}(x_1+\delta)} - e^{i\varphi_{R/L}(x_1)}\right). \tag{1.38}$$

We can use Eqs. (1.36) and (1.38) to show that the operator

$$\alpha_L = e^{\frac{i\pi}{n}(\hat{n}_\phi + \hat{n}_\theta^{(1)})} \int_{x_1}^{x_1+\delta} dx \left[e^{-\frac{i\pi}{n}(\hat{n}_\phi + \hat{n}_\theta^{(1)})} e^{i\varphi_R(x)} + e^{-\frac{i\pi}{n}(\hat{n}_\phi - \hat{n}_\theta^{(1)})} e^{i\varphi_L(x)} + \text{H.c.}\right] \tag{1.39}$$

commutes with the Hamiltonian and, therefore, is a zero mode bound to the domain wall constructed from quasiparticle operators $e^{i\varphi_{R/L}}$ that has fractional charge e/m. We can

project the operator in the ground state by taking $a_k^\dagger a_k = 0$ to obtain

$$\alpha_L \sim e^{\frac{i\pi}{m}(\hat{n}_\phi + \hat{n}_\theta^{(1)})}. \tag{1.40}$$

So far, we have only considered the first domain wall. However, as stated before, the same can be done to the second domain wall [9]. In this case, taking the appropriate limits, we obtain

$$\alpha_R \sim e^{\frac{i\pi}{m}(\hat{n}_\phi + \hat{n}_\theta^{(2)})}. \tag{1.41}$$

It is easy to see that these operators satisfy the relations

$$\alpha_L^{2m} = \alpha_R^{2m} = 1, \qquad \alpha_L \alpha_R = e^{i\pi/m} \alpha_R \alpha_L, \tag{1.42}$$

which are the same as Eq. (1.15) demonstrating that the operators α_L and α_R corresponds to $\mathbb{Z}_{2m}$ parafermion zero modes.

Chapter 2

Quantum dots as Parafermion detectors

Over this thesis, we are generally concerned with the properties of parafermion bound states. Here, however, we propose a protocol to measure parafermions. This chapter, therefore, is concerned with the crucial question: given a system that hosts parafermion zero modes (PZMs), how can we detect them?

Previously, quantum dots (QDs) have been used to distinguish the presence of Majorana bound states [107–111]. We adapt this idea to include parafermion zero modes, in particular, we focus on $\mathbb{Z}_4$ fermionic parafermions [12, 13]. These $\mathbb{Z}_4$ fermionic parafermions are "poor's man parafermions", in the sense that they do not satisfy the "pure" $\mathbb{Z}_4$ parafermion braiding.

Our results show that experimentally readily accessible QD properties, such as the local density of states and occupation number, can be used to distinguish the different topological phases of the system, indicating the presence or absence of edge PZMs. More importantly, the QD signatures can distinguish between phases of local $\mathbb{Z}_4$ parafermionic modes and those comprised of two $\mathbb{Z}_2$ Majorana modes. Moreover, after our results were published, it was suggested that quantum dots could, indeed, be used to detect "pure" parafermions [112]. This chapter is adapted from *"Quantum dots as parafermion detectors"*, Phys. Rev. Res. 3, 033014 (2021).

2.1 Model

We consider a setup composed of a quantum dot coupled to a 1D fermionic chain that hosts $\mathbb{Z}_4$ parafermionic modes at its ends, as depicted in Fig. 2.1. The first challenge is to devise a system of correlated 1D spinful fermions which can host such $\mathbb{Z}_4$ parafermionic modes[1]. A promising path is to express parafermionic operators in terms of

[1]The question if those are truly parafermions are a bit semantic. Some people regard them as parafermion since they come from a parafermion model, albeit a fermionized model. Others regard them

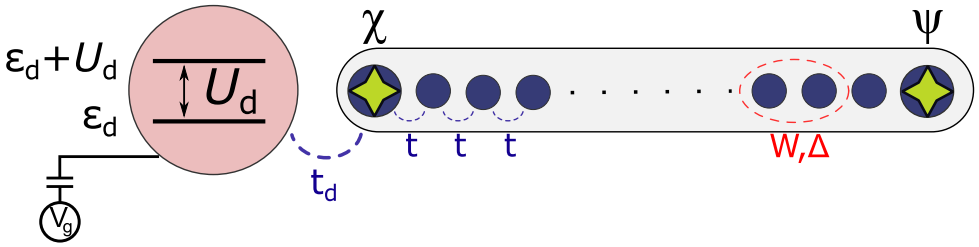

Figure 2.1: Parafermion chain coupled to a quantum dot. The dot has an electron-electron repulsion given by U_d and an energy given by ϵ_d controlled by the gate voltage V_g. The chain is coupled to the dot by a hopping with andreev reflection given with strength t_d. The chain has two dangling parafermions at the edges χ and ψ when $t = W = \Delta$.

purely fermionic ones [6, 47] and then write a Kitaev-like model for $\mathbb{Z}_4$ parafermions as a strongly-correlated fermionic model in 1D with local terms only [12]. Such transformation will generate (nearest neighbor) superconducting and two- and three-body interaction terms. After collecting these terms, we can write the following Hamiltonian for the model as

$$H_{Z_4} = H_{\mathrm{SC}} + H_W \ , \tag{2.1}$$

with

$$H_{\mathrm{SC}} = -\sum_{\sigma,j} t c^\dagger_{\sigma,j} c_{\sigma,j+1} - i\Delta c^\dagger_{-\sigma,j} c^\dagger_{\sigma,j+1} \tag{2.2}$$

$$\begin{aligned} H_W = -W \sum_{\sigma,j} \Big[& c^\dagger_{\sigma,j} c_{\sigma,j+1} \left(-n_{-\sigma,j} - n_{-\sigma,j+1}\right) + c^\dagger_{\sigma,j} c^\dagger_{\sigma,j+1} \left(n_{-\sigma,j} - n_{-\sigma,j+1}\right) \\ & + i c^\dagger_{\sigma,j} c_{-\sigma,j+1} \left(n_{-\sigma,j} - n_{\sigma,j+1}\right)^2 + i c^\dagger_{\sigma,j} c^\dagger_{-\sigma,j+1} \left(n_{-\sigma,j} - n_{\sigma,j+1}\right)^2 \Big] + \mathrm{H.c.} \ , \end{aligned} \tag{2.3}$$

where t is the (single-particle) hopping parameter, Δ is an unconventional superconductivity order parameter (assumed real) that couples different spins in neighbour sites and W is the strength of 2 and 3-body interactions. The many-body interactions in Eq. (2.3) have different behaviors and can be seen as a competition in the system that tries to push the ground state away from the half occupation limit.

Let us briefly discuss the four interaction terms in Eq. (2.3) in more detail. The first is essentially a hopping term that is hindered when there are no electrons of opposite spins in the two hopping sites. As such, it can be understood as an effective two-body attraction between the electrons of opposite spins. The second term describes a p-wave supercon-

as broken symmetry phases since they do not satisfy the parafermion braiding. Here, and in chapter 3 we call them parafermions to simplify. Another possible nomenclature is poor's man parafermion or Non-topological parafermions [14].

ducting pairing which depends on the two sites having distinct opposite spin occupation numbers. This, in turn, thwarts the creation of a p-wave pair of a given spin unless there is a charge imbalance of electrons with opposite spin in the two sites. The third and forth terms are, respectively, three-body spin-orbit-like hopping and spin-mixing p-wave paring terms which contribute only when two neighboring sites have distinct occupation numbers of opposite spin.

This model has two important features. In the limit $t = \Delta = W \equiv t$, the Hamiltonian maps exactly [12] into a Kitaev-like chain of $\mathbb{Z}_4$ parafermions with two uncoupled parafermions at its ends, namely:

$$H_{\text{pf}} = -Je^{-i\pi/4}\sum_{j=1}^{L-1}\psi_j\chi_{j+1}^{\dagger} + \text{H.c.}\ . \tag{2.4}$$

where χ and ψ are $\mathbb{Z}_4$ parafermions satisfying $\chi_j^{\dagger} = \chi_j^3$, $\psi_j^{\dagger} = \psi_j^3$ and $\chi_j\chi_k = i\chi_k\chi_j$, $\psi_j\psi_k = i\psi_k\psi_j$ for $j < k$ and $\chi_j\psi_k = i\psi_k\chi_j$ for $j \leq k$. At the same time, the limit $t = \Delta$ with $W = 0$ gives a chain with two Majorana modes at each end ($2 \times \mathbb{Z}_2$) [12]. As such, we can explore trivial, $\mathbb{Z}_4$ and $2 \times \mathbb{Z}_2$ phases just by varying Δ and W.

We consider the case there the chain is coupled to an interacting quantum dot located at it's left end, as depicted in Fig. 2.1. The Hamiltonian of the full system is

$$H_{\text{Z}_4-\text{QD}} = H_{Z_4} + H_{\text{QD}} + H_{\text{pf}-\text{QD}}\ , \tag{2.5}$$

where

$$H_{\text{pf}-\text{QD}} = -\,t_d\sum_{\sigma=\uparrow,\downarrow} c_{\sigma,d}^{\dagger}c_{\sigma,1} - c_{\sigma,d}^{\dagger}c_{\sigma,1}^{\dagger} + \text{H.c.}\ , \tag{2.6}$$

$$H_{\text{QD}} = U_d n_{\uparrow,d}n_{\downarrow,d} + \epsilon_d(n_{\uparrow,d} + n_{\uparrow,d})\ . \tag{2.7}$$

In the above, $c_{\sigma,d}^{\dagger}$ ($c_{\sigma,d}$) represents a creation (destruction) operator for an electron of spin σ in the dot with $n_{\sigma,d} \equiv c_{\sigma,d}^{\dagger}c_{\sigma,d}$. $H_{\text{pf}-\text{QD}}$ in Eq. (2.6) represents the dot-chain coupling. Notice that it includes an Andreev-reflection term[2], similarly to the case of quantum dots coupled to chains hosting MZMs [109, 111]. In addition, the quantum dot Hamiltonian is given by Eq. (2.7), which contains an electron-electron repulsion term with strength by U_d[3] and a (tunable) single-particle energy level at ϵ_d. We take $t_d = 0.1t$ throughout the chapter as the results are qualitatively similar even for $t_d \sim t$.

[2]The choice of a minus sign in the Andreev-like coupling in Eq. (2.6) does not affect the results and any phase factor $e^{i\theta}$ would work, except $\theta = 0$ (plus sign). In this case we have an transition similar to what happens with Majoranas, but shifted by π.

[3]It is important to consider $U_d \neq 0$. Not only in experimental setups is hard to remove the contributions of electron-electron repulsion, but as it is shown later, most of the features that distinguish different phases arise due to the separation of Hubbard peaks that only happens when $U_d \neq 0$. On the same note, $U_d \gg t$ completely decouples the Hubbard peaks which makes it harder to distinguish the different phases.

The choice of the coupling between QD and chain is not a trivial one. The exotic nature of parafermion chain allows many non-trivial couplings, such as Fock-parafermion hoppings and generalized Andreev-like reflections that use Fock-parafermions. Although some of these hoppings produce unique signatures between the different phases, we chose to use Eq. (2.5) since it also appears in QD-Majorana chains and is more natural [109].

2.2 Phase diagram

The phase diagram of the system can be obtaining by following the many-body ground state degeneracies as well as the gap to the first excited states of either the chain-only or chain+quantum dot systems. We obtain the overall ground-states of the respective Hamiltonians with the DMRG method [20–22] as implemented within the ITensor package [113].

Ground-state degeneracy count plays an important role in distinguishing the two topological phases from the trivial one: while the ground state is four-fold degenerate in the first two, it is always non-degenerate in the latter. To this end, we determine the degeneracy of the ground state by counting the number of low-lying states within a window $\delta E \lesssim 10^{-6}t$. This value is well within the ground-state energy accuracy in the DMRG calculations given the bond dimension and chain lengths used (see section 2.2.1 for more details). It is also enough to characterize gap openings between the ground state and the first excited state, which, for the parameters used, are of order $\sim 10^{-3}t$ in the trivial phase and $\gtrsim 0.1t$ in the topological phases.

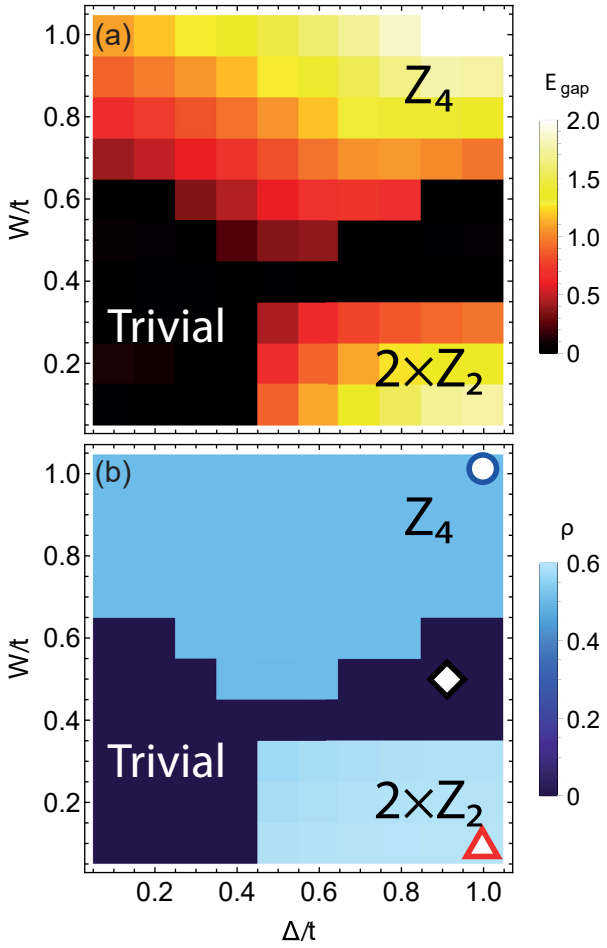

Figure 2.2: Phase diagrams of H_{Z_4}, Eq. (2.1). (a) Energy gap between ground and first excited states for a 20-site chain described by H_{Z_4}. (b) Quantum dot LDOS $\rho_d(0)/(2\pi)$ for a 20-site chain attached to the QD for $U_d/t = 1$ and $\epsilon_d = 0$. Symbols represent the Δ and W values used in the curves shown in Fig. 2.4.

In the chain-only case, the topological phases of H_{Z_4} were obtained by computing the gap between ground and first excited states of a 20-site chain[4]. These are shown in Fig. 2.2(a) for different values of the parameters W and Δ. Analytical solutions exist for three out of the four corners of the phase diagram, namely $\Delta/t = W/t = 1$, $\Delta/t = 1$, $W = 0$ and $\Delta = W = 0$. Those limits correspond respectively to topological phases $\mathbb{Z}_4$, $2 \times \mathbb{Z}_2$ and "trivial", i.e. a simple tight-binding chain. As Δ and W are varied, topological phase transitions occur as the gap goes to zero. By following these gap closings and comparing with the analytical limits, we can determine which region corresponds to each phase.

We stress that many-body interactions play an essential role in the transition to the $\mathbb{Z}_4$ parafermion phase. In fact, as can be seen in Fig. 2.2(a), the emergence of $\mathbb{Z}_4$ parafermionic modes occurs only for $W/t > 0.4$. Concurrently, $2 \times \mathbb{Z}_2$ Majorana phase occurs for weak

[4]Due to the system size and configuration, we probably don't observe Kondo effect and only observe Hubbard bands.

many-body interaction and a large values of the superconducting order parameter Δ.

2.2.1 Finite-size effects in the phase diagram.

As discussed in the previous section, determining whether two states are "degenerate" in the topological phases is an important aspect in constructing the phase diagram show in Fig. 2.2. The DMRG calculations were carried out using bond dimensions up to 100 (a value usually reached in the trivial phases only) and at least 15 sweeps to ensure convergence. A "noise term" was also used to improve convergence to the ground state, avoiding local minima.

Within these parameters, convergence was obtained within an energy accuracy of $\sim 10^{-8}t, 10^{-9}t$ within the topological phases, which justifies the criteria for considering two states to be degenerate if their energy difference is less than $10^{-6}t$. The energy gap was calculated with similar accuracy by targeting the first few excited states within the same block (no symmetries were considered in the calculations).

Although such energy gaps can be used to distinguish the topological phase transitions between trivial, $\mathbb{Z}_4$ and $2 \times \mathbb{Z}_2$ phases, some care must be taken regarding the system's size used. For small system sizes, the calculated "gap" might have more to to with the overlapping of the edge modes than with the actual "topological" gap. This is a similar to the famed "gap oscillations" in Majorana systems [82].

For instance, for $\epsilon_d = 0$, zero-energy states tends to localize at the dot site. This can be easily verified for the $\mathbb{Z}_4$ states where the sum of local density of states (LDOS) is constant and tends to be localized at the dot. Even though the sum of LDOS is not constant in the $2 \times \mathbb{Z}_2$ phase, this case also have localization, as we see the decrease of LDOS around half the chain close to the dot, see Section 2.3.1.

To illustrate this point, we consider an uncoupled chain described by the Hamiltonian in Eq. (2.1). The dependence of the gap to chain's size is shown in Fig. 2.3. An exponential decay in the gap, similar to that predicted for Majorana bound states [82], appear in both topological phases. The jumps in the gap are artifacts introduced by the cutoff energy δE which we use to consider two different energies to be equal. This means that when $E_{gap} < \delta E$ we assume E_{gap} to be zero and we use the next state to calculate the gap. Because of this, when we see the jump in the gap we also observe an increase in the ground-state degeneracy.

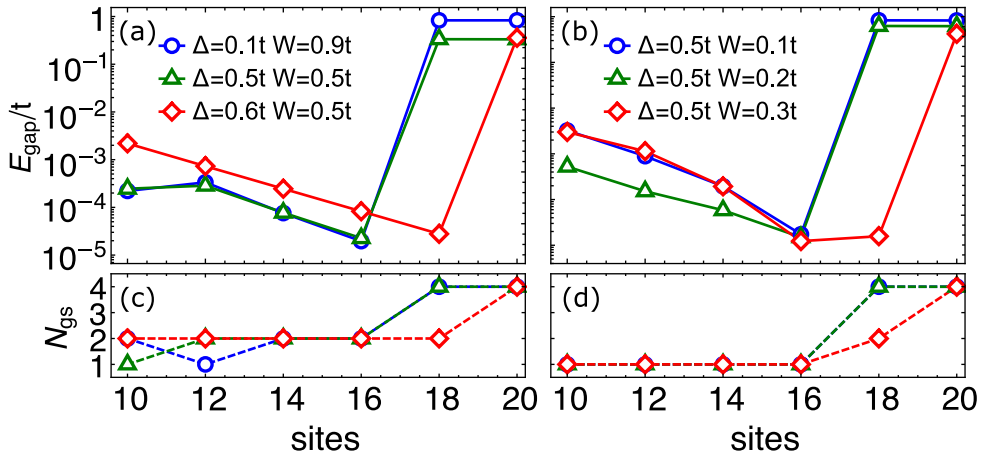

Figure 2.3: Finite size effects are more prominent in the system without quantum dots. The exponential decay of E_{gap} with the number of sites of the chain, depends not only on the phase (a) $\mathbb{Z}_4$ and (b) $2 \times \mathbb{Z}_2$, but also on the values of Δ and W.

The decay rate with system size at each phase is non-universal and depends on the model's parameters. In Fig. 2.3(a) ($\mathbb{Z}_4$ phase), there are clearly two behaviors, with the gap closing at different rates for $\Delta = 0.6$ and $\Delta \leq 0.5$. Small deviations from a pure exponential decay are also present, particularly in the $2 \times \mathbb{Z}_2$ phase (Fig. 2.3(b)). These are probably associated with the details on how the $2 \times \mathbb{Z}_2$ edge states spread along the chain and overlap with each other. Additionally, some of the "gap closings" are, in fact, the formation of a doublet, as illustrated if Fig. 2.3(b) for $\Delta = 0.5t$ and $W = 0.3t$: between $N = 16$ and $N = 18$, the ground state degeneracy goes from 1 to 2.

2.3 Parafermion detection

Detecting topological phase transitions by monitoring the gap and ground state degeneracies can be a challenging task. Not only it is difficult to tell the $\mathbb{Z}_4$ and $2 \times \mathbb{Z}_2$ topological phases from each other but also finite-size effects can be an issue, as discussed in the previous section. Interestingly, we find that these phases can be also be probed by accessing the local density of states of a quantum dot side-coupled to the system. The dot's occupation can also be used to differentiate the phases, making the dot an ideal platform to detect parafermions. Together, these features can give a clearer experimental signature of the topological phase transitions in the system.

More importantly, our results establish a one-to-one correspondence between the zero-energy density of states and the different topological and non-topological phases, allowing for a clear signature of the presence or absence of PZMs in the chain. This correspondence is nicely illustrated by comparing Figs. 2.2(a) and (b) and constitute one of the main results of this chapter.

2.3.1 Local density of states

The local density of states for a given site in the chain can be accessed by tracking the matrix elements of the local fermionic operators between the $N_{\rm gs}$ ground states of the system [12, 88]. We follow this route to obtain the QD LDOS[5] from the zero-energy spectral function given by:

$$\rho_d(0) = \frac{2\pi}{N_{\rm gs}} \sum_{\sigma,|g\rangle,|g'\rangle} |\langle g| c^\dagger_{\sigma,d} |g'\rangle|^2 + |\langle g| c_{\sigma,d} |g'\rangle|^2 , \tag{2.8}$$

where we sum over all ground states $|g\rangle$,$|g'\rangle$ of $H_{\mathrm{Z}_4-\mathrm{QD}}$ (Eq. (2.5)). Notice that $\rho_d(0)$ depends only on matrix elements involving the system's ground states, even for $\epsilon_d \neq 0$. In practice, the sum in Eq. (2.8) is comprised of $N_{\rm gs}$ terms which turn out to be equal. Thus, it is sufficient to calculate only one of these terms for a given fixed "reference" ground state $|g'\rangle \equiv |0\rangle$, which we choose as the first state with the lowest energy computed by DMRG.

We can compare the phase diagram due the gap to the phase diagram due the dot's zero-energy DOS, Fig, 2.2(b). The LDOS phase diagram was obtained for $U_d/t = 1$, $\epsilon_d = 0$ and $\rho_d(0)$ assumes a characteristic, near constant, non-zero value at each of the topological phases while it drops to zero in the transition to the trivial phase.

The characteristic values of $\rho_d(0)$ on each topological phase depend on U_d and ϵ_d, as shown in Fig. 2.4. As a general feature, $\rho_d(0)$ displays peaks at $\epsilon_d = 0$ and $\epsilon_d = -U_d$, as shown in Fig. 2.4(a) in the topological phases. Generically, $\rho_d(0)$ can distinguish the different phases by gate-tuning the quantum dot to the single-occupation regime $-U_d < \epsilon_d < 0$. In fact, tuning the dot to the particle-hole symmetric point $\epsilon_d = -U_d/2$ can maximize its sensibility to distinguish the different phases. Here, the $\rho_d(0)$ value at the $2 \times \mathbb{Z}_2$ is nearly twice that of the value at the $\mathbb{Z}_4$ phase. Fig. 2.4(b) shows $\Delta\rho_d(0) = (\rho_d(0,\epsilon_d) - \rho_d(0,-U_d/2))/\rho_d(0,-U_d/2)$ around the particle-symmetric point. This sharp feature, which leads to illustrates that the LDOS variation that can be used to clearly distinguish the different topological phases: a discontinuity in the LDOS first derivative with respect to ϵ_d appears in the $\mathbb{Z}_4$ phase, while the $2 \times \mathbb{Z}_2$ phase is featureless around $\epsilon_d = -U/2$.

The values of $\rho_d(0)$ at the peaks can be used to differentiate the $\mathbb{Z}_4$ and $2 \times \mathbb{Z}_2$ phases. While the $\mathbb{Z}_4$ phase has a value of $\rho_d(0)/2\pi \sim 0.5$ at the peaks the $2 \times \mathbb{Z}_2$ phase has a larger value $\rho_d(0) \sim 0.58$ for $U_d/t = 1$. These values are a consequence of the strong localization of the ground state in both phases (at least half of the total spectral weight) at the QD site. This situation is similar to the "leaking" of Majorana bound states into quantum dots studied in Refs. [109, 110].

The "leaking" is stronger for the case of MZMs ($2 \times \mathbb{Z}_2$ phase) than for PZMs ($\mathbb{Z}_4$

[5]The QD LDOS can be obtained with conductance measurement [114].

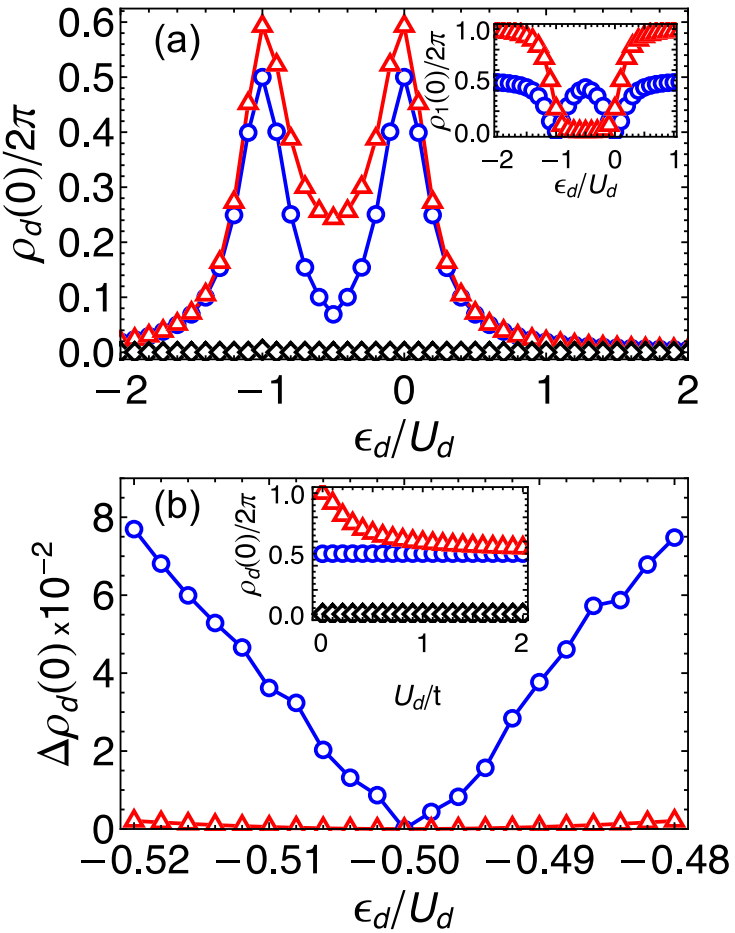

Figure 2.4: (a) QD LDOS versus ϵ_d calculated for $U_d/t = 1$ and chain parameters corresponding to the symbols marked in Fig. 2.2(b): $W/t = \Delta/t = 1$ (blue circles, $\mathbb{Z}_4$ phase); $\Delta/t = 1$, $W = 0$ (red triangles, $2 \times \mathbb{Z}_2$ phase); $W/t = 0.5$, $\Delta/t = 0.9$, (black diamonds, trivial phase). The inset shows the LDOS at the first site of the chain for the same parameters. (b) $\Delta\rho_d(0)$ near $\epsilon_d = -U_d/2$. Note the sharp feature in the $\mathbb{Z}_4$ LDOS curve, which is absent in the $2 \times \mathbb{Z}_2$ one. The Inset shows the LDOS maximum for different values of U_d. Only the maximum of $2 \times \mathbb{Z}_2$ phase has dependency with U_d.

phase). This is illustrated in the inset of Fig. 2.4(a) which shows the LDOS at the first site of the chain $\rho_1(0)$. For the $\mathbb{Z}_4$ phase, we find $\rho_1(0) = \pi - \rho_d(0)$, reaching $\rho_1(0) \approx \pi$ and $\rho_d(0) \approx 0$ (localized in the chain rather than in the dot) for $\epsilon_d = -U_d/2$ and $\epsilon_d > 0$, $\epsilon_d < -U_d$. This indicates that the PZM "leaks" into the dot only at the Coulomb peaks $\epsilon_d = 0, -U_d$. In the $2 \times \mathbb{Z}_2$ phase, by contrast, $\rho_1(0) \sim 0$ for $-U_d < \epsilon_d < 0$, implying a much stronger leaking of the two MZMs into the dot.

We also explored the effects of on-site disorder in the interacting chain in section 2.5. Our calculations show that, as long as the parafermionic modes are not destroyed, the effect of disorder amounts essentially to a constant shift in ϵ_d . If such shift is taken into account, the all the signatures in the QD properties discussed above are robust against disorder.

Moreover, the $\rho_d(0)$ value in the $\mathbb{Z}_4$ phase is essentially independent of the electron-electron interaction in the dot U_d, as shown in the inset of Fig. 2.4(b) for $\epsilon_d = 0$. By contrast, increasing values of U_d tend to decrease the $\rho_d(0)$ value at the $2 \times \mathbb{Z}_2$ $\rho_d(0)$. This indicates that QDs with $U_d \sim t$ can be more efficient in distinguishing the different topological phases.

2.3.2 Dot occupation

As discussed above, the stronger signatures of PZMs in the dot LDOS occur precisely at the points where the dot's occupancy changes, either from from unoccupied to singly occupied ($\epsilon_d \approx 0$) as well as from singly occupied to doubly occupied ($\epsilon_d \approx -U_d$). In fact, one can track the presence/absence of PZMs in the chain by monitoring the average occupation of the quantum dot[6].

This is shown in Fig. 2.5(a), where we show the zero-temperature dot occupancy $\langle n_d \rangle$ versus ϵ_d for each of the phases at $W/t = \Delta/t = 1$ ($\mathbb{Z}_4$), $W/t = 0$ $\Delta/t = 1$ ($2 \times \mathbb{Z}_2$), $W/t = 0.5$ $\Delta/t = 0.9$ (trivial), shown in the phase diagram. Although the overall behavior of the occupancy is similar, with well-defined occupancy plateaus as a function of ϵ_d, there are subtle differences depending on the phase of the system.

For instance, while both trivial and $2\times\mathbb{Z}_2$ phase display a smooth change in occupation number around the symmetric point $\epsilon_d = -U_d/2$, in the $\mathbb{Z}_4$ phase the occupancy jumps from around 0.96 at $\epsilon_d > -U/2$ to exactly 1 at $-U/2$ than to 1.04 at $\epsilon_d < -U/2$, (inset of Fig. 2.5(a))[7]. This discontinuity arises due to the transfer of spectral weight as the $\mathbb{Z}_4$ parafermion "leaves" the dot precisely at $\epsilon_d = -U_d/2$, and "re-enters" at other value[8]. The same is not true for the $2 \times \mathbb{Z}_2$ spectral weight: this state' contribution for the dot

[6]For each ϵ_d value, we calculate the occupation number for each ground state and them take the average.

[7]We verified that similar results were obtained for more generic parameters.

[8]This probably arises from a quasi-particle peak crossing the Fermi energy. NRG calculations could give more information about it.

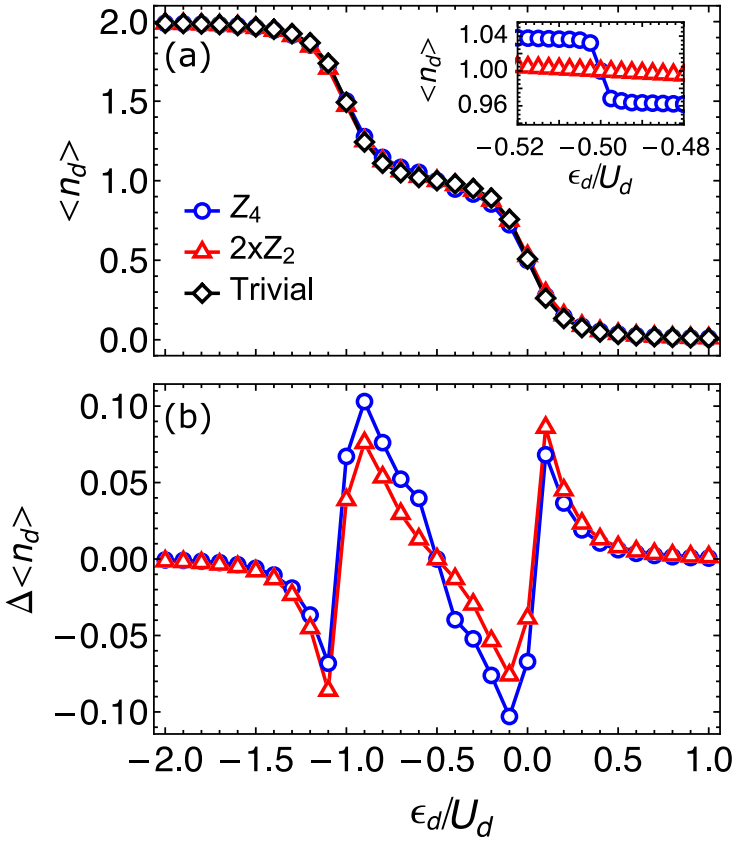

Figure 2.5: (a) QD occupancy $\langle n_d \rangle$ vs ϵ_d for the same parameters as in Fig. 2.4. Inset: enhancement showing a discontinuity in $\langle n_d \rangle$ calculated at the $\mathbb{Z}_4$ phase at $\epsilon_d = -U/2$. (b) Occupancy difference between topological and trivial phases.

LDOS is suppressed but does not reach zero, implying a continuous occupation number as a function of ϵ_d.

In all cases, we confirmed that there is no spin-polarization in the occupancy (namely $\langle n_{d\uparrow} \rangle = \langle n_{d\downarrow} \rangle$). In addition, on-site disorder in the chain does not affect the features in the occupancy around $\epsilon_d = -U_d/2$ for both $\mathbb{Z}_4$ and $2 \times \mathbb{Z}_2$ phases (see section 2.5 for details).

The distinction between the curves at the different phases can be better appreciated by subtracting $\langle n_d \rangle(\epsilon_d)$ from the trivial case, $\Delta\langle n_d \rangle \equiv \langle n_d \rangle - \langle n_d \rangle_{\text{trivial}}$, as plotted in Fig. 2.5(b). In particular, $\Delta\langle n_d \rangle$ changes rather strongly near the inflection points $\epsilon_d = 0, -U_d$, allowing one to differentiate the topological phases from trivial one.

2.4 Comparison with analytic results

In order to better understand in DMRG results, we use an analytical perturbative approach to describe the changes in the $\mathbb{Z}_4$ topological phase in the presence of the coupling to the quantum dot.

Our approximation consists in considering the analytic results for the (four-fold degenerate) ground state $|g^{(0)}\rangle$ of H_{pf} given by Eq. (2.4) (which describes the $\mathbb{Z}_4$ phase of

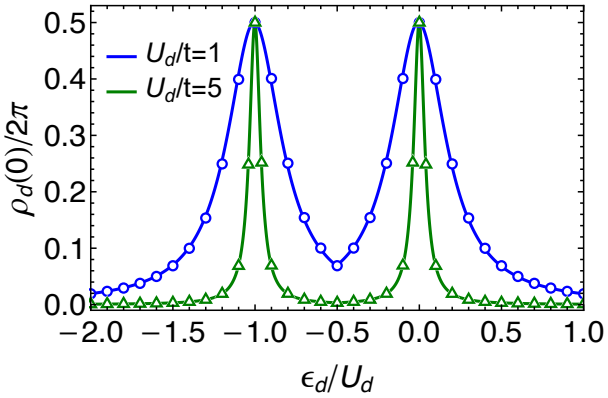

Figure 2.6: Comparison between the first-order approximation approach (lines) and DMRG results (symbols) for the $\mathbb{Z}_4$ phase with $U_d/t = 1$ (blue), and $U_d/t = 5$ (green).

H_{Z_4} at $\Delta = W = t$) and calculate the first-order correction due to the coupling t_d to the quantum dot given by Eqs. (2.6)-(2.7). The resulting corrected states $|g^{(1)}\rangle$ are then used in Eq. (2.8) to obtain an approximation for the dot LDOS $\tilde{\rho}_d(0)$. Details of this procedure are given in Appendix B.

One of the artifacts of the approximation is that $\{|g^{(1)}\rangle\}$ is now split into two doublets of Fock-parafermion dot states, with an energy splitting of order $\sim t_d/t$ (see Appendix B). Nonetheless, by considering the the lowest energy doublet and calculating the dot LDOS from Eq. (2.8), one obtains an excellent agreement with the DMRG calculations, as shown in Fig. 2.6.

The LDOS calculated within the analytic approximation can shed some light on the distinct signatures of the presence of PZMs, namely the peaks at $\epsilon_d = 0, -U_d$. By closely looking at the perturbed ground state doublet we find that both Fock-parafermion states have the same components precisely for $\epsilon_d = 0, -U_d$. This matches what one expects for a PZM localized in the dot: an equal-weight linear combination of Fock-parafermion states.

2.5 On-site disorder in the chain.

In real experimental setups, disorder can play a crucial role in masking the signatures of topological excitacions. In fact, this has been the case of Majorana zero modes in semiconducting nanowires, in which strong disorder effects can produce zero-bia signatures even in the non-topological phases [80]. Thus, it is interesting to check whether the signatures proposed in the paper would be robust against on-site disorder in the chain.

In order to account for disorder effects in our system, we add a local random chemical potential μ_i at each chain site. We consider the system to have "weak" disorder if $\langle \mu_i \rangle \approx 0.1t$ or "strong" disorder if $\langle \mu_i \rangle \approx t$. After generating the random profile of μ_i, we calculate the spectral function, Eq. (2.8), using all ground states to avoid any potential bias.

In Fig. 2.7(a,c) we show the spectral function for 6 different realizations of random

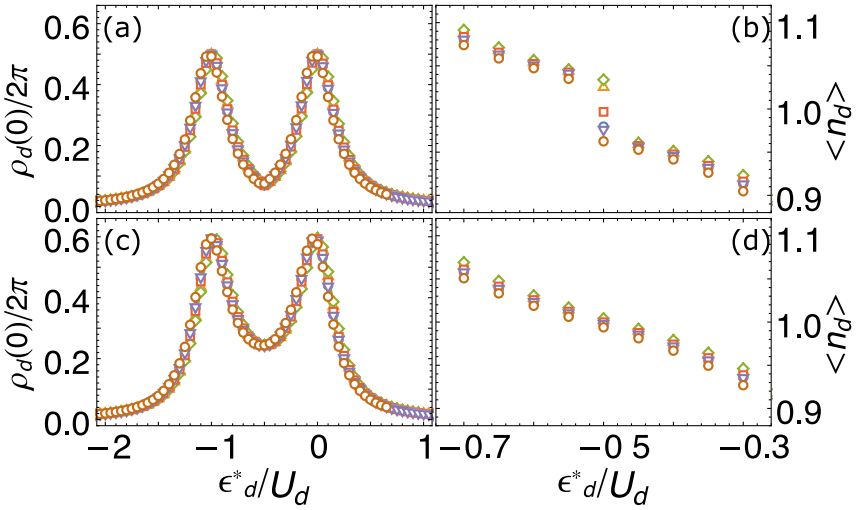

Figure 2.7: Spectral function and average occupation number for different random potentials. The $\mathbb{Z}_4$ phase (a) spectral function and (b) average occupation number are similar to a clean sample. The same is true for $2 \times \mathbb{Z}_4$ (c) spectral function and (d) average occupation number.

potentials, 3 of them with weak disorder and 3 with strong disorder. The only effect we observe is a shift in the dot's energy from ϵ_d to $\epsilon_d^* = \epsilon_d + \mu^*$, where μ^* is a constant that depends upon the μ_i distribution.

The results indicate that the proposed quantum dot measurements are very robust against disorder: the same profile of Fig. 2.4(a) is obtained for both weak and strong disorders. The $\mathbb{Z}_4$ and $2 \times \mathbb{Z}_2$ phases have the same parameter as Fig. 2.4(a), as showed in the main text, these parameters should be enough to represent all the phases. Moreover, on-site disorder in the chain does not affect qualitatively the average occupation number. Similar to the clean sample, $\mathbb{Z}_4$ states have a discontinuity around $\epsilon_d^* = 0.5t$, while $2 \times \mathbb{Z}_2$ states do not have discontinuity. This shows that both measurements are disorder-resistant and can be applied in real-life situations to discern $\mathbb{Z}_4$ and $2 \times \mathbb{Z}_2$ states.

Chapter 3

Fermionic $\mathbb{Z}_3$ parafermion

In this chapter, we explore a fundamental question in the search for parafermion bound states. Is there any tight-biding model that can generate a parafermion, be it topological or not, that hosts $\mathbb{Z}_3$ edge states? While previous studies have shown the existence of $\mathbb{Z}_4$ parafermion bound states [12, 13], a $\mathbb{Z}_N$ parafermion with odd N appears to be more elusive. The importance of odd N is that the parafermion bound state cannot condensate into a Majorana bound state with a broken symmetry [115]. Therefore, if it is topological, it must have a different braiding of Majoranas. Moreover, for a prime N we can either have the $\mathbb{Z}_N$ parafermion or a nontopological state.

Here, we address the existence of fermionic $\mathbb{Z}_3$ parafermion by proposing a new Hamiltonian that hosts $\mathbb{Z}_3$-symmetric localized edge state. Our proposal uses strong local electron-electron interaction such that no double-occupancy is present (t-J limit). In a sense, the restriction to zero and singly occupied states plays a similar role as the restriction to "spinless" fermions in the early proposals for Majorana bound states in semiconductor nanowires [1, 28, 60, 61]. Although the proposed Hamiltonian could, therefore, be considered only a toy model, we believe it could in principle be studied using optical lattices.

In order to characterize the parafermionic phase, we use DMRG [21, 22, 113] to numerically calculate the energy gap, the entanglement entropy (E.E.), and the local spectral functions of the strongly correlated fermionic models. In addition, we study the stability of $\mathbb{Z}_3$ parafermions under the effect of local doping and Zeeman terms, which can be important for the prospects of parafermion-based topological quantum computation. We find that the parafermionic zero modes are stable against such local perturbations as long as these terms preserve the $\mathbb{Z}_3$ symmetry. This chapter is adapted from *"Edge $\mathbb{Z}_3$ parafermions in fermionic lattices"*, Phys. Rev. B 105, 195121 (2022).

3.1 Models

In this section, we propose a spinful fermionic model supporting $\mathbb{Z}_3$ parafermionic edge modes. As previously discussed, the intrinsic difficulty in devising such a system is that the Hamiltonian must conserve parity symmetry ($\mathbb{Z}_2$) and, at the same time, conserve a $\mathbb{Z}_3$ symmetry of the parafermionic modes. A possible solution is that the $\mathbb{Z}_3$ parafermionic modes emerge in a situation in which the parity of the different ground states is set by the number of sites in the chain. As we shall see, this is indeed the case in the proposed fermionic lattice models.

We begin by considering a fermionic spinful model with infinitely large on-site Hubbard repulsive interactions. In this limit, we can safely exclude the doubly-occupied state in the local Hilbert space of each site, a procedure akin to that used in the derivation of the $t-J$ model [116]). The Hamiltonian reads

$$H_I = H^{(2)} + H^{(4)} + H^{(6)} \,, \tag{3.1}$$

with

$$H^{(2)} = \sum_{\substack{j=1 \\ \sigma=\uparrow,\downarrow}}^{L-1} -t\tilde{c}^\dagger_{\sigma,j}\tilde{c}_{\sigma,j+1} - \Delta\tilde{c}^\dagger_{\sigma,j}\tilde{c}^\dagger_{-\sigma,j+1} + \text{H.c.}, \tag{3.2}$$

$$H^{(4)} = -W_4 \sum_{j=1}^{L-1} s^+_j s^-_{j+1} + \text{H.c.} \,, \tag{3.3}$$

$$H^{(6)} = -W_6 \sum_{j=2}^{L-1} s^+_{j-1} s^+_j s^+_{j+1} + \text{H.c.} \,. \tag{3.4}$$

Where $\tilde{c}_{\sigma,j} = c_\sigma(1-n_{-\sigma,j})$ is the $t-J$ basis annihilation operator in terms of usual fermionic operators [116]. It satisfies all but one fermionic anti-commutation relation, namely $\{\tilde{c}^\dagger_{\sigma,j}, \tilde{c}_{-\sigma,j}\} = \tilde{c}^\dagger_{\sigma,j}\tilde{c}_{-\sigma,j}$ instead of the usual 0.

In the above, $s^+_j(s^-_j) = \tilde{c}^\dagger_{\uparrow,j}\tilde{c}_{\downarrow,j}(\tilde{c}^\dagger_{\downarrow,j}\tilde{c}_{\uparrow,j})$ is the spin-flip operator, t is the single-particle hopping, Δ is a p-wave-like superconducting order parameter that mixes spins in neighbor sites, W_4 is the strength of a synchronized spin-flip in two neighbor sites, while W_6 is the strength of synchronized spin flip in the three closest sites. We note that the three-body interaction contained in $H^{(6)}$ is an important ingredient for the existence of $\mathbb{Z}_3$ parafermions.

The Hamiltonian H_I given by Eq. (3.1) has $S_3 = \mathbb{Z}_3 \rtimes \mathbb{Z}_2$ symmetry, where the $\mathbb{Z}_2$ part comes from spin flip and the $\mathbb{Z}_3$ component stems from the generalized three-valued "parity" operator:

$$\hat{P}_{\mathbb{Z}_3} = \omega^{\sum_{j=1}^{L}(n_{\uparrow,j}+2n_{\downarrow,j})} \tag{3.5}$$

where $\omega = e^{2\pi i/3}$ and $n_{\sigma,j} = \tilde{c}^{\dagger}_{\sigma,j}\tilde{c}_{\sigma,j}$ is the fermionic number operator at site j.

One can readily check that $\hat{P}^{\dagger}_{\mathbb{Z}_3} H_I \hat{P}_{\mathbb{Z}_3} = H_I$. More importantly, as further discussed in Sections 3.2 and 3.3, the ground states of H_I are also eigenstates of $\hat{P}_{\mathbb{Z}_3}$ and, in the $\mathbb{Z}_3$ phase, two out of the three ground states are related by a spin-flip transformation. These states can be split by an out-of-plane local Zeeman term which breaks the corresponding $\mathbb{Z}_2$ symmetry.

The next step is to check under which conditions H_I can be related to a benchmark Hamiltonian supporting $\mathbb{Z}_3$ parafermionic edge modes. To this end, we can use a Kitaev-like $\mathbb{Z}_3$ parafermion chain [6, 117], the Hamiltonian of which is given by

$$H_{pf} = -J \sum_{j=1}^{L-1} \psi_j \chi^{\dagger}_{j+1} + \text{H.c.}, \tag{3.6}$$

where each site has two parafermion modes ψ and χ satisfying parafermionic identities $\psi^{\dagger}_j = \psi^2_j$, $\chi^{\dagger}_j = \chi^2_j$ and $\chi_j\psi_j = \omega\psi_j\chi_j$. For different sites, they satisfy a parafermionic exchange algebra $\psi_l\psi_j = \omega\psi_j\psi_l$, $\chi_l\chi_j = \omega\chi_j\chi_l$ and $\chi_l\psi_j = \omega\psi_j\chi_l$ for $l < j$.

This model is exactly solvable for any $J > 0$, showing a threefold ($\mathbb{Z}_3$ symmetric) degenerate ground state [6, 88, 117]. Moreover, one can show that H_{pf} can be written in terms of fermionic operators (see Appendix C) yielding a similar Hamiltonian as that of Eq. (3.1).

We note that fermionization of H_{pf} produces a parity-violating interaction term $H^{(3)}$ given by

$$H^{(3)} = -W_3 \sum_{\substack{j=1 \\ \sigma=\uparrow,\downarrow}}^{L-1} (-1)^{\sum_{p<j} n_p} \left[\tilde{c}_{\sigma,j}\tilde{c}^{\dagger}_{-\sigma,j+1}\tilde{c}_{\sigma,j+1} + \tilde{c}^{\dagger}_{\sigma,j}\tilde{c}_{-\sigma,j}\tilde{c}^{\dagger}_{\sigma,j+1} \right] + \text{H.c.}. \tag{3.7}$$

This term corresponds to an exotic process of creation (annihilation) of an electron together with a spin flip in the neighboring site. As such, it does not conserve either parity or electron number. In fact, this term can be understood as an approximation of the mean-field interaction of the term $H^{(6)}$ given by Eq. (3.4) in which the parity is spontaneously broken (see Appendix D) .

We thus define Hamiltonian H_{II} as

$$H_{II} = H^{(2)} + H^{(4)} + H^{(3)} \, . \tag{3.8}$$

For $J := t = \Delta = W_4 = W_3$, it can be shown that $H_{II} \to H_{pf}$ (see Appendix C for details). In this special limit, the ground state can be obtained analytically [88].

We should point out that the long-range interaction terms in H_{II} do not prevent the existence of a topological phase [118, 119]. In the present case, not only are there free parafermionic edge operators (χ_1 and ψ_L) which couple the different ground states but

also the ground states are indistinguishable by local probes, satisfying the criteria for topological order [42].

Although H_{II} can be obtained from a mean-field-like form of H_I, it is not *a priori* clear that H_I should have a $\mathbb{Z}_3$ topological phase. The deep connection of the fermionic model of Eq. (3.1) and the parafermionic chain of Eq. (3.6) constitutes one of the main results of this chapter and it is discussed in detail in Section 3.2.

3.2 Equivalence of the models

The existence of a $\mathbb{Z}_3$ phase in the Hamiltonian H_I can be established by two complementary methods. First, we show that there is a phase transition in which the ground state of the system goes from nondegenerate to threefold degenerate that is accompanied with the closing of bulk gap. Then we show that in this threefold degenerate phase it is possible to smoothly deform H_I into H_{II} in a regime of parameters in which it displays the same $\mathbb{Z}_3$ parafermion phase as H_{pf}.

These two methods, together with the existence of gapless edge states and the indistinguishability of ground states by local operators (discussed in Sec. 3.3.3) and the protection against disorder and single impurities that preserve $\mathbb{Z}_3$ symmetry (Sec. 3.3) are strong evidences of the existence of a $\mathbb{Z}_3$ topological phase in both H_I and H_{II}[1]. To confirm the non-trivial topological phase, iDMRG [120–122] should be used or maybe even Bott index [123][2].

3.2.1 Gap closing at the transition

The different phases can be characterized by two main quantities: the ground state degeneracy n_{gs} and the energy gap E_{gap} between the ground state and the first excited (many-body) state. To this end, the ground states of the fermionic Hamiltonians are calculated for the different model parameters with the DMRG method [20–22] via the ITensor package [113]. In the remainder of the chapter, we use $t=\Delta=W_4$ and a 100-site chain, unless otherwise specified.

We obtain n_{gs} in the DMRG calculations by counting the number of low-lying states within a window $\delta E \lesssim 10^{-3}t$ of the ground state energy (the hopping t is the energy unit). This value is well within the ground state energy accuracy in the DMRG calculations

[1] As consequence of long-range interaction as well as strong electron-electron interactions, the topological phase might note be present in the tenfold classification [89]. This is similar to parafermion bound states in fractional quantum Hall having different topological phases, compared to the tenfold classification, due to long-range introduced by bosonization [14] and discussed before.

[2] We do nonetheless call this state topological and parafermion as it comes from a real topological Z_3 parafermion chain [6], however the issue lies in a non-local map between parafermion operators and $t-J$ operators which can change the topological nature of the ground state.

given the bond dimension and system's size. It is also enough to calculate E_{gap} for the parameters used, $E_{\text{gap}} \gtrsim 10^{-2}t$ for all cases.

Results for E_{gap} for Hamiltonians H_I and H_{II} as a function of W_6 and W_3 respectively are shown in Fig. 3.1. Figure 3.1(a) shows E_{gap} for H_I as a function of W_6. For small values of W_6, the system is in the trivial regime and has a small gap ($\sim 10^{-2}t$) which we attribute to finite-size effects in a gapless phase. For $W_6 \approx 2t$, the system undergoes a phase transition[3], characterized by a sharp decrease in E_{gap} ("gap closing").

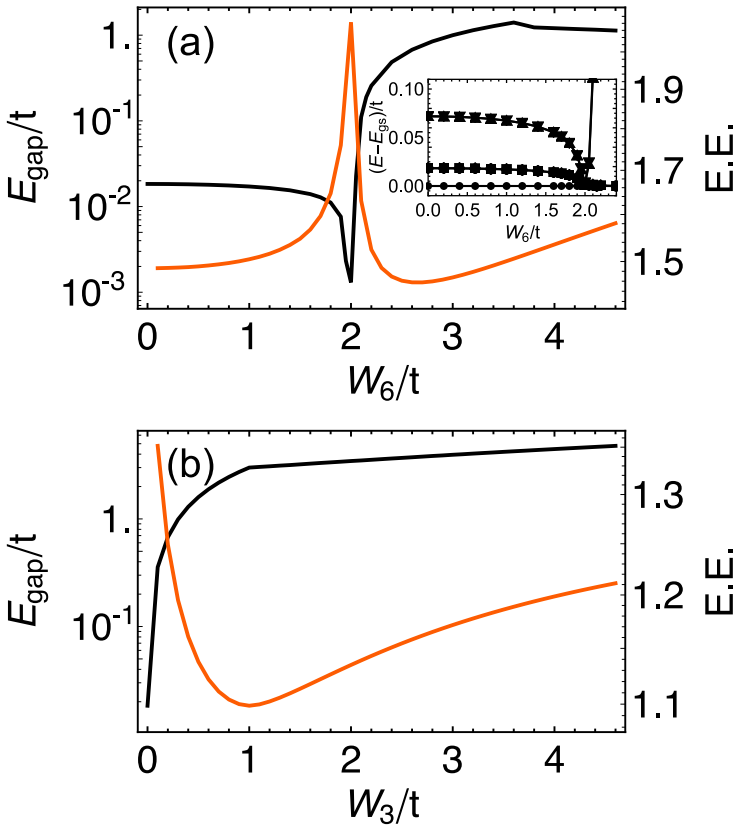

Figure 3.1: Gap (black) and entanglement entropy (red) as a function of interaction strength (a) W_6 and (b) W_3 for the models described by H_I and H_{II} respectively. While the phase transition occurs at $W_6 > 2t$ in H_I, any $W_3 > 0$ induces the $\mathbb{Z}_3$ phase in H_{II}. The inset in panel (a) shows the difference in energy level between the 5 states with lower energy (E) and the ground state energt E_{gs}. Note that all the states converge around the phase transition.

The phase transition becomes evident by plotting the low-lying energy levels as a function of W_6 (inset Fig. 3.1(a)). For $W_6 \gtrsim 2t$, the single ground state and a pair of higher energy states merge, abruptly increasing the degeneracy from $n_{\text{gs}} = 1$ to 3. The other higher energy states also close the gap at the same point and reopen, cindicating the bulk gap closes at the transition.

The threefold ground state degeneracy characterizes the new phase as a $\mathbb{Z}_3$ (topologi-

[3]Around $W_6 = 2t$ we used steps of $0.05t$ to plot figure 3.1(a).

cal) phase. The closure of the gap shown in Fig. 3.1(a) is accompanied by a discontinuity in the first derivative of the entanglement entropy E.E[4].

To compute the entanglement entropy, we perform DMRG calculations fully preserving the $\mathbb{Z}_3$ symmetry. We calculate the entanglement spectrum, by, first, gauging the matrix product state at the central bond then we SVD this wavefunction to obtain the density-matrix eigenvalues, p_n. We obtain the spectrum by applying the von Neumann formula to the squares of the singular values, $\lambda_n = -p_n^2 \ln(p_n^2)$. The entanglement entropy is the sum of all λ_n[5].

At the $\mathbb{Z}_3$ phase, all ground states have a well defined $\mathbb{Z}_2$ parity which depends on the length L of the chain as $\hat{P}_{\mathbb{Z}_2} = (-1)^{\sum_i^L (n_{\uparrow,i}+n_{\downarrow,i})} = (-1)^{L \bmod 2}$. Moreover, these ground states are characterized by a $\mathbb{Z}_3$ parity operator $\hat{P}_{\mathbb{Z}_3} = \omega^{\sum_i^L (n_{\uparrow,i}+2n_{\downarrow,i})}$ defined in Eq. (3.5). The different ground states can be distinguished by the respective eigenvalue of $\hat{P}_{\mathbb{Z}_3}$, which can be $1, \omega$ or ω^2. For this reason, the $\mathbb{Z}_3$ phase can not be understood as a simple combination of a Majorana-hosting phase together with a $\mathbb{Z}_2$ broken symmetry phase as it is the case for $\mathbb{Z}_4$ parafermions [12, 13, 17]. An important consequence is that a spin-flip transformation swaps the sectors $\langle \hat{P}_{\mathbb{Z}_3} \rangle = \omega$ and ω^2, while $\langle \hat{P}_{\mathbb{Z}_3} \rangle = 1$ is mapped into itself. This translates into the formation of doublets in the excited states.

A similar analysis can be made for H_{II}, by plotting E_{gap} for increasing W_3 with $t = \Delta = W_4$ (Fig. 3.1(b)). The main difference is that the critical value in which the system goes from the trivial to $\mathbb{Z}_3$ phase is $W_3 = 0$. As such, for any $W_3 > 0$ the system is in the $\mathbb{Z}_3$ phase and no phase transition takes place for nonzero values of W_3, as indicated by the absence of a peak in the entanglement entropy. In fact, the E.E. reaches its minimum value ($\ln(3)$) for $W_3 = t$, precisely the point where the mapping of H_{II} to the parafermion chain Hamiltonian H_{pf} is exact.

3.2.2 Entanglement spectrum and finite-size effects

In order to better understand the nature of the ground state, we turn to the entanglement spectrum of H_I. Fig. 3.2(a) shows the largest eigenvalues of the reduced density matrix ($\lambda_n > 5 \times 10^{-6}$) calculated with DMRG in the sector $\langle \hat{P}_{\mathbb{Z}_3} \rangle = 1$ for $W_6 = 3.2t$ and $L = 100$ sites. As a general feature, the spectrum is threefold degenerate, as it would be expected for a $\mathbb{Z}_3$ phase [14]. The same result is obtained for the other parity sectors.

We point out in passing that a similar result is obtained for H_{II}. In particular, at the point $W_3 = t$, the system is maximally entangled with bond dimension 3, i.e., only three nonzero λ_n, all equal to 1/3.

Due to intraedge coupling of the edge states, the gap calculation of H_I is prone to finite-size effects, as shown in Fig. 3.2(b). We note that there are two distinct regimes,

[4]Entanglement entropy measures how much two subsystems are entangled, for pure states it is zero while mixed states have non-zero.

[5]The implementation is described in the ITensor documentation [113].

with the gap decaying faster for $L \gtrsim 70$ sites. This indicates that the decay for $L \lesssim 60$ is mainly due to a decreasing in the intraedge overlap of the edge modes, which is also consistent with the spectral function results discussed in Section 3.3.3.

This is in striking contrast with the case of H_{II}, where the edge modes are much more localized. In fact, since H_{II} is exactly mapped in H_{pf}, there is no dependence of the gap size with the chain length. This is clearly not the case for H_I, which needs large chains such that finite-size effects can be neglected.

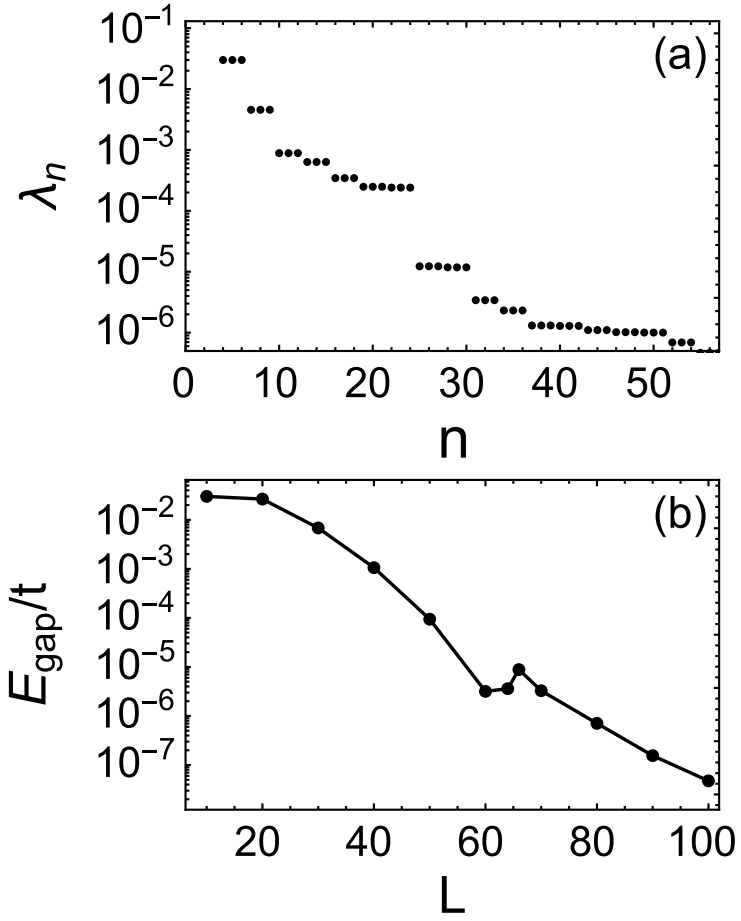

Figure 3.2: Characterization of H_I with $W_6 = 3.2t$. (a) Entanglement spectrum for the ground state in the sector $\langle \hat{P}_{\mathbb{Z}_3} \rangle = 1$ for a chain with $L = 100$ sites; the spectrum has a threefold degeneracy and is the same for other sectors. (b) Gap between the ground states due to the finite size of a chain with L sites; note that there are two different behaviors for $L \lesssim 60$ and $L \gtrsim 70$ indicating two mechanisms of intraedge interaction.

3.2.3 Deforming H_I into H_{II}

In order to confirm that the limits of large W_6 for H_I and large W_3 for H_{II} correspond to the same topological $\mathbb{Z}_3$ phase, we consider the following Hamiltonian:

$$H'(x) = (1 - x)H_I + xH_{II}, \tag{3.9}$$

which is equal to H_I and H_{II} for $x=0$ and 1 respectively. In a sense, x acts as a parameter which continuously "deforms" $H^{(6)}$ into $H^{(3)}$.

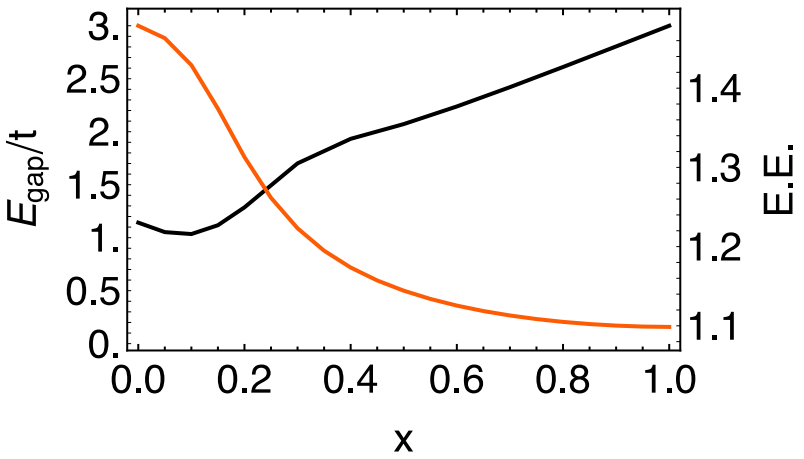

Figure 3.3: Gap (black) and entanglement entropy (red) as a function of deformation parameter x, Eq. (3.9). We consider the case $W_6 = 3.2t$ and $W_3 = t$.

Figure 3.3 shows the dependency of E_{gap} and entanglement entropy with x for $W_6 = 3.2t$ and $W_3 = t$. The crucial result is that there is no gap closing or sharp features in the entanglement entropy (which would be indicatives of a phase transition) as x varies from 0 to 1. In fact, the minimum gap is $E_{gap} \approx t$ for $x = 0.1$ and the difference in the entanglement entropy's value is due to the differences in the ground state occupancies. This shows that both Hamiltonians describe the same $\mathbb{Z}_3$ topological phase for these values of W_6 and W_3.

3.3 Effects of local operators

Although both H_I and H_{II} display a parafermion-hosting $\mathbb{Z}_3$ phase, the ground states themselves are very different. For example, the H_I ground state has a well-defined parity, while the H_{II} ground state does not. Nonetheless, we expect the general behavior of parafermions under changes in local operators to be similar.

Since the DMRG calculations for H_{II} run a few orders of magnitude faster as compared to H_I, in this Section we use H_{II} as a "benchmark"[6]. Unless otherwise stated, we set $W_3=t$ (and $W_6=0$), meaning that, in the absence of other terms in the Hamiltonian, the system will be in the topological phase of H_{II}.

Previous studies [6, 117] have shown that local interactions might be able to destroy the parafermion phase. Specifically, the interaction $-f(e^{i\theta}\psi_j^\dagger\chi_j + e^{-i\theta}\chi_j^\dagger\psi_j)$ destroys the

[6]Here we assume H_{II} and H_I are in the same phase. The calculations using H_{II} would take up to two orders of magnitude more computational time than H_I. Also, there are no analytical results to benchmark H_{II}, on the other hand, H_I can be easily compared with Ref. [6, 117].

parafermion edge while conserving the FPF number. In particular, there is a phase transition at $f = J$ with $\theta = 0$. This interaction translates into the fermionic language (see Appendix C) as

$$e^{i\theta}\psi_i^\dagger\chi_i + e^{-i\theta}\chi_i^\dagger\psi_i = -2\sqrt{3}\sin(\theta)\ n_{\uparrow,i} + [3cos(\theta) - \sqrt{3}\sin(\theta)]n_{\downarrow,i}\ , \tag{3.10}$$

which can be thought of as a mixing of magnetic field and chemical potential for any θ. This shows the importance of local operators to parafermions. In particular, we are interested in the effects of chemical potential,

$$H_d = -\sum_{\substack{j=1 \\ \sigma=\uparrow,\downarrow}}^{L} \mu n_{\sigma,j}, \tag{3.11}$$

and Zeeman fields[7] in all three directions:

$$H_x = \sum_{\substack{j=1 \\ \sigma=\uparrow,\downarrow}}^{L} V_x \tilde{c}_{\sigma,j}^\dagger \tilde{c}_{-\sigma,j}\ , \tag{3.12}$$

$$H_y = \sum_{\substack{j=1 \\ \sigma=\uparrow,\downarrow}}^{L} -iV_y\sigma \tilde{c}_{\sigma,j}^\dagger \tilde{c}_{-\sigma,j}\ , \tag{3.13}$$

$$H_z = \sum_{\substack{j=1 \\ \sigma=\uparrow,\downarrow}}^{L} V_z\sigma n_{\sigma,j}\ , \tag{3.14}$$

which will be added to H_{II}. The Zeeman fields might not be completely realistic but are easy to implement and compare with previous results, both for Majorana bound states and parafermions, thus making an ideal benchmark.

3.3.1 Gap closing

Figure 3.4 shows the dependence of the gap energy E_{gap} with each of these local terms for a 100-site chain. Regarding the chemical potential (μ), we see a near gap closing at $\mu \approx 2.9t$ (Fig. 3.4(a)). This is consistent with previous results [117] which show a transition between topological (parafermionic) and normal phases for $\mu = 3t$. We believe the small discrepancy with our result can be accounted for by finite-size effects. In fact, we can

[7]Strictly speaking, these are not Zeeman fields since they use $\tilde{c}$ operators instead of usual fermionic ones. Nonetheless, as shown in section 3.4, it is possible to use the fermionized parafermion chain in the context of a true fermion operator and thus the local interaction is truly Zeeman fields.

verify that the phase transition point approaches $\mu = 3t$ for increasing the chain sizes (see Section 3.3.3).

The inset of Fig. 3.4(a) shows that the gap between the parafermion states decreases exponentially in the topological phase. This gap arises due to the coupling between parafermionic modes located at both ends of the chain. This exponential decay depends on μ[8], as illustrated by the slower decay with size by $\mu = 2.9t$ as compared to the case $\mu = 2.5t$. As such, this is equivalent to the "exponential protection" predicted for Majorana modes [82] and was also predicted to occur for $\mathbb{Z}_4$ parafermions as well [12].

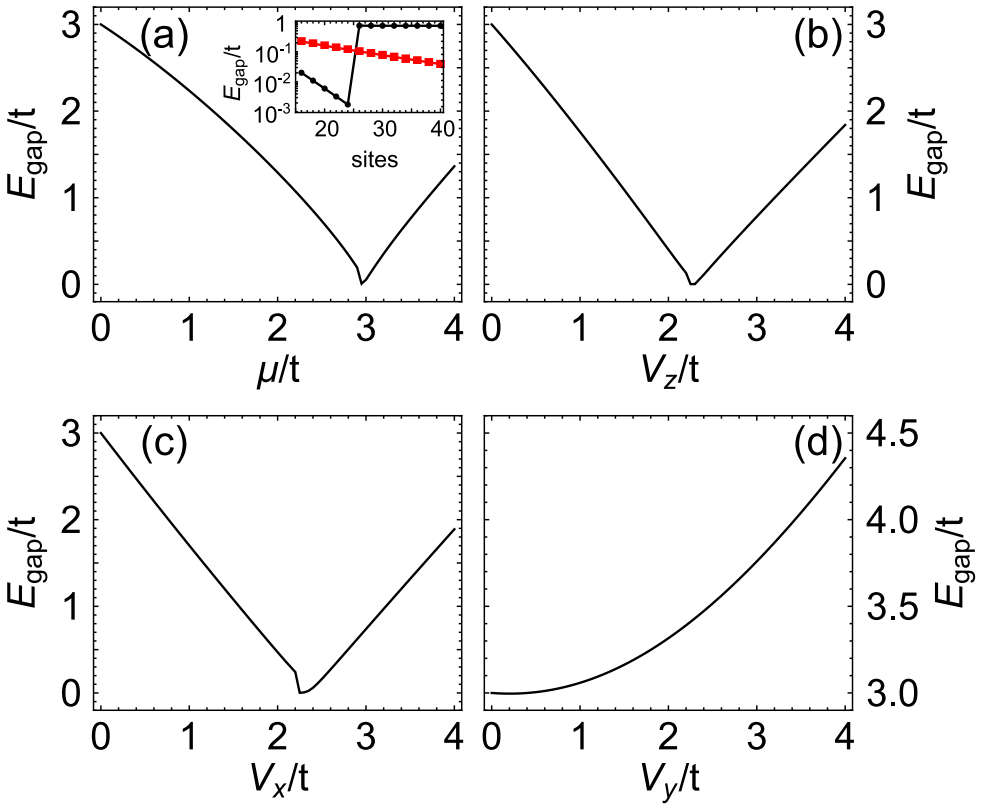

Figure 3.4: Dependence of the gap with respect to local operators. (a) Doping (μ), (b) z-direction (V_z), (c) x-direction (V_x), and (d) y-direction (V_y) Zeeman terms. Panels (a) and (b) show a topological phase transition at $\mu = 3t$ and $V_z = 2.3t$, respectively. Panel (c) has a phase transition between a twofold degenerate state and a normal state for $V_x \approx 2.5J$. Finite-size effects are responsible for the discontinuity in the gap. Panel (d) shows no phase transition as a function of V_y, and the gap always increases. The inset in panel (a) shows the exponential dependence of the gap between the parafermionic modes with the chain length for $\mu = 2.5t$ (black circles) and $\mu = 2.9t$ (red squares).

Parafermionic edge modes are also stable under a small local Zeeman-like term in the z direction proportional to V_z, as given by Eq. (3.14). As shown in Fig. 3.4(b), the topological phase is destroyed only for relatively large values of the Zeeman term ($V_z \gtrsim 2.3t$). In addition, similarly to the dependency with the doping μ, the transition value is sensitive

[8]The exponential decay happens as long as μ is such that does not break the $\mathbb{Z}_3$ phase.

to finite-size effects even for long chains. In both cases (μ and V_z), the ground state goes from a threefold degenerate to a nondegenerate one at the transition.

As discussed in detail in Appendix C, a generic magnetic field in the xy plane dos *not* conserve the Fock-parafermion number, thus breaking the $\mathbb{Z}_3$ symmetry. In fact, any small positive Zeeman term in the x-direction ($V_x > 0$) breaks the ground state $\mathbb{Z}_3$ symmetry, changing the ground state degeneracy from $n_{\text{gs}} = 3$ to 2. Locally, the Zeeman at the x-direction brakes the threefold degenerate state into a state with Fock-parafermion number 0 and other with a superposition of Fock-parafermion numbers 1 and 2. As V_x increases, a second phase transition occurs, further reducing n_{gs} from 2 to 1 . This is shown in Fig. 3.4(c), where the phase transition to the $n_{\text{gs}} = 1$ (nondegenerate) ground state occurs around $V_x \approx 2.5t$. In this case, finite-size effects are more prominent than the previous cases, making it difficult to pinpoint the exact V_x value where phase transition occurs for large systems.

By contrast, any positive Zeeman term in the y direction ($V_y > 0$) produces a phase transition directly from from $n_{\text{gs}} = 3$ to 1. The gap increases monotonically with V_y, as shown in Fig. 3.4(d). Due to these differences between x and y directions, we expect a strong dependence of the gap with the direction of magnetic fields in the xy plane.

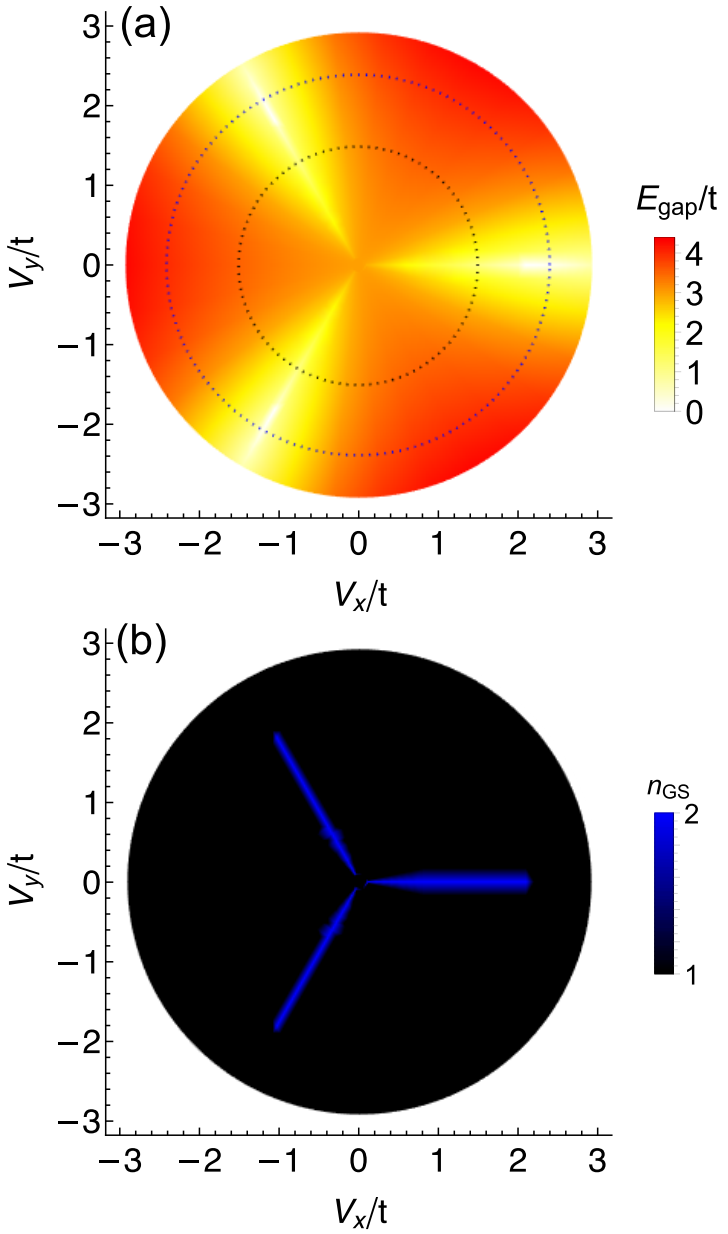

Figure 3.5: Dependence of (a) the gap to the intensity and angle of the magnetic field and (b) its ground state degeneracy, $n_g s$. For fixed $V_{xy} < 2.5t$ the gap is minimum at angles $0, \pm 2\pi/3$ and the ground state is twofold degenerate. The dotted circles in panel (a) correspond to the transversal cut shown in Fig. 3.6.

In order to better understand how the local Zeeman terms in the xy plane affect the parafermionic chain ground state, we consider a generic Zeeman term arising from a magnetic field in the xy plane, given by

$$H_{xy} = V_{xy} \sum_{j=1}^{L} e^{-i\theta} \tilde{c}^{\dagger}_{\uparrow,j} \tilde{c}_{\downarrow,j} + e^{i\theta} \tilde{c}^{\dagger}_{\downarrow,j} \tilde{c}_{\uparrow,j}, \tag{3.15}$$

where $V_{xy} = \sqrt{V_x^2 + V_y^2}$ is the strength of the Zeeman field and θ is the magnetic field angle

with respect to the x direction.

We calculate the gap energy ($E_{\rm gap}$) and ground state degeneracy ($n_{\rm gs}$) as a function of V_{xy} and θ. The results are depicted in Fig 3.5. Notice the clear symmetry in $E_{\rm gap}(\theta)$ and $n_{\rm gs}(\theta)$ as $\theta \to \theta + 2\pi/3$. This is in fact due to the invariance of H_{xy} under a $2\pi/3$ rotation, associated with the $\mathbb{Z}_3$ symmetry of the full Hamiltonian. This invariance becomes clear by writing Eq. (3.15) in terms of parafermion operators, which can be accomplished by inverting the fermionization process discussed in Appendix C. The result is

$$H_{xy} = \frac{V_{xy}}{3}\sum_{j=1}^{L} \omega^{\sum_{p<j} N_p} e^{-i\theta}\left[\chi_j + \omega\psi_j + \chi_j^\dagger\psi_j^\dagger\right] + \omega^{2\sum_{p<j} N_p} e^{i\theta}\left[\chi_j^\dagger + \omega^2\psi_j^\dagger + \omega^2\chi_j\psi_j\right]. \tag{3.16}$$

For $\theta = 0$ and $\pm 2\pi/3$, the Hamiltonian is invariant under a transformation $\chi \to e^{i\theta}\chi$ and $\psi \to e^{i\theta}\psi$. This can be easily seen in Fig. 3.5, where the smallest gaps occur at angles $\theta_n^{\rm min} = 2n\pi/3$, $n = 1, 2, 3$. In those cases, the ground state is doubly degenerate, as discussed above, with a phase transition occurring at $V_{xy} \approx 2.5t$, similar to that shown in Fig. 3.4(c).

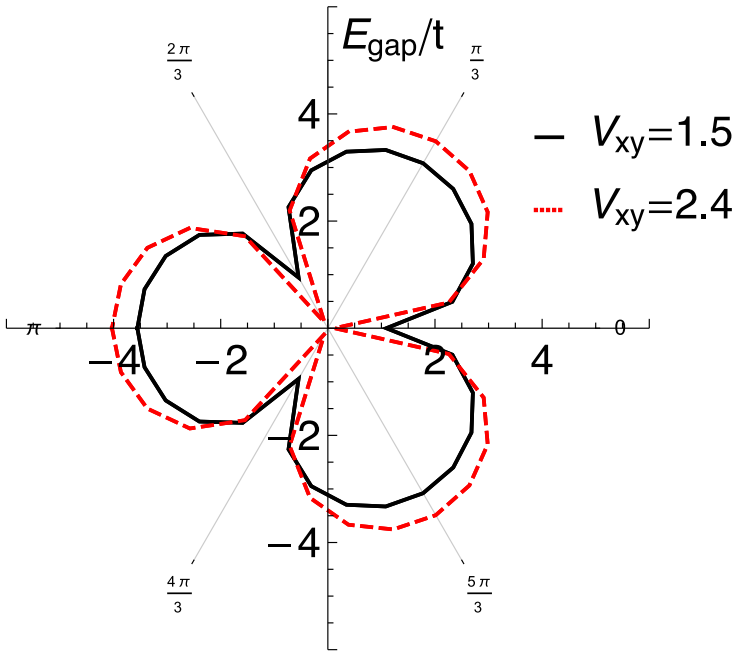

Figure 3.6: Transversal cut of Fig. 3.5 with $V_{xy} = 1.5t$, solid black, and $V_{xy} = 2.4t$, dashed red.

In order to better visualize this, a crosscut of Fig. 3.5 with $V_{xy} = 1.5t$ and $2.4t$ is shown in Fig. 3.6. The minimum gap occurs at $\theta_n^{\rm min} = 2n\pi/3$ and the maxima are at $\theta_n^{\rm max} = (2n-1)\pi/3$ with $n = 1, 2, 3$.

3.3.2 Local disorder

We also considered the case of a locally disordered potential, i.e., the on-site terms μ or V_z are randomly distributed. We simulated 20 different profiles of chemical potential or Zeeman in the z direction; both μ_j and $V_{z,j}$ were generated from a uniform distribution and varying the mean values of μ/t or V_z/t.

Figure 3.7 shows the variation of the mean disorder-induced splitting $\langle \Delta E_0 \rangle$ between the ground states as a function of the mean values of μ or V_z. The splitting is zero (i.e., the parafermionic phase is *not* destroyed) provided that the mean values are much smaller than the critical values for which the system undergoes a phase transition, shown in Fig. 3.4. By contrast, for disordered chains with mean values of $\langle \mu \rangle / t$ or $\langle V_z \rangle / t$ close to critical values, even a handful of sites are enough to open a gap and lift the ground state degeneracy.

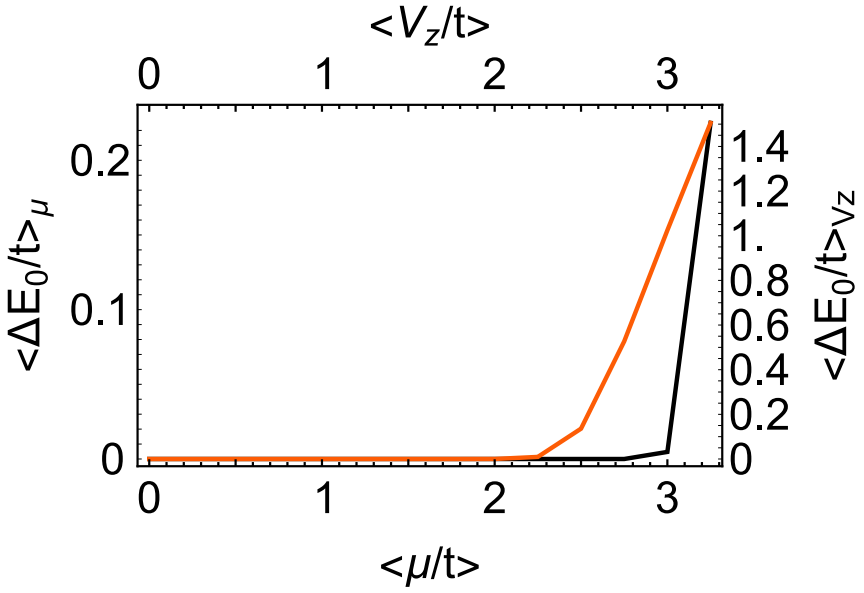

Figure 3.7: Mean energy splitting between the ground states due to random potential with maximum intensity for the chemical potential μ (black) and Zeeman field at z direction V_z (red). The mean was calculated based on 20 different distributions of impurities. Note the splitting happens for values of $\langle \mu \rangle / t$ or $\langle V_z \rangle / t$ of the order of the critical value seen in Fig. 3.4.

Nonetheless, a single impurity symmetry in the bulk do not lift the threefold degeneracy as long as it preserve the $\mathbb{Z}_3$ symmetry. This property holds even when the impurity potential is large, $\langle \mu \rangle \sim 100t$ and $\langle V_z \rangle \sim 100t$. This result is central to the topological protection since it shows that even though the Hamiltonian has a long-range interaction the edge state "doesn't feel" the bulk. On the other hand, a single impurity that breaks $\mathbb{Z}_3$ symmetry, no matter how weak, is enough to lift the threefold degeneracy.

This can be easily understood in terms of simple first-order approximation, similar to what was done in Appendix B. Locally, *all* ground states are a superposition of vac-

uum and single-occupied states ($|E\rangle, \tilde{c}^\dagger_\uparrow |E\rangle, \tilde{c}^\dagger_\downarrow |E\rangle$). Therefore, a single-site impurity that preserves $\mathbb{Z}_3$ symmetry will generate a diagonal matrix with the same elements for the first-order approximation. However, in the case of a Zeeman field in the xy-plane, thus one that breaks the $\mathbb{Z}_3$ symmetry, will have a diagonal term plus two off-diagonals.

3.3.3 Fock-parafermion spectral function

We now turn to the spatial distribution of the parafermionic modes along the chain. To this end, we calculate the zero-energy Fock parafermion spectral function at site j defined as

$$\mathcal{A}_j(0) = \frac{2\pi}{n_{\rm gs}} \sum_{|g'\rangle|g\rangle} |\langle g'| d_j \bar{\omega}^{N_j} |g\rangle|^2 + |\langle g'| \bar{\omega}^{N_j} d_j^\dagger |g\rangle|^2, \tag{3.17}$$

where d is the Fock-parafermion operator defined in Eq. (C.4) in Appendix C, $N_j = n_{\uparrow,j} + 2n_{\downarrow,j}$ is the Fock-parafermion number operator and the second sum (normalized by the ground states degeneracy $n_{\rm gs}$) runs over all ground state $|g\rangle, |g'\rangle$. As discussed in Appendix C, the phase factor $\bar{\omega}^{N_j}$ prevents spurious asymmetries in the FPF spectral weights along the chain [88]. Interestingly, the phase factor $\bar{\omega}^{N_j}$ does not affect the FPF spectral function of H_I, Fig. 3.8(a). This implies that the structure of the ground states of H_I is significantly different from that of the ground states of H_{II}, as discussed below.

For a parafermion chain with no local interactions (Eq. (3.6)), the zero-energy FPF spectral function is $\mathcal{A}_j(0)/(2\pi) = 2/9(\delta_{j,1} + \delta_{j,L})$, which is perfectly consistent with our simulations. In the Appendix C, we show the derivation of $\mathcal{A}_j(0)$ for a $\mathbb{Z}_M$ parafermion chain.

We emphasize that $\mathcal{A}_j(0)$ measures the local density of states related to Fock parafermions instead of the electrons, although the actual calculations involve fermionic matrix elements. A more naïve approach would be to calculate the purely fermionic spectral function, as it has been done in the $\mathbb{Z}_4$ case, see Chapter 2 [12, 17]. However, the matrix elements entering the usual fermionic spectral function couple states with opposite fermionic parities and produce ill-defined results for both H_I and H_{II}. On one hand, all ground states of H_I, have the same parity, such that $\langle g'| c_\sigma |g\rangle = 0$, all ground states of H_{II} don't have well-defined parity. In addition, the terms arising from bulk states do not necessarily cancel each other, which is a necessary property here (see Appendix C)[9]. For these reasons, $\mathcal{A}_j(0)$ as defined above is a better option to visualize the edge parafermionic modes.

The FPF spectral function for H_I (Fig. 3.8(a)) shows exponentially localized edge states in the topological phase ($W_6 \gtrsim 2t$). These modes decay exponentially into the interior of the chain but in a nonmonotonic fashion, with an oscillation period of a few

[9]To observe parafermions edge states, we need FPF spectral function. Otherwise, we don't clearly see localized states. In the case of Majorana bound states, $\mathbb{Z}_2$, the FPF spectral function *is* the fermionic spectral function.

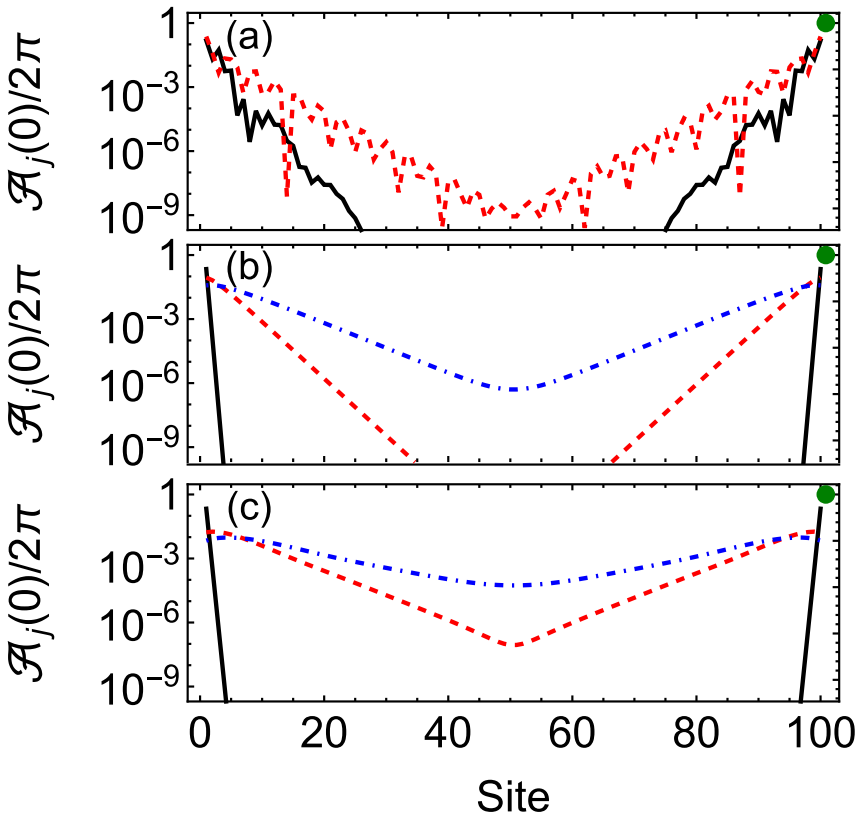

Figure 3.8: FPF spectral function $\mathcal{A}_j(0)$ for different interactions. (a) Spatial spread of the ground state over the chain for H_I with $W_6 = 2.2t$ (solid black) and $W_6 = 3.2t$ (dashed red). (b-c) Spatial spread of the ground state of H_{II} for $W_3 = t$ and (b) $\mu = 0.1t$ (solid black), $\mu = 2.5t$ (dashed red), and $\mu = 2.8t$ (dot-dashed blue) and (c) for $V_z = 0.1t$ (solid black), $V_z = 2.1t$ (dashed red), and $V_z = 2.2t$ (dot-dashed blue). The green dots mark the analytical value (2/9) for perfectly localized $\mathbb{Z}_3$ edge parafermions of $H_{\rm pf}$.

sites.

This is in sharp contrast with the strongly localized edge states of H_{II} for $W_3 = t$ shown in Figs. 3.8(b-c). For small values of on-site potentials (μ and V_z, black curves), the decay occurs within a few (~ 10) sites. For $\mu = V_z = 0$ and $W_3 = t$, H_{II} maps exactly into $H_{\rm pf}$ and the parafermionic modes become free, with the FPF spectral function being zero in all sites of the chain except at the end sites, where it reaches the analytically obtained value of 2/9 (green dots in Fig. 3.8).

These differences between H_I and H_{II} are also encoded in the structure of the ground states in the FPF basis. For instance, while two ground states ($|g\rangle$ and $|g'\rangle$) of H_{II} with distinct $\mathbb{Z}_3$ parity values can be coupled by any local FPF creation/destruction operator such that $\langle g|d_j + d_j^\dagger|g'\rangle \neq 0$, the same is *not* true for the ground states of H_I. Although the latter have well-defined $\mathbb{Z}_3$ parity values, they are not eigenstates of all local FPF number operators $n_{d,j} = d_j^\dagger d_j$.

Figure 3.8(b) shows the spreading of the parafermionic state as we increase the doping across the phase transition at $\mu \approx 2.9$. The plot of $\mathcal{A}_j(0)$ shows exponentially localized

modes in the topological phase ($\mu = 0.5t$ (black) and $\mu = 2.5t$ (dashed red)), while the ground state becomes delocalized near the transition point ($\mu = 2.8t$ (dashed blue)). Moreover, it becomes clear that finite-size effects can be considerable in small chains ($<$ 100-site long chains).

The same analysis can be done in the case of a magnetic field in the z direction (Fig. 3.8(b)) for $\mu = 0.1t$. Again, the spectral function shows exponentially localized edge modes for $V_z < V_z^c = 2.2t$, i.e., before the phase transition at $V_z^c = 2.2t$ (dashed blue curve), at which point the ground state spectral function is spread all over the chain.).

3.3.4 Entanglement entropy

Lastly, we consider the signatures of the topological phase transition in the E.E. [117, 124]. Figure 3.9 shows the E.E. calculated at the central link of the chain as a function of the chemical potential μ for different chain sizes.

For small values of μ such that the system is in the topological phase, E.E. is constant and pinned at ln(3) (main panel of Fig. 3.9). This is consistent with previous DMRG results for $\mathbb{Z}_3$ parafermion chains [117]. As μ increases and the system approaches the topological phase transition, the E.E. increases, reaches a maximum near the phase transition, and then decreases. This behavior is accentuated for larger chains, as shown in Fig. 3.9.

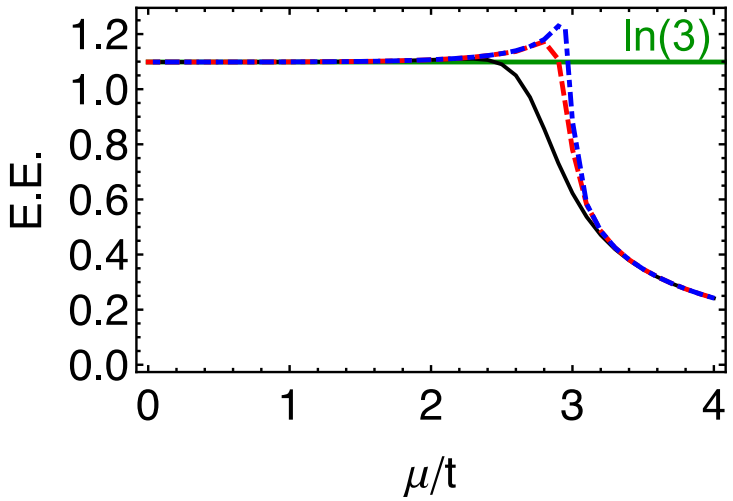

Figure 3.9: Entanglement entropy (E.E.) dependence with doping for different chain lengths of 16 (solid black), 48 (dashed red) and 100 (dotted blue). Note that far away from the phase transition all of them have the same value.

3.4 Allowing double occupancy

In the previous sections, we considered a local fermionic basis excluding the double occupancy state, $c_\downarrow^\dagger c_\uparrow^\dagger |E\rangle$. A consistency check for this approach would be to include this state in the fermionic basis along with a Hubbard interaction in each site, $U_H n_\uparrow n_\downarrow$, and then take the limit $U_H \to \infty$. In this section, we perform this consistency check and show that indeed we recover the main text's results.

To perform the calculations in this section, we use ITensor [113] but instead of "tJ" site we use "electron" site. This in turn allows of double occupancy. Again, we use H_{II} to illustrate that single occupancy is not necessary. Figure 3.10 shows the persistence of the parafermionic phase already for relatively small values of U_H relative to the hopping t (say, $U_H/t \sim 1-5$). For $U_H \gg t$, the gap becomes completely independent of the chain size, and we recover the expected $E_{\text{gap}}/t = 3$. This shows that a large Hubbard (on-site) interaction is not necessary for the formation of $\mathbb{Z}_3$ parafermions and that finite-size effects are not relevant in this regime.

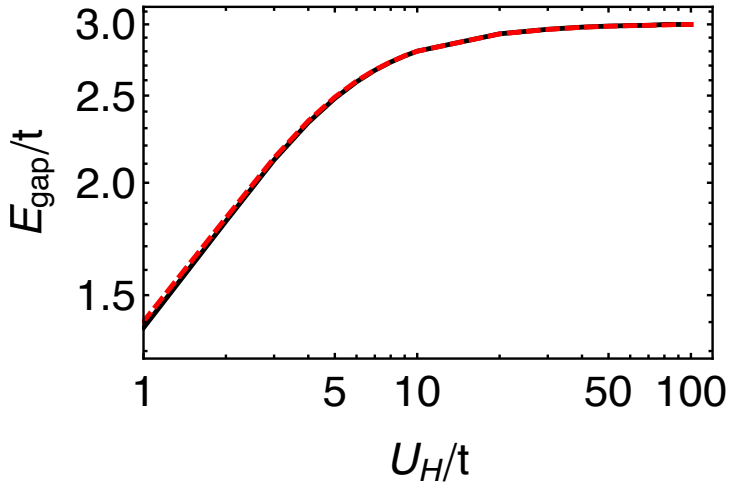

Figure 3.10: Gap dependency with Hubbard interaction in a double occupancy basis. The gaps of the 16-site chain (red dashed) and 100-site chain (solid black) have minor differences only in the low interaction regime, $U_H \approx t$.

Chapter 4

Overlap of parafermion bound states in Fractional Quantum Hall

In the last chapters, we studied fermionic models mapped to pure parafermionic chains. However, as stated before, the nature of those models is not necessarily the same. This is the case for the $\mathbb{Z}_4$ fermionic parafermion, which does not have the same braiding statistics as "pure" $\mathbb{Z}_4$ parafermion [12, 13]. In this chapter, we study a different model in which an FQH edge with different gaps hosts parafermion bound states at the interface. Here, we will use a semiclassical approximation to treat the model's low-energy excitations. Differently from before, these are bona fide parafermion bound states, with the expected braiding [36].

Being one-dimensional and subject to interactions, systems hosting parafermions are usually modeled using bosonization methods [106]. Parafermionic bound states emerge at the interfaces between regions where FQH states are coupled by backscattering and superconducting pairing, thus generating non-trivial band gaps. Both effects give rise to cosine terms in the bosonization language, so parafermion systems can be modeled as inhomogeneous sine-Gordon Hamiltonians, as shown in the introduction. While a homogeneous sine-Gordon model is among the rare examples of an exactly solvable interacting model, no such exact solution is known for the inhomogeneous model. Therefore, the theoretical modeling typically rests on approximations.

One such method is the instanton gas approximation, which is based on a semiclassical treatment of the sine-Gordon Hamiltonian [125–128]. Single instantons, time-like kinks of the phase field, are the solutions of the corresponding classical Euler-Lagrange equation and can be used to compute the ground state energy [129, 130]. Multiple instantons can easily be accounted for in the dilute one-instanton gas approximation, where different instantons are assumed to be far apart such that their interaction can be neglected. This method can be extended towards multiple interacting instantons, also called molecular instantons [131–133]. Used in the context of resurgence theory [134, 135], multi-instantons can offer a path to go beyond the first-order approximation. As we will show, such inter-

acting multi-instanton configurations can become important for PBSs located at a finite distance from each other. This chapter is adapted from *"Overlap of parafermionic zero modes at a finite distance"*, Phys. Rev. Res. 4, 043094 (2022).

4.1 Model

The model system for studying parafermion bound states consists of a pair of FQH edges containing two counter-propagating modes. To generate parafermion bound states, it is necessary to engineer two topologically distinct spectral gaps in different regions such that a subgap parafermion bound state appears at the interfaces between these gapped regions [101, 102]. Many proposals consider an interface between ferromagnetic (FM) and superconducting (SC) regions [9, 36, 128]. Denoting by $\psi_{L,R}(x)$ the annihilation operators for left- and right-moving electrons in the FQH state, the ferromagnet induces a backscattering gap corresponding to a term $\Delta_{\mathrm{FM}}\psi_L^\dagger\psi_R + \mathrm{H.c.}$. On the other hand, the proximity effect from a nearby superconductor creates and annihilates Cooper pairs and gives rise to a term $\Delta_{\mathrm{SC}}\psi_L^\dagger\psi_R^\dagger + \mathrm{H.c.}$. Hence, a pair of FQH edge states with such an FM-SC-FM junction, see Fig. 4.1, should host parafermion bound states at the interfaces.

We consider a FQH state with filling factor $1/n$[1] and group velocity v. We first bosonize the left- and right-moving electrons in terms of chiral bosonic fields $\varphi_{L,R}(x)$ such that

$$\psi_{L,R}^\dagger(x) = \frac{1}{\sqrt{2\pi n\xi}} e^{-in\varphi_{L,R}(x)}, \tag{4.1}$$

where ξ is the correlation length, which is the inverse of the high-energy cutoff, $\xi = v/E_{\mathrm{cutoff}}$ (using $= 1$) and n comes from the $1/n$ filling factor.

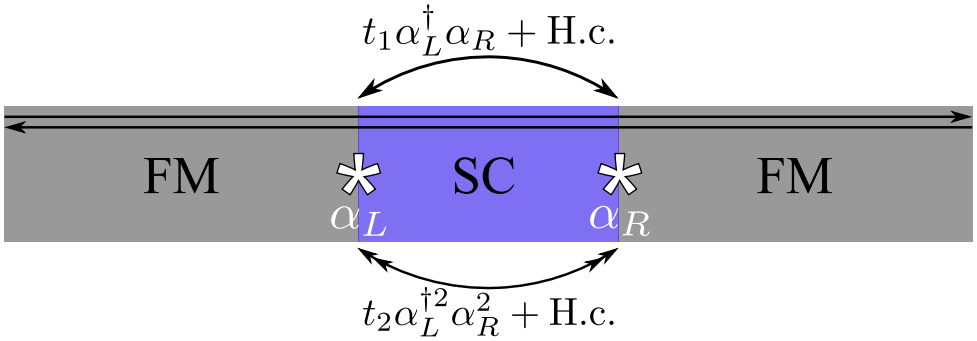

Figure 4.1: The system comprises a pair of FQH edges with two counter-propagating edge modes at filling factor $1/n$. The FQH edge is subject to induced superconductivity and ferromagnetic coupling leading to an FM-SC-FM junction. The parafermion zero modes appear at the interfaces between FM and SC regions, which is illustrated by the asterisks.

[1] Although this part is valid for Laughlin states with odd n, there is no mathematical constraints for even n (in the equations shown below). We use this fact to later calculate Monte Carlo for $n = 2$, even though the ground state is bosonic [136] all equations are the same.

We continue by defining the fields $\phi = (\varphi_R + \varphi_L)/2$ and $\theta = (\varphi_R - \varphi_L)/2$, which satisfy the commutation relations $[\phi(x), \theta(x')] = (i\pi/n)\Theta(x - x')$, where Θ is the Heaviside function. Hence, $\phi(x)$ and $(n/\pi)\partial_x\theta(x)$ are canonically conjugate variables. The backscattering and pairing terms can then be simplified to $\Delta_{\rm SC}[\sin(2n\phi)+1]$ and $\Delta_{\rm FM}[\sin(2n\theta)+1]$, respectively.

The Euclidean action for the whole system thus becomes an inhomogeneous sine-Gordon model

$$S_{\rm sys} = \int d\tau dx \Big\{ \frac{nv}{2\pi}\left[(\partial_x\theta)^2 + (\partial_x\phi)^2\right] + \frac{in}{\pi}(\partial_x\theta)(\partial_\tau\phi) - \frac{\mu}{\pi}\partial_x\theta + \frac{\Delta_{\rm FM}(x)}{\pi n\xi}\sin(2n\theta) + \frac{\Delta_{\rm SC}(x)}{\pi n\xi}\sin(2n\phi)\Big\}, \tag{4.2}$$

where $\Delta_{\rm FM}(x)$ and $\Delta_{\rm SC}(x)$ vanish, respectively, outside the FM and SC regions and are constant inside those regions[2]. We assume the chemical potential μ to be constant along the system. We focus on the limit $\Delta_{\rm FM}L_{\rm FM}/v \to \infty$, where $L_{\rm FM}$ is the length of the FM region. In this limit, the field $\theta(x)$ is pinned to a minimum of $\sin(2n\theta)$ inside the FM region, while the field ϕ is allowed to fluctuate.

4.1.1 Effective action

By completing the square and considering $\theta(x)$ as constant inside the FM region, the effective action of the system becomes that of a simple sine-Gordon model with a Berry-phase term due to the chemical potential. In order to obtain the effective action with only ϕ-field dependency, we first need to remove the cross-term $\partial_x\theta\partial_\tau\phi$, we consider the identity

$$\frac{nv}{2\pi}(\partial_x\theta)^2 + \frac{in}{\pi}(\partial_x\theta)(\partial_\tau\phi) - \frac{\mu}{\pi}\partial_x\theta = \frac{nv}{2\pi}\left(\partial_x\theta + \frac{i}{v}\partial_\tau\phi - \frac{1}{nv}\mu\right)^2 + \frac{n}{2\pi\nu}(\partial_\tau\phi)^2 + \frac{i\mu}{\pi v}\partial_\tau\phi - \frac{\mu^2}{2\pi nv}, \tag{4.3}$$

where the last term is a constant and can be disregarded in the upcoming calculation of the action. In the SC region, $\Delta_{\rm FM} = 0$, $\Delta \equiv \Delta_{\rm SC}$ and action can be separated in two effective terms, $S_{sys}[\phi,\theta] = S_{\rm eff}[\phi] + S_{\rm eff}[\phi,\theta]$, which reads

$$S_{\rm eff}[\phi] = \int d\tau \int_{\rm SC} dx \Big\{ \frac{n}{2\pi v}(\partial_\tau\phi)^2 + \frac{nv}{2\pi}(\partial_x\phi)^2 + \frac{\Delta}{\pi n\xi}\sin(2n\phi) + \frac{i\mu}{\pi v}\partial_\tau\phi \Big\}, \tag{4.4}$$

$$S_{\rm eff}[\phi,\theta] = \frac{nv}{2\pi}\int d\tau \int_{\rm SC} dx \left(\partial_x\theta + \frac{i}{v}\partial_\tau\phi - \frac{n}{v}\mu\right)^2 \tag{4.5}$$

[2]The cross term, $\partial_x\theta\partial_\tau\phi$ comes from the Legendre transformation of the Hamiltonian described in the introduction, $S[\phi,\theta] = \int d\tau \left\{\int dx\,[\Pi_\phi i\partial_\tau\phi + H[\phi,\theta]] - \mu N\right\}$, where $\Pi_\phi = (n/\pi)\partial_x\theta$ is the canonical conjugate variable of ϕ and the charge density is $\rho = (1/\pi)\partial_x\theta$, thus the total number $N = (1/\pi)\int dx(1/\pi)\partial_x\theta$.

We still need to show the $S[\phi,\theta]$ can be made independent of ϕ, such that we can integrate it over θ. In order to do that, we need to make a shift in the θ field. We Fourier transform the fields and chemical potential from (x,τ) to (k,ω),

$$\begin{aligned}\theta(x,\tau) &= \frac{1}{TL}\sum_{k,i\omega}\theta(k,i\omega)e^{i(kx-\omega\tau)},\\ \phi(x,\tau) &= \frac{1}{TL}\sum_{k,i\omega}\phi(k,i\omega)e^{i(kx-\omega\tau)},\\ \mu(x) &= \frac{1}{L}\sum_{k,i\omega}\delta_{i\omega,0}\mu(k,i\omega)e^{i(kx-\omega\tau)}.\end{aligned} \tag{4.6}$$

The mixing field action becomes

$$S_{\text{eff}}[\phi,\theta] = \frac{nv}{2\pi(TL)^2}\int d\tau\int_{\text{SC}}dx\left\{\sum_{k,\omega}\left[ik\theta(k,\omega)+\frac{\omega}{v}\phi(k,\omega)-\frac{T\delta_{\omega,0}n}{v}\mu(k,\omega)\right]e^{i(kx-\omega\tau)}\right\}^2. \tag{4.7}$$

Now, we can define a new variable $\tilde{\theta}$

$$\tilde{\theta}(k,i\omega) \equiv \theta(k,\omega) - \frac{i\omega}{kv}\phi(k,\omega) + \frac{iT\delta_{\omega,0}n}{kv}\mu(k,\omega), \tag{4.8}$$

such that after an inverse Fourier transformation, the action becomes

$$S_{\text{eff}}[\tilde{\theta}] = \frac{nv}{2\pi}\int d\tau\int_{\text{SC}}dx\left[\partial_x\tilde{\theta}\right]^2. \tag{4.9}$$

The measure in the partition function is written in terms of the Fourier transformation of the field as

$$\int\mathcal{D}[\phi] = \prod_{k,i\omega}\int d\phi(k,i\omega), \qquad \int\mathcal{D}[\theta] = \prod_{k,i\omega}\int d\theta(k,i\omega) = \prod_{k,i\omega}\int d\tilde{\theta}(k,i\omega), \tag{4.10}$$

where we integrate over all possible field configurations $\theta(k,i\omega)$ for a given pair $(k,i\omega)$. We can rename $\theta\to\tilde{\theta}$ in the measure integral, similar to a shift $x\to x+a$ in the usual Riemann integral $\int_{-\infty}^{\infty}dxf(x)$. With these considerations, we can calculate the partition function in the 2D euclidean space while keeping the real space Feynman measure (and dropping the tilde),

$$\begin{aligned}\mathcal{Z} &= \int\mathcal{D}[\phi]\int\mathcal{D}[\theta]e^{-S_{\text{sys}}[\theta,\phi]}\\ &= \int\mathcal{D}[\phi]e^{-S_{\text{eff}}[\phi]}\int\mathcal{D}[\theta]e^{-S_{\text{eff}}[\theta]}\\ &= \mathcal{C}\int\mathcal{D}[\phi]e^{-S_{\text{eff}}[\phi]},\end{aligned} \tag{4.11}$$

where we integrated out the field θ as a constant given by

$$\mathcal{C} = e^{\int dx \int d\tau \frac{\mu(x)^2}{2\pi n v}} \int \mathcal{D}[\theta] e^{-\frac{nv}{2\pi} \int dx \int d\tau [\partial_x \theta]^2}. \tag{4.12}$$

The integral in θ can be done by using the Gaussian integral [130]. Since we are interested in the ground state splitting of parafermions, we will now focus only on the action $S_{\text{eff}}[\phi] \equiv S[\phi]$ that contains all the relevant information.

4.1.2 Effective parafermion Hamiltonian

At low energies, the predictions resulting from the sine-Gordon model can be translated into an effective parafermion Hamiltonian, which is valid at energies below the band gaps $|E| \ll \Delta, \Delta_{\text{FM}}$. To describe the effective parafermion interaction, we consider two parafermion modes described by $\mathbb{Z}_{2n}$ parafermion operators $\alpha_{L,R}$[3]. These operators satisfy the parafermionic commutation relations $\alpha_{L,R}^{2n} = 1$, $\alpha_{L,R}^{\dagger} = \alpha_{L,R}^{2n-1}$ and $\alpha_L \alpha_R = e^{i\pi/n} \alpha_R \alpha_L$. A generic interaction Hamiltonian that preserves the $\mathbb{Z}_{2n}$ charge can be written as

$$H_{\mathbb{Z}_{2n}} = \sum_{k=1}^{n} H_k, \quad H_k = |t_k| e^{i\lambda_k} \alpha_L^{\dagger k} \alpha_R^k + \text{H.c.}. \tag{4.13}$$

The phase diagrams of such parafermion Hamiltonian have been studied using different methods [6, 88, 137, 138]. This Hamiltonian can be written in the eigenstate basis of the first-order interaction term $\alpha_L^{\dagger} \alpha_R |q\rangle = -e^{i\pi(\hat{q}-1/2)/n} |q\rangle$, where the eigenstates $|q\rangle$ are labeled by an integer $q \in \{0, 1, 2, ..., 2n-1\}$ which corresponds to the total charge of the superconducting region [128]. As a consequence, powers of the first-order interaction term satisfy

$$\begin{aligned} \alpha_L^{\dagger k} \alpha_R^k &= \alpha_L^{\dagger k-1} \alpha_L^{\dagger} \alpha_R \alpha_R^{k-1} = \bar{\omega}_p^{k-1} \alpha_L^{\dagger k-1} \alpha_R^{k-1} (\alpha_L^{\dagger} \alpha_R) \\ &= \bar{\omega}_p^{\sum_{j=1}^{k-1}(k-j)} (\alpha_L^{\dagger} \alpha_R)^k \\ &= \bar{\omega}_p^{k(k-1)/2} (\alpha_L^{\dagger} \alpha_R)^k. \end{aligned} \tag{4.14}$$

It is easy to see that $\alpha_L^{\dagger k} \alpha_R^k$ is diagonal in the basis $\{|q\rangle\}$ and

$$\begin{aligned} \alpha_L^{\dagger k} \alpha_R^k |q\rangle &= \bar{\omega}_p^{k(k-1)/2} (\alpha_L^{\dagger} \alpha_R)^k |q\rangle = (-1)^k \bar{\omega}_p^{k(k-1)/2} \omega_p^{k(q-1/2)} |q\rangle \\ &= (-1)^k \omega_p^{k(q-k/2)} |q\rangle \\ &= (-1)^k e^{\frac{i\pi k}{n}(q-k/2)} |q\rangle . \end{aligned} \tag{4.15}$$

[3] In this chapter we use a different notation for parafermions to avoid any misunderstanding regarding the wave function $\psi_{L,R}$.

such that the energy eigenvalues $E(q)$ of the Hamiltonian $H_{\mathbb{Z}_{2n}}$ can be expressed as a sum,

$$E(q) = \sum_{k=1}^{n} 2(-1)^k |t_k| \cos\left(\frac{\pi k}{n}(q - k/2) + \lambda_k\right). \tag{4.16}$$

In the following, we will use a semiclassical instanton calculation as well as a Monte-Carlo simulation to determine the effective coupling strengths $t_{1,2}$ and the phases $\lambda_{1,2}$.

4.2 Instanton calculation

4.2.1 Review of the dilute one-instanton gas

In this subsection, we briefly review the dilute one-instanton gas approximation [125–128] to find the energy splitting between different ground states. In order to obtain the energies, it is necessary to compute the transition rates between different configurations of the θ field. In imaginary time, such transition amplitudes correspond to the matrix elements,

$$\langle j_+ | \, e^{-HT} \, | j_- \rangle \tag{4.17}$$

between two stationary states $|j_\pm\rangle$, in which the field θ is pinned at a minimum of the sine potential and which are eigenstates in the limit $\Delta L/v \gg 1$. Moreover $T \gg \xi/v$ is a large time. This transition amplitude can be conveniently calculated with the action $S[\phi]$.

We focus on classical solutions of the action $S[\phi]$ with constant spatial profile, $\partial_x \phi = 0$ [128] because solutions with a nonzero $\partial_x \phi$ have a larger action and only contribute subleading corrections to the transition amplitude for a given number of instantons. Using this simplification, the equation of motion corresponding to the action (4.4) becomes

$$\frac{n}{\pi v}\partial_\tau^2 \phi(\tau) = \frac{2\Delta}{\pi \xi} \cos[2n\phi(\tau)], \tag{4.18}$$

and allows us to define the states $|j\rangle$ which correspond to the stationary solutions $\phi_j = -\pi/4n + j\pi/n$ ($j \in \{0, 1, .., 2n-1\}$) which minimize the classical action. Solitons correspond to the non-stationary classical solutions and can be found by straightforward

integration of Eq.(4.18).

$$\begin{aligned}
\partial_\tau^2\tilde{\phi}(\tau) &= \omega^2\sin(\tilde{\phi}) \\
\int d\tilde{\phi}\partial_\tau^2\tilde{\phi}(\tau) &= \omega^2\int d\tilde{\phi}\sin(\tilde{\phi}) \\
\frac{1}{2}(\partial_\tau\tilde{\phi}(\tau))^2 &= -\omega^2\cos(\tilde{\phi}(\tau)) + \text{cte.} \\
\int d\phi\frac{1}{\sqrt{\sin(\tilde{\phi})}} &= \pm 2\omega\int d\tau \\
2\ln\left[\tan\left(\tilde{\phi}/2\right)\right] &= \pm 2\omega(\tau-\tau_0).
\end{aligned} \tag{4.19}$$

Where we used the fact that at $\tau\to-\infty$ the field $\phi(\tau) = -\pi/4n + \pi j/n$ and $\phi'(\tau) = 0$ with $\omega = 2\sqrt{\Delta v/\xi}$. The solution takes the form of a classical field that interpolates between two stationary solutions, $|j\rangle$ and $|j+\epsilon\rangle$, with $\epsilon\pm1$ corresponding to an instanton (+) or anti-instanton (-), and centered at an imaginary time τ_0,

$$\phi_{\rm cl}^{\epsilon}(\tau) = -\frac{\pi}{4n} + \frac{\pi j}{n} + \frac{2\epsilon}{n}\arctan\left[e^{\omega(\tau-\tau_0)}\right]. \tag{4.20}$$

The action of the soliton field has two different contributions, a kinetic term (S_0) and a Berry-phase term (S_{Bp}). While the former is responsible for the system's overall energy scale, the latter will induce an oscillatory behavior in the energy-splitting,

$$S[\phi_{\rm cl}^{\epsilon}] = \underbrace{\frac{Ln}{\pi v}\int_0^T d\tau[\partial_\tau\phi_{\rm cl}^{\epsilon}(\tau)]^2}_{S_0} + \underbrace{\frac{iL\mu}{\pi v}\int_0^T d\tau\partial_\tau\phi_{\rm cl}^{\epsilon}(\tau)}_{S_{Bp}}, \tag{4.21}$$

where we integrated over the position and used Eq. (4.18) to simplify the action. Calculating the integral for the soliton, one finds the kinetic term,

$$\begin{aligned}
S_0 &= \lim_{T\to\infty}\frac{Ln}{\pi\nu}\int_{T/2}^{T/2} d\tau\frac{4}{n^2}[\partial_\tau\phi_{\rm cl}^{\epsilon}(\tau)]^2 = \lim_{T\to\infty}\frac{Ln}{\pi\nu}\int_{T/2}^{T/2} d\tau\left[\frac{\omega e^{\omega(\tau-\tau_0)}}{1+e^{2\omega(\tau-\tau_0)}}\right]^2 \\
&= \lim_{T\to\infty}\frac{2L\omega}{n\pi\nu}\int_{u(-T/2)}^{u(T/2)}\frac{du}{u^2} \qquad u(t) = 1+e^{2\omega(\tau-\tau_0)},\ du = 2\omega e^{2\omega(\tau-\tau_0)}, \\
&= -\lim_{T\to\infty}\frac{2L\omega}{n\pi\nu}\left[\frac{1}{u(T/2)} - \frac{1}{-u(T/2)}\right] \\
&= \frac{2L\omega}{n\pi\nu},
\end{aligned} \tag{4.22}$$

and the Berry phase contribution

$$\begin{aligned} S_{B-p} &= \lim_{T\to\infty} \frac{iL\mu}{\pi\nu} \int_{T/2}^{T/2} d\tau \partial_\tau \phi_{\rm cl}^\epsilon(\tau) = \lim_{T\to\infty} \frac{iL\mu}{\pi\nu} \phi_{\rm cl}^\epsilon \Big|_{-T/2}^{T/2} \\ &= \pm \lim_{T\to\infty} \frac{iL\mu}{\pi\nu} \left[\arctan(e^{\omega(T/2-\tau_0)}) - \arctan(e^{\omega(-T/2-\tau_0)})\right] \\ &= i\epsilon\gamma, \end{aligned} \tag{4.23}$$

with $\gamma = L\mu/nv$. As the classical soliton interpolates between $|j\rangle$ and $|j+\epsilon\rangle$, this allows us to identify the transition rate between these two stationary states. By calculating the path integral with fluctuations η around the classical solution, the quantum amplitude of a transition starting in state $|j\rangle$ at imaginary time $\tau = 0$ and ending in state $|j+\epsilon\rangle$ at $\tau = T$ is given by

$$G^\epsilon = \langle j+\epsilon| \, e^{-HT} \, |j\rangle = \int \mathcal{D}[\phi] e^{-S[\phi]} = \int \mathcal{D}[\eta] e^{-S[\phi_{\rm cl}^\epsilon + \eta]} \tag{4.24}$$

So far, we have only considered the classical solution, however quantum fluctuations have an important contribution. In the semiclassical limit, we consider the action around the classical solution, such that the field is $\phi = \phi_{\rm cl}^\epsilon + \eta$. The idea is to expand the action in terms of fluctuations[4], η, and use the saddle point approximation. Again, we separate the action in terms of kinetic and Berry-phase contribution $S[\phi] = S_0[\phi] + S_{B-p}[\phi]$. The kinetic part is[5]

$$S_0[\phi^\epsilon] = \int d\tau \int dx \left\{ \frac{n}{2\pi\nu} [\partial_\tau \phi_{\rm cl}^\epsilon + \partial_\tau \eta]^2 + \frac{n\nu}{2\pi} [\partial_x \eta]^2] + \frac{\Delta}{\pi n \xi} [\sin(2n\phi_{\rm cl}^\epsilon + 2n\eta) + 1] \right\}, \tag{4.25}$$

and we want to rewrite as an expansion in terms of η

$$S_0[\phi^\epsilon] := S_0[\phi_{\rm cl}^\epsilon] + \frac{\delta S_0[\phi_{\rm cl}^\epsilon]}{\delta\phi} \eta + \frac{1}{2} \frac{\delta^2 S_0[\phi_{\rm cl}^\epsilon]}{\delta\phi^2} \eta^2 + O(\eta^3). \tag{4.26}$$

Before calculating the functional derivatives, let us rewrite Eq. (4.25),

$$\begin{aligned} \int d\tau \int dx [\partial_\tau \phi_{\rm cl}^\epsilon + \partial_\tau \eta]^2 &= \int d\tau \int dx [\partial_\tau \phi_{\rm cl}^\epsilon]^2 + [\partial_\tau \eta]^2 + 2[\partial_\tau \phi_{\rm cl}^\epsilon][\partial_\tau \eta] \\ &= \int d\tau \int dx [\partial_\tau \phi_{\rm cl}^\epsilon]^2 + [\partial_\tau \eta]^2 - 2[\partial_\tau^2 \phi_{\rm cl}^\epsilon]\eta + b.t. \\ &= \int d\tau \int dx [\partial_\tau \phi_{\rm cl}^\epsilon]^2 - \eta[\partial_\tau^2 \eta] - 2[\partial_\tau^2 \phi_{\rm cl}^\epsilon]\eta + b.t., \end{aligned} \tag{4.27}$$

where we integrated by parts in the second line ($[\partial_\tau \phi_{\rm cl}^\epsilon][\partial_\tau \eta]$) and in the third line ($[\partial_\tau \eta]^2$),

[4] η must vanish at the boundaries.

[5] Other than the vanishing boundary term, we don't impose any constraint in η regarding the dependency on x-direction.

since η vanishes at the boundary, all boundary terms (b.t.) are zero. We can do the same procedure for the partial derivative in the x direction

$$\int d\tau \int dx[\partial_x \eta]^2 = -\int d\tau \int dx\ \eta[\partial_x^2 \eta] + b.t., \tag{4.28}$$

and we can expend the potential term around $\phi_{\rm cl}^\epsilon$,

$$\sin(2n\phi_{\rm cl}^\epsilon + 2n\eta) = \sin(2n\phi_{\rm cl}^\epsilon) + 2n\cos(2n\phi_{\rm cl}^\epsilon)\eta - 2n^2\sin(2n\phi_{\rm cl}^\epsilon)\eta^2 + O(\eta^3). \tag{4.29}$$

Now we can compare Eq. (4.25) with Eq. (4.26) using Eqs. (4.27-4.29),

$$\frac{\delta S_0[\phi_{\rm cl}^\epsilon]}{\delta\phi}\eta = \int d\tau \int dx \left\{ -\frac{n}{\pi\nu}[\partial_\tau^2 \phi_{\rm cl}^\epsilon] + \frac{2\Delta}{\pi n\xi}\cos(2n\phi_{\rm cl}^\epsilon) \right\} \eta = 0, \tag{4.30}$$

where we used the equation of motion, Eq. (4.18), to show the first order derivative is zero. We can do the same for the second order,

$$\begin{aligned}
\frac{1}{2}\frac{\delta^2 S_0[\phi_{\rm cl}^\epsilon]}{\delta\phi^2}\eta^2 &= \int d\tau \int dx \left\{ -\frac{n}{2\pi\nu}\eta[\partial_\tau^2\eta] - \frac{n\nu}{2\pi}\eta[\partial_x^2\eta] - \frac{2n\Delta}{\pi n\xi}\sin(2n\phi_{\rm cl}^\epsilon) \right\} \eta^2, \\
&= -\frac{1}{2}\frac{n}{\pi\nu}\int d\tau \int dx\ \eta \left[-\partial_\tau^2 - \nu^2\partial_x^2 - \frac{4\Delta\nu}{\xi}\sin(2n\phi_{\rm cl}^\epsilon) \right]\ \eta, \\
&= -\frac{1}{2}\frac{n}{\pi\nu}\int d\tau \int dx\ \eta\hat{F}^\epsilon\eta = S_\eta^\epsilon,
\end{aligned} \tag{4.31}$$

$\hat{F}^\epsilon = -\partial_\tau^2 - v^2\partial_x^2 + \omega^2\sin(2n\phi_{\rm cl}^\epsilon)$ is the differential operator associated with the fluctuations. The Berry phase action can be trivially calculated using the fact that the boundary terms are zero,

$$S_{B-p}[\phi_{\rm cl}^\epsilon + \eta] = \frac{i\mu}{\pi\nu}\int d\tau \int dx\ \{\partial_\tau\phi_{\rm cl}^\epsilon + \partial_\tau\eta\} = S_{B-p}[\phi_{\rm cl}^\epsilon] + b.t. = S_{B-p}[\phi_{\rm cl}^\epsilon]. \tag{4.32}$$

Now, we are ready to calculate the path integral of one instanton going from one minimum to an adjacent minimum (j to $j+\epsilon$), such that

$$\begin{aligned}
G^\epsilon &= \int \mathcal{D}[\eta] e^{-(S_0[\phi_{\rm cl}^\epsilon] + \frac{\delta S_0[\phi_{\rm cl}^\epsilon]}{\delta\phi}\eta + \frac{1}{2}\frac{\delta^2 S_0[\phi_{\rm cl}^\epsilon]}{\delta\phi^2}\eta^2 + S_{B-p}[\phi_{\rm cl}^\epsilon])} \\
&= e^{-S_0 - i\epsilon\gamma}\int \mathcal{D}[\eta] e^{-\frac{1}{2}\frac{\delta^2 S}{\delta\phi^2}[\phi_{\rm cl}^\epsilon]\eta^2} = e^{-S_0 - i\epsilon\gamma}\int \mathcal{D}[\eta] e^{-\frac{1}{2}\frac{n}{\pi\nu}\int\int d\tau dx\ \eta\hat{F}^\epsilon\eta} \\
&= T\sqrt{\frac{\pi\nu S_0}{n}} e^{-S_0 - i\epsilon\gamma}\int \mathcal{D}'[\eta] e^{-\frac{1}{2}\frac{n}{\pi\nu}\int\int d\tau dx\ \eta\hat{F}^\epsilon\eta} \\
&= T\sqrt{\frac{\pi\nu S_0}{n}} e^{-S_0 - i\epsilon\gamma}\mathcal{N}\sqrt{\frac{\pi\nu}{n}}\det{}'[F^\epsilon]^{-1/2}.
\end{aligned} \tag{4.33}$$

where in the first line we expanded the action around classical solitons between states $|j\rangle$

and $|j \pm 1\rangle$, such that we have a Gaussian integral over all fluctuations $\eta(x,t)$ vanishing at the boundaries. In the third line, the translation-invariant zero mode is integrated out and creates a factor $T\sqrt{\pi v S_0/n}$ [125, 126], see Appendix E. The remaining integral without zero modes (denoted by the prime in the path integral measure) is Gaussian. By computing the Gaussian integral in the second line we obtain the determinant without zero-modes, $\det'[\hat{F}^\epsilon]$, multiplied by $\mathcal{N}$, the normalization constant from the measure $\mathcal{D}'[\eta]$ [125].

Following Refs. [125, 128] the determinant can be calculated by multiplying and dividing by $\det[\hat{F}_0]^{-1/2}$, where $\hat{F}_0 = -\partial_\tau^2 - v^2\partial_x^2 + \omega^2$ is the differential operator of a harmonic oscillator, and computing the ratio of determinants using the zeta regularization method for a Neumann boundary condition [139][6],

$$\frac{\det[\hat{F}_0]^{1/2}}{\det'[\hat{F}^\epsilon]^{1/2}} = \sqrt{\frac{\omega}{L}}. \tag{4.34}$$

As a result, the transition rate becomes

$$G^\epsilon = T\mathcal{N}e^{-\omega T/2}\mathcal{K}e^{-S_0 - i\epsilon\gamma}, \tag{4.35}$$

where $\mathcal{K} = \omega/(\pi\sqrt{n})$. We identify in the results for G^+ and G^- the transition amplitude arising from an instanton as $[\mathcal{I}] = \mathcal{K}e^{-S_0 - i\gamma}$ and for an anti-instanton as $[\bar{\mathcal{I}}] = [\mathcal{I}]^*$. The exponential $e^{-\omega T/2}$ comes from the factor $(\det[\hat{F}_0])^{-1/2}$ and is associated with the energy of a harmonic oscillator.

Next, we normalize the stationary states $|j_+\rangle$ and $|j_-\rangle$ with the factor $\sqrt{\mathcal{N}}$, and calculate, within the one-instanton approximation, the most general trajectory between them as that consisting of all possible combinations of well-separated instantons and anti-instantons,

$$\begin{aligned}
\langle j_+|\, e^{-HT}\, |j_-\rangle &= e^{-\omega T/2}\sum_{\{n_t\}}\delta_{n_t, j_+ - j_-}\frac{(T[\mathcal{I}])^{n_\mathcal{I}}}{n_\mathcal{I}!}\frac{(T[\bar{\mathcal{I}}])^{n_{\bar{\mathcal{I}}}}}{n_{\bar{\mathcal{I}}}!} \\
&= \frac{e^{-\omega T/2}}{2n}\sum_{\{n_t\}}\sum_{q=0}^{2n-1} e^{\frac{i\pi q(j_- - j_+)}{n}}\frac{(T[\mathcal{I}]e^{\frac{i\pi q}{n}})^{n_\mathcal{I}}}{n_\mathcal{I}!}\frac{(T[\bar{\mathcal{I}}]e^{\frac{-i\pi q}{n}})^{n_{\bar{\mathcal{I}}}}}{n_{\bar{\mathcal{I}}}!} \\
&= \frac{e^{-\omega T/2}}{2n}\sum_{q=0}^{2n-1} e^{\frac{i\pi q(j_- - j_+)}{n}} e^{2\mathcal{K}Te^{-S_0}\cos(\frac{\pi q}{n} - \gamma)},
\end{aligned} \tag{4.36}$$

where we summed over all combinations of $n_\mathcal{I}$ and $n_{\bar{\mathcal{I}}}$ with $n_t = n_\mathcal{I} - n_{\bar{\mathcal{I}}}$. In the second line we used the summation form of the Dirac delta function, expanding n_t and distributing the exponential $e^{\pm i\pi q}$ together with the instanton amplitude.

To obtain an expression for the energy splitting, we expand $\langle j_+|\, e^{-HT}\, |j_-\rangle$ in terms of the eigenstates of a general two-parafermion Hamiltonian and we compare both expres-

[6] This calculation goes beyond the scope of this thesis. For a detailed calculation see Ref. [140].

sions. The eigenstates $|q\rangle$ of the effective low-energy parafermion Hamiltonian (4.13) are similar to Bloch waves and can be written as linear combinations in the $|j\rangle$ basis [139]. By noticing that $|j\rangle = |j + 2n\rangle$ due the periodicity of the sine function we can write

$$|q\rangle = \sqrt{\frac{1}{2n}} \sum_{j=0}^{2n-1} e^{-i\pi qj/n} |j\rangle . \tag{4.37}$$

By considering the completeness of the basis $|q\rangle$ we can expand $|j_\pm\rangle$ to obtain

$$\langle j_+| e^{-HT} |j_-\rangle = \frac{1}{2n} \sum_q \langle j_+|q\rangle \langle q|j_-\rangle e^{-E(q)T}. \tag{4.38}$$

Neglecting the constant energy $\omega/2$, we can set equal Eq. (4.38) and Eq. (4.36), to arrive at

$$E(q) = -\frac{2\omega e^{-S_0}}{\pi\sqrt{n}} \cos\left(\frac{\pi q}{n} - \frac{\mu L}{nv}\right). \tag{4.39}$$

We note that $E(q)$ decays exponentially as $\propto e^{-L\omega}$, whereas the chemical potential gives rise to a typical oscillation [128]. A final equality between Eq. (4.39) and Eq. (4.16) relates the parafermion tight binding parameters to the microscopic model constants,

$$t_1 = \frac{\omega}{\pi\sqrt{n}} e^{-S_0}, \quad \lambda_1 = -\frac{\mu L}{nv} + \frac{\pi}{2n}. \tag{4.40}$$

In the dilute one-instanton gas approximation, all higher order hopping processes are neglected, i.e., $t_k = 0$ for $k > 1$.

4.2.2 Beyond the dilute one-instanton gas

Moving beyond the dilute one-instanton gas approximation, we consider now a system composed of instantons and bi-instantons, the latter corresponding to a correlated two-instanton event [133–135]. In such a bi-instanton, the change of $\phi(\tau)$ during the transition is still fast compared to the distance between two instantons, but in contrast to the instanton gas limit, this distance is not infinite [134].

In contrast to a single instanton, the bi-instanton is not an *exact* solution of the classical Euler-Lagrange equation and has a different winding number. Nonetheless, it is a solution up to a correction which is exponentially small in the distance between the instantons, so it can have a significant contribution to the quantum mechanical path integral. Bi-instantons will have an energy scale of the order e^{-2S_0} [125] but interactions between the two instantons produce corrections to this energy [132]. The bi-instanton

"solution" we want Eq. (4.20) has the following limits

$$\begin{aligned}\phi^{\epsilon_1\epsilon_2} &\sim -\frac{\pi}{4n} + \epsilon_1\frac{\pi}{n} + \epsilon_1\frac{2}{n}e^{-\omega\tau} \qquad \text{as } \tau \to \infty \\ &\sim -\frac{\pi}{4n} + \epsilon_2\frac{2}{n}e^{\omega\tau} \qquad\qquad \text{as } \tau \to -\infty \end{aligned} \tag{4.41}$$

We consider the action for a configuration of two instantons at positions $\pm\tau_0$ given by (for $\epsilon_1, \epsilon_2 = \pm$)

$$\phi^{\epsilon_1\epsilon_2}(\tau) = -\frac{\pi}{4n} + \epsilon_1 f_+(\tau) + \epsilon_2 f_-(\tau), \tag{4.42}$$

where

$$f_\pm(\tau) = \frac{2}{n}\text{arctan}\left[e^{\omega(\tau\mp\tau_0)}\right], \tag{4.43}$$

For $\epsilon_1 = \epsilon_2$ such a configuration describes a pair of instantons ($\epsilon_{1,2} = 1$) or anti-instantons ($\epsilon_{1,2} = -1$), whereas for $\epsilon_1 = -\epsilon_2$, the field describes an instanton anti-instanton pair.

Now, we calculate the classical action corresponding to $\phi^{+\epsilon_2}(\tau)$. It can be easily generalized for $\phi^{\epsilon_1\epsilon_2}(\tau)$. In order to do this, we will separate the action, without the Berry phase, in two parts $S_+(\phi)$ and $S_-(\phi)$, such that[7]

$$\begin{aligned} S_+[\phi^{+\epsilon_2}] &= \frac{nL}{\pi\nu}\int_0^\infty d\tau \frac{1}{2}(\dot{\phi}^{+\epsilon_2})^2 + \frac{\omega^2}{4n^2}V(\phi^{+\epsilon_2}) \\ S_-[\phi^{+\epsilon_2}] &= \frac{nL}{\pi\nu}\int_{-\infty}^0 d\tau \frac{1}{2}(\dot{\phi}^{+\epsilon_2})^2 + \frac{\omega^2}{4n^2}V(\phi^{+\epsilon_2}) \end{aligned} \tag{4.44}$$

where we already integrated over dx and $V(\phi) = \sin(2n\phi) + 1$. The choice to integrate starting or ending at $\tau = 0$ is arbitrary, indeed we could choose any value τ_1 as long as $\tau_1 \ll \tau_0$. Here we assume $\tau_0 \gg 1$, in this case f_+ is small for $\tau < 0$ and f_- is small $\tau > 0$. We will focus on S_+ expanding it around $f_- = 0$, but, the same could be done to S_- around f_+ and yield an analogous result.

$$\begin{aligned} S_+[\phi^{+\epsilon_2}] &= \frac{nL}{\pi\nu}\int_0^\infty d\tau \frac{1}{2}(\dot{\phi}^{+\epsilon_2})^2 + \frac{\omega^2}{4n^2}V(\phi^{+\epsilon_2}) \\ &= \frac{nL}{\pi\nu}\int_0^\infty d\tau \left\{\left[\frac{1}{2}\dot{f}_+^2 + \frac{\omega^2}{4n^2}V(\frac{\pi}{4n} + f_+)\right] + \epsilon_2\left[\dot{f}_+\dot{f}_- + \frac{\omega^2}{4n^2}V'(\frac{\pi}{4n} + f_+)f_-\right]\right. \\ &\quad \left. + \left[\frac{1}{2}\dot{f}_-^2 + \frac{1}{2}\frac{\omega^2}{4n^2}V''(\frac{\pi}{4n} + f_+)f_-^2\right]\right\}. \end{aligned} \tag{4.45}$$

The first and third terms are part of the classical action of the solitons centered at τ_0 and

[7] To simplify the notation here, we use the dot to denote ∂_τ and prime to denote ∂_f.

$-\tau_0$. This can be seen by rewriting $\frac{1}{2}V''(\frac{\pi}{4n}+f_+)f_-^2 \approx V(\frac{\pi}{4n}+f_-)$, which can be seen

$$\begin{aligned} V''(\frac{\pi}{4n}+f_+)f_-^2 &= -4n^2\sin(\pi/2+2nf_+)f_-^2 \approx -4n^2\sin(\pi/2+2\pi+4e^{-\omega\tau_0})f_-^2 \\ &= -4n^2\cos(4e^{-\omega\tau_0})f_-^2 \approx -4n^2f_-^2+2-2 \approx 2(-\cos(2nf_-)+1) \\ &= 2[\sin(-\pi/2+2nf_-)+1] = 2[\sin(2([-\frac{\pi}{4n}+f_-))+1]. \end{aligned} \tag{4.46}$$

For the linear term in f_- of S_+, we integrate by parts

$$\begin{aligned} \int_0^\infty d\tau \dot{f}_+\dot{f}_- + \frac{\omega^2}{4n^2}V'(\frac{\pi}{4n}+f_+)f_- &= \dot{f}_+f_-\big|_0^\infty + \int d\tau\left[-\ddot{f}_+f_- + \frac{\omega^2}{4n^2}V'(\frac{\pi}{4n}+f_+)f_-\right] \\ = \dot{f}_+f_-\big|_0^\infty &= \frac{4\omega}{n^2}\frac{e^{\omega(\tau-\tau_0)}}{(1+e^{\omega(\tau-\tau_0)})^2}\arctan(e^{\omega(\tau-\tau_0)})\big|_0^\infty \approx \frac{4\omega}{n^2}e^{-2\omega\tau_0}, \end{aligned} \tag{4.47}$$

where we use the equation of motion, Eq. (4.18), in the second line ($V'(\frac{\pi}{4n}+f_+) = \frac{4n^2}{\omega^2}\ddot{f}_+$). Doing the same procedure to S_- we obtain

$$S[\phi^{\epsilon_1\epsilon_2}] = 2S_0 + \frac{8\epsilon_1\epsilon_2\omega L}{\pi\nu n}e^{-2\omega\tau_0} + i(\epsilon_1+\epsilon_2)\gamma = 2S_0 + 4\epsilon_1\epsilon_2 S_0 e^{-2\omega\tau_0} + i(\epsilon_1+\epsilon_2)\gamma. \tag{4.48}$$

The "classical" action of such a bi-instanton is twice the classical action of a single instanton plus a positive (negative) energy due to the repulsive (attractive) interaction between instanton and (anti-) instanton. In the following, we focus on the case $\epsilon_1 = \epsilon_2$ because it does contribute to the energy splitting, as opposed to $\epsilon_1 = -\epsilon_2$ which merely adds a overall constant to the energies: an instanton-anti-instanton pair does not allow additional transitions between different $|j\rangle$, so it just adds a constant value to the energies.

By direct application of the concepts previously introduced for the dilute one-instanton gas, we compute the transition rate due to a single bi-instanton

$$\begin{aligned} G^{\epsilon\epsilon} &= \langle j+2\epsilon|\, e^{-HT}\,|j\rangle = \int \mathcal{D}[\phi]e^{-S[\phi]} = \int \mathcal{D}[\eta]e^{-S[\phi^{\epsilon\epsilon}+\eta]} \\ &= \int \mathcal{D}[\eta]e^{-(S_0[\phi^{\epsilon\epsilon}]+\frac{\delta S_0[\phi^{\epsilon\epsilon}]}{\delta\phi}\eta+\frac{1}{2}\frac{\delta^2 S_0[\phi^{\epsilon\epsilon}]}{\delta\phi^2}\eta^2+S_{B-p}[\phi^{\epsilon\epsilon}])} \\ &= e^{-2S_0-2i\epsilon\gamma}\int \mathcal{D}[\eta]e^{-4S_0e^{-\omega z}}e^{-\frac{1}{2}\frac{\delta^2 S}{\delta\phi^2}[\phi^{\epsilon\epsilon}]\eta^2} \\ &= e^{-2S_0-2i\epsilon\gamma}\int \mathcal{D}[\eta]e^{-4S_0e^{-\omega z}}e^{-\frac{1}{2}\frac{n}{\pi\nu}\int\int d\tau dx\ \eta\hat{M}^{\epsilon\epsilon}\eta} \\ &= T\frac{\pi\nu S_0}{n}e^{-2S_0-2i\epsilon\gamma}\int dz\ e^{-4S_0e^{-\omega z}}\int \mathcal{D}'[\eta]e^{-\frac{1}{2}\frac{n}{\pi\nu}\int\int d\tau dx\ \eta\hat{M}^{\epsilon\epsilon}\eta} \\ &= T(\mathcal{N}e^{-\frac{\omega}{2}\frac{T}{}})(\mathcal{K}^2e^{-2S_0-2i\epsilon\gamma}\int dz\ e^{-4S_0e^{-\omega z}}), \end{aligned} \tag{4.49}$$

where we followed the same procedure as in Eq. (4.33), with the translational invariance of the bi-instanton center of mass now being responsible for the zero-mode. Here, z is the dis-

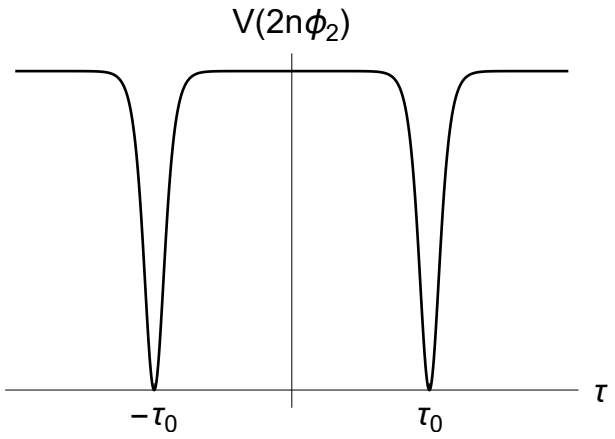

Figure 4.2: Illustration of $V(\phi^{\epsilon\epsilon})$. For $\tau_0 \gg 1$ the eigenvalues of $\hat{M}$ will be two-fold degenerate.

tance between the centers of the two instantons and $\hat{M}^{\epsilon\epsilon} = -\partial_\tau^2 - v^2\partial_x^2 + (4\Delta v/\xi)\sin(2n\phi^{\epsilon\epsilon})$ is the differential operator associated with the bi-instanton. The eigenvalues of M are two-fold degenerate so $\det'[\hat{M}^{\epsilon\epsilon}] = (\det'[\hat{F}^{\epsilon}])^2$ [133], this can be seen by assuming the solutions are far apart($\tau_0 \gg 1$). In this case, the operator M has the form of a Hamiltonian with two asymptotically identical wells coming from the sines, see Fig. 4.2. At leading order, the spectrum will be the same as the one instanton, but twice degenerate, with corrections exponentially small. To suppress the zero-energy modes, we can introduce two collective variables, similar to the procedure for one instanton.

The correction to the bi-instanton amplitude due to the instanton interactions, $[\mathcal{I}\mathcal{I}] = [\mathcal{I}]^2 \int dz e^{-4S_0} e^{-\omega z}$, can be simplified by using the semiclassical approximation $S_0 \gg 1$ and by introducing a regularization parameter c [135] in the instanton-instanton interaction Eq. (4.48),

$$\begin{aligned}
&\lim_{c\to 0} \int_0^\infty dz e^{-4S_0 e^{-\omega z} - c\omega z} \\
&\quad = \frac{1}{\omega} \lim_{c\to 0} \left(\frac{1}{4S_0}\right)^c \int_0^{4S_0} ds e^{-s} s^{c-1} \approx \frac{1}{\omega} \lim_{c\to 0} \left(\frac{1}{4S_0}\right)^c \Gamma(c) \\
&\quad = -\frac{1}{\omega}\left[\gamma_E + \log(4S_0)\right] + \mathcal{O}(1/c),
\end{aligned} \tag{4.50}$$

where $\gamma_E \approx 0.5772$ is the Euler number and we need to subtract the divergent term $\mathcal{O}(1/c)$ which corresponds to non-interacting instantons. We proceed by generalizing Eq. (4.36) to a gas consisting of both instantons and bi-instantons, which we call a dilute two-instanton gas approximation. Between two normalized stationary states $|j_+\rangle$ and $|j_-\rangle$ we consider

all possible combinations of (anti-)instantons and (anti-)bi-instantons

$$\begin{aligned}\langle j_+|\, e^{-HT}\, |j_-\rangle &= e^{-\omega T/2}\sum_{\{n_t\}}\delta_{n_t,j_+-j_-}\frac{(T[\mathcal{I}])^{n_{\mathcal{I}}}}{n_{\mathcal{I}}!}\frac{(T[\bar{\mathcal{I}}])^{n_{\bar{\mathcal{I}}}}}{n_{\bar{\mathcal{I}}}!}\frac{(T[\mathcal{I}\mathcal{I}])^{n_{\mathcal{I}\mathcal{I}}}}{n_{\mathcal{I}\mathcal{I}}!}\frac{(T[\bar{\mathcal{I}}\bar{\mathcal{I}}])^{n_{\bar{\mathcal{I}}\bar{\mathcal{I}}}}}{n_{\bar{\mathcal{I}}\bar{\mathcal{I}}}!} \\ &= \frac{e^{-\omega T/2}}{2n}\sum_{q=0}^{2n-1} e^{\frac{i\pi q(j_- - j_+)}{n}} e^{2\mathcal{K}Te^{-S_0}\cos(\frac{\pi q}{n}-\gamma)} e^{-\frac{2}{\omega}[\gamma_E+\log(4S_0)]\mathcal{K}^2Te^{-2S_0}\cos(\frac{2\pi q}{n}-2\gamma)},\end{aligned} \tag{4.51}$$

where $n_t = n_{\mathcal{I}} - n_{\bar{\mathcal{I}}} + 2n_{\mathcal{I}\mathcal{I}} - 2n_{\bar{\mathcal{I}}\bar{\mathcal{I}}}$ is the net number of instantons. By comparing Eq. (4.51) with Eq. (4.38), it is possible to obtain the energy splitting including the subleading correction due to bi-instantons,

$$\begin{aligned}E(q) = &-\frac{2\omega}{\pi\sqrt{n}}e^{-S_0}\cos\left(\frac{\pi q}{n}-\frac{\mu L}{nv}\right) \\ &+\frac{2\omega}{\pi^2 n}[\gamma_E+\log(4S_0)]e^{-2S_0}\cos\left(\frac{2\pi q}{n}-\frac{2\mu L}{nv}\right).\end{aligned} \tag{4.52}$$

In Fig. 4.3 we show the energy splitting for a $\mathbb{Z}_4$ parafermion ($n = 2$), comparing the result for the dilute one-instanton gas (4.39) (dashed line) with the corrected result including bi-instantons (4.52) (solid line) for a value $\sqrt{2}e^{-S_0} = \pi$ and $[\gamma_E + \log(4S_0)]/2 = 0.1$. While energy crossings between two consecutive q mod 4 occur at the same energy, the crossings between q and $q+2$ mod 4 are shifted. By setting equal Eq. (4.52) and Eq. (4.16), we recover the leading order result (4.39), and in addition the second-order coupling amplitude and phase,

$$\begin{aligned}t_2 &= \frac{\omega}{\pi^2 n}\left[\gamma_E+\log(4S_0)\right]e^{-2S_0}, \\ \lambda_2 &= -\frac{2\mu L}{nv}+\frac{2\pi}{n}.\end{aligned} \tag{4.53}$$

In this section, we have so far ignored the contribution of instanton anti-instanton pair since it doesn't contribute to the energy splitting. For completeness sake, we now show the pair's amplitude that would be added in the "gas". There is,however, a problem that arises when we try to calculate the integral of $[\mathcal{I}\bar{\mathcal{I}}]$. In this case, the integral becomes divergent as $1/S_0 \to 0$, and for regions with small z the integral is ill defined in the limit $1/S_0 \ll 1$. In order to solve this problem, we consider $-S_0 > 0$ and analytically continue back to $1/S_0 > 0$ in the complex plane. This can be done with two different paths

$$\begin{aligned}[\mathcal{I}\bar{\mathcal{I}}]/(\mathcal{K}^2e^{-2S_0}) &\xrightarrow{1/|S_0|\ll 1} \frac{1}{\omega}\lim_{c\to}(-\frac{1}{4S_0})^c\Gamma(c) \\ \xrightarrow{-1/4S_0\to e^{\mp i\pi}/4S_0} -\frac{1}{\omega}(\gamma_E+\log(\frac{4S_0}{e^{\mp i\pi}})) &= -\frac{1}{\omega}(\gamma_E+\log(4S_0))\mp\frac{1}{\omega}i\pi.\end{aligned} \tag{4.54}$$

To solve the ambiguity problem of the imaginary part, is necessary to use ressurgence the-

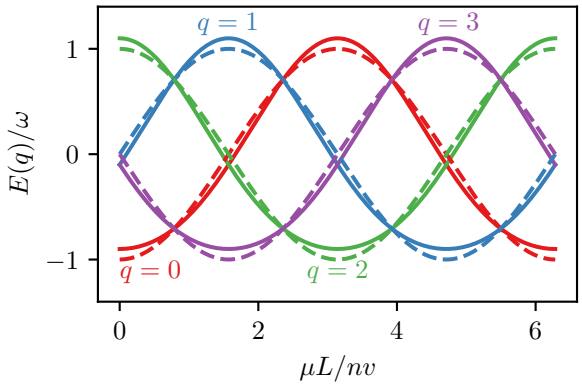

Figure 4.3: Energy splitting for ground states with different q as function of chemical potential. The dashed line corresponds to the one-instanton energy corresponding to only two-parafermion interactions. The solid line corresponds to the energy including four-parafermion terms (bi-instantons corrections), with parameters corresponding to $t_2 = 0.1t_1$. The major difference between these two cases are the shifts in the energy crossing at $E = 0$.

ory[8] and the ambiguity should cancel with the same ambiguity of the non-borel summable series arising from perturbation theory [134, 135]. We can safely ignore the imaginary part and we get an expression analogous to the bi-instanton.

4.3 Monte Carlo

We start with a discretization of the action (4.4), using a lattice constant a_x and time step a_τ. In the following, we set $v = 1$, which leads to

$$S[\phi] = \frac{n}{2\pi}\sum_{i=1}^{N_\tau}\sum_{j=1}^{N_x}\left\{\frac{a_x}{a_\tau}(\phi_{\tau_{i+1},x_j} - \phi_{\tau_i,x_j})^2 + \frac{a_\tau}{a_x}(\phi_{\tau_i,x_{j+1}} - \phi_{\tau_i,x_j})^2 + \frac{\omega^2 a_x a_\tau}{2n^2}\sin(2n\phi_{\tau_i,x_j}) + \frac{2i\mu a_x}{n}(\phi_{\tau_{i+1},x_j} - \phi_{\tau_i,x_j})\right\}, \tag{4.55}$$

where $\tau_i = ia_\tau$ and $x_j = ja_x$. Moreover, N_x and N_τ are chosen such that $N_x a_x = L$ and $N_\tau a_\tau = T$. We choose a rectangular grid, $N_\tau = 100$ and set $a_x = a_\tau = a$.

To simulate instanton configurations which connect states $|j_-\rangle$ and $|j_+\rangle$, we assume a twisted boundary condition in the τ direction, such that $\phi_{\tau_{N_\tau+1},x_i} = \phi_{\tau_1,x_i} + \pi\delta Q/n$ [141], where $\delta Q = j_+ - j_-$ is an integer. This condition is enforced in the simulation via an energy penalty $\frac{na_x}{2\pi a_\tau}(\phi_{\tau_1,x_j} - \phi_{\tau_{N_\tau},x_j} + \pi\delta Q/n)^2$, and causes the simulated configuration to

[8]The idea is to use perturbation theory to construct non-Borel summable divergent series, that converges in a small radius of interest.

have a net number δQ of instantons.

The spatial boundary condition are open, allowing the field to fluctuate freely in x direction. However, fields which fluctuate in x direction lead only to subleading contributions compared to configurations which are spatially constant.

The Monte Carlo algorithm is initialized with a vanishing configuration $\phi_{\tau_i,x_j} = 0$ for all i, j. In each Monte Carlo step, we propose a field update $\phi \to \phi'$, which is accepted with probability $P = \min(|\exp(-\alpha\Delta S)|, 1)$ that is determined by the change of the action $\Delta S = S[\phi'] - S[\phi]$. We introduced an additional parameter $\alpha \geq 1$ which will be explained shortly. Hence, if the updated action $S[\phi']$ is smaller than the original action $S[\phi]$, then $\Delta S < 0$ and the update will be accepted ($P = 1$). On the other hand, if $\Delta S > 0$, we draw a uniformly distributed random number $X \in [0, 1]$ and accept the proposed update if $X < P$. Otherwise, the update is rejected and the original field configuration is kept.

A "bead update" which randomly displaces the field along all imaginary time coordinates has a small acceptance rate which results in an inefficient simulation. To achieve an improved convergence towards fluctuations around the classical saddle point solutions of the path integral, we implemented a local field update scheme at the level of individual nodes, i.e., $\phi'_{\tau_i,x_j} = \phi_{\tau_i,x_j} + \delta\phi$, at a random position (i, j) where $\delta\phi \in [-\delta, \delta]$ is a uniform random displacement and δ a dynamical interval width. After 100 Monte Carlo steps, we update δ depending on the acceptance rate. If the acceptance rate is below 0.6, we reduce δ to 0.8δ. Typically this means δ converges to 0.1. Since the action difference after a single local update is independent of the imaginary time T (interpreted as an inverse temperature), an artificial parameter α with $\alpha a_\tau \propto T$ is introduced to obtain a local importance sampling scheme corresponding to an average inverse temperature. We found optimal performance and fast convergence to fluctuations around the classical saddle point solutions for the choice $\alpha = N_\tau$.

Every 200 steps, we randomly attempt center of mass moves of the field along τ: For a fixed x_j, we propose a uniform shift of the field for all τ_i, i.e. $\boldsymbol{\phi}_{x_j} \to \boldsymbol{\phi}_{x_j} + \delta$ where $\boldsymbol{\phi}_{x_j} = (\phi_{\tau_1,x_j}, \phi_{\tau_2,x_j}, \ldots)$. The move is accepted according to the same criterion as for the individual node updates. By swapping τ and x, a center of mass shift is attempted along the spatial direction. This routine allows slight changes in the center of mass of instantons and improves convergence.

After the system equilibrates (we typically consider 10000 local updates, although the system usually converges in less than 5000), we store the final configuration. The simulation is restarted by creating either an instanton or an anti-instanton, with the same likelihood, at a random imaginary time τ after which we let the system equilibrate again. The creation/annihilation of instantons followed by equilibration is repeated 60 times before the next configuration is stored. Fig. 4.4 illustrate some of the configurations with $\delta Q = 1$ and 2 obtained by Monte Carlo.

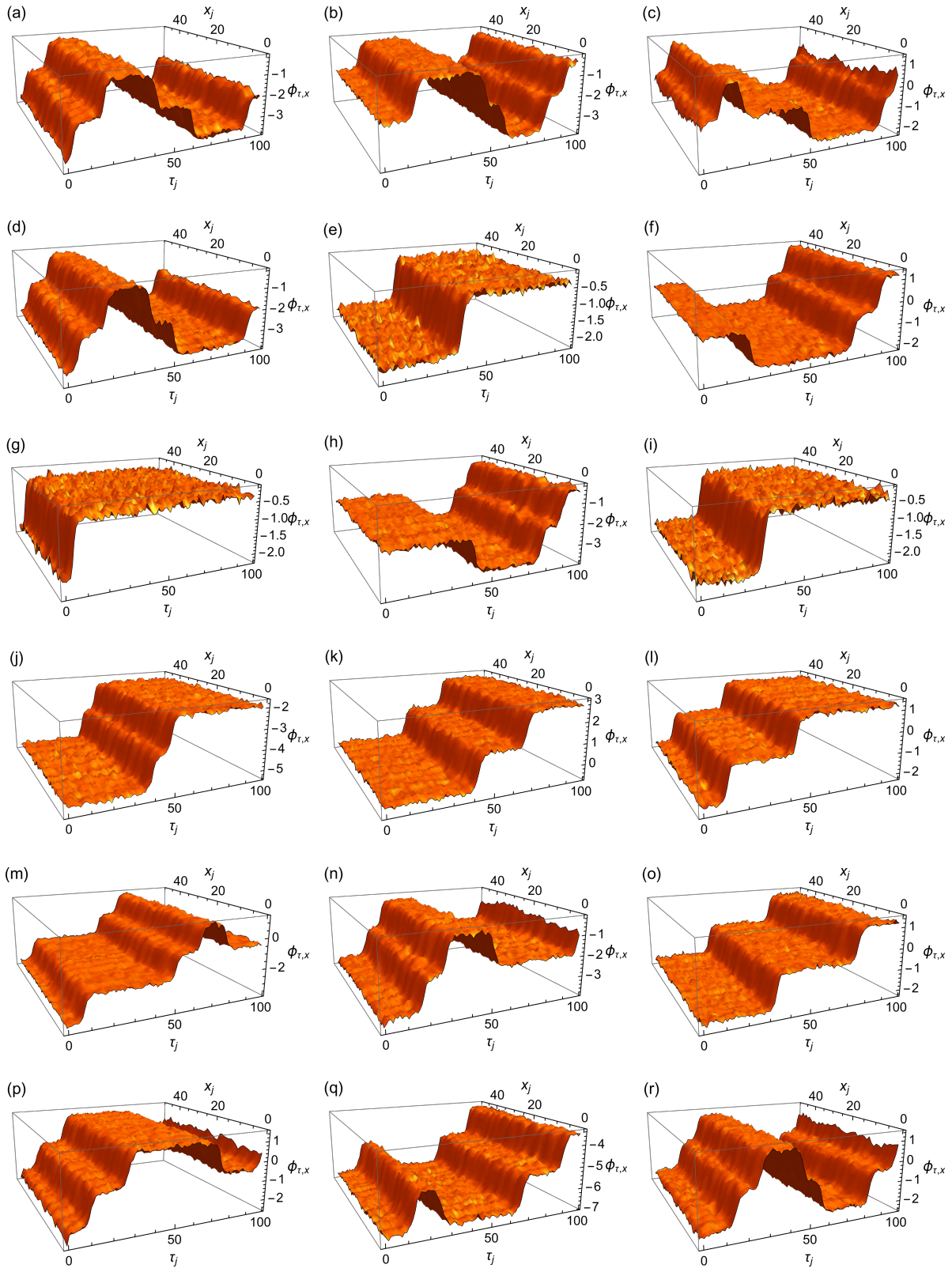

Figure 4.4: Different configurations generated by the Monte Carlo. (a-i) Fields with $\delta Q = 1$, (j-r) fields with $\delta Q = 2$. Note that, not only we have configurations with single and bi-instantons, but more exotic configurations with pairs of instantons and anti-instantons.

This procedure allows us to sample configurations in the neighborhood of different saddle points which otherwise cannot be reached in reasonable computation time. For each δQ, we collect $N_c = 3000$ configurations based on which we compute the observables explained in the following. To simulate the action, Eq. (4.55), we use $n = 2$, $\omega = \sqrt{2}$, $a = 0.6$ and $N_\tau = 100$. For each length N_x and chemical potential μ we simulated configurations with $0 \leq \delta Q \leq 2$.

The twisted boundary conditions effectively decouple different instanton sectors and allow us to simulate quantities such as Eqs. (4.33) and (4.49). Since all δQ sectors contribute to physical observables, we define the following average

$$\langle A \rangle_j = \frac{\sum_{\{\phi_j\}} A[\phi_j] e^{-S[\phi_j]}}{\sum_{\{\phi'_j\}} e^{-S[\phi'_j]}}, \tag{4.56}$$

where $\phi_{\delta Q}$ are configurations containing δQ instantons or anti-instantons (negative δQ). We denote the transition rates of δQ instantons as

$$G^{\delta Q}_{\mathrm{MC}} = \langle \delta Q | \, e^{-HT} \, |0\rangle = \langle e^{-S} \rangle_{\delta Q}. \tag{4.57}$$

The Monte Carlo result depends on a normalization constant $\mathcal{N}_{\mathrm{MC}}$ which is independent of δQ. To check the results we plot G^2_{MC} and G^1_{MC} [see Fig. 4.5(a)]. Fitting the expressions for $G^{1(2)}_{\mathrm{MC}} \approx e^{\omega T/2} \mathcal{N}_{\mathrm{MC}} G^{1(2)}/T$ we are able to determine $\mathcal{N}_{\mathrm{MC}} = e^{-2\sqrt{2}L/\pi}\sqrt{2}/\pi$, and this result holds for different choices of parameters (ω, T and $n = 2$). Note that even for small lengths, G^2_{MC} agrees with the analytical result even though it is near the region where the theory is no longer valid. Indeed we later show that the energy splitting deviates from the expected value in this region.

From the transition rates, we follow the derivation of Eq. (4.39) to compute the energy splitting. In particular, we note that Eq. (4.38) can be written as a Fourier transform of transition rates, i.e.

$$\sum_{\delta Q} \langle \delta Q | e^{-HT} | 0 \rangle \, e^{i\pi q' \delta Q/n} = \frac{1}{2n} \sum_{\delta Q} \sum_{q} e^{-i\pi(q-q')\delta Q/n} e^{-E(q)T} = e^{-E(q)T}, \tag{4.58}$$

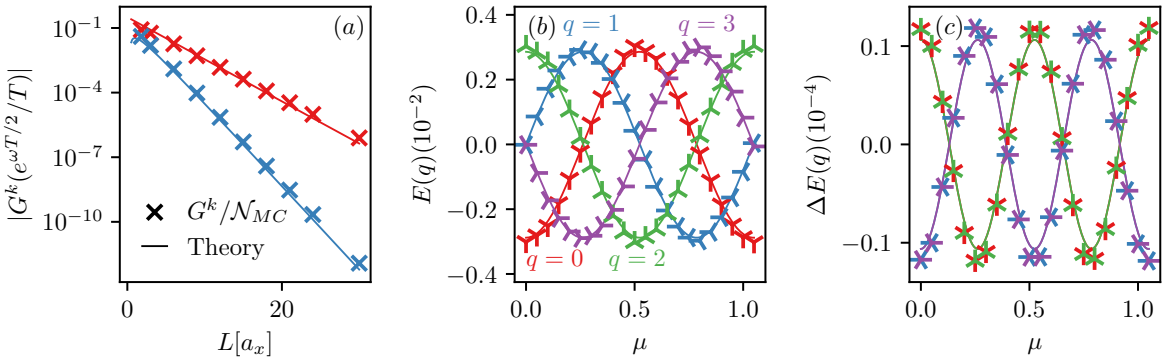

Figure 4.5: Comparison between Monte Carlo simulations and theory. (a) transition rates as function of length L, $\mu = 0$, obtained by Monte Carlo (crosses) are compared to the theory (lines) for $k = 1$ (red) and 2 (black). (b) energy splitting $E(q)$ as function of chemical potential for $L = 12$. The Monte Carlo simulation, Eq. (4.60), matches the theory, Eq. (4.52). The energy shift from bi-instantons is not clearly visible as it is two orders of magnitude lower. (c) correction due to bi-instantons, note that $q = 0, 2(1, 3)$ have the same value. The simulation (markers) also agrees with the theory (lines).

we follow by taking the log of both sides,

$$\begin{aligned}
E(q)T &= -\log\left(\sum_{\delta Q}\langle\delta Q|e^{-HT}|0\rangle\, e^{i\pi q\delta Q/n}\right)\\
&= -\log\left(\langle 0|e^{-HT}|0\rangle\right) - \log\left(1+\sum_{\delta Q\neq 0}\frac{\langle\delta Q|e^{-HT}|0\rangle}{\langle 0|e^{-HT}|0\rangle}e^{i\pi q'\delta Q/n}\right)\\
&\approx -\log\left(\langle 0|e^{-HT}|0\rangle\right) - \sum_{\delta Q\neq 0}\frac{\langle\delta Q|e^{-HT}|0\rangle}{\langle 0|e^{-HT}|0\rangle}e^{i\pi q\delta Q/n} + \frac{1}{2}\left(\sum_{\delta Q\neq 0}\frac{\langle\delta Q|e^{-HT}|0\rangle}{\langle 0|e^{-HT}|0\rangle}e^{i\pi q\delta Q/n}\right)^2\\
&\approx -\frac{\langle 1|e^{-HT}|0\rangle}{\langle 0|e^{-HT}|0\rangle}e^{i\pi q/n} - \left[\frac{\langle 2|e^{-HT}|0\rangle}{\langle 0|e^{-HT}|0\rangle} - \frac{1}{2}\left(\frac{\langle 1|e^{-HT}|0\rangle}{\langle 0|e^{-HT}|0\rangle}\right)^2\right]e^{2i\pi q/n} + \text{c.c.} + \text{cte.}
\end{aligned} \tag{4.59}$$

where "c.c." means complex conjugate. We consider the energy up to $\mathcal{O}(e^{-2S_0})$, which means we neglect the transitions with $\delta Q > 2$. Since we are interested only on the energy splitting between different ground states, we gather all constant terms in "cte." and we will ignore it from now on. Comparing with Eqs. (4.35) and (4.39), we can easily compute $\langle 0|e^{-HT}|0\rangle \approx \mathcal{N}e^{-\omega T/2}$, such that we can express in terms of the Monte Carlo transition rates, $G^{1(2)}_{\text{MC}}$,

$$E(q) \approx -e^{\frac{i\pi q}{n}}\frac{G^1_{\text{MC}}}{\mathcal{N}_{\text{MC}}} + e^{\frac{2i\pi q}{n}}\left[\frac{-G^2_{\text{MC}}}{\mathcal{N}_{\text{MC}}} + \frac{1}{2}\left(\frac{G^1_{\text{MC}}}{\mathcal{N}_{\text{MC}}}\right)^2\right] + \text{c.c.}. \tag{4.60}$$

The energy splitting is plotted in Fig. 4.5(b) for $L = 12$ and shows a good agreement

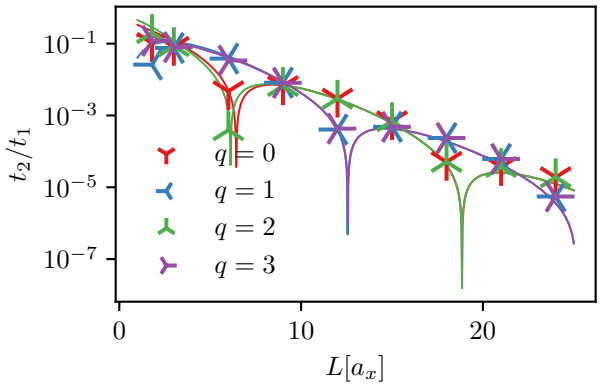

Figure 4.6: $|E(q)|$ as function of length for $\mu = 0.5$ with the same color scheme as Fig. 4.5. Note that for $L < 6$ is possible to clearly observe an asymmetry between $q = 0$ and 2 sectors.

between simulation and theory. We isolate the subleading contributions in Fig. 4.5(c), which demonstrates that the corrections

$$\Delta E(q) = e^{\frac{2i\pi q}{n}} \left[\frac{-G^2_{\mathrm{MC}}}{\mathcal{N}_{\mathrm{MC}}} + \frac{1}{2} \left(\frac{G^1_{\mathrm{MC}}}{\mathcal{N}_{\mathrm{MC}}} \right)^2 \right] + \text{c.c}, \tag{4.61}$$

are two orders of magnitude lower than $E(q)$ for the chosen parameters, but still in very good agreement with the theory. The bi-instanton corrections are more visible when we consider $E(q)$ as function of length for a fixed chemical potential, see Fig. 4.6 for $\mu = 0.5$. According to the theory, the level crossing between $q = 0$ and $q = 2$ at $L \approx 6$ is shifted, which we confirm by the simulations. For small lengths, the semi-classical approximation does not fully capture the behavior of the system and we see differences between analytical results and Monte Carlo simulations. Even so, it is still possible to find regions in which the semi-classical regime describes bi-instantons and the effects are not negligible.

We estimate that the subleading correction due to four-parafermion interaction can be on the order of 10% of the leading contribution. Indeed, using typical experimental values for the FQH edges [94, 112, 142], we can estimate $v = 10^5 \mathrm{m/s}$, $E_{\mathrm{cutoff}} \sim 2\,\mathrm{meV}$ the bulk gap of FQH, $L \sim \mu m$ and $\Delta \sim 1\,\mathrm{meV}$, from which we find that the correction is on the order of $0.1 \sim 10\%$ as shown in Fig. 4.7.

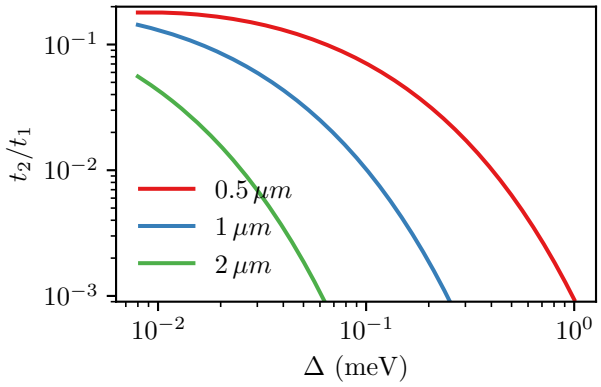

Figure 4.7: Ratio between energy correction due one and two instantons, Eq. (4.40) and (4.53), for typical experimental value $v = 10^5$m/s, $E_{\text{cutoff}} = 2\,\text{meV}$ and different lengths L over a range of superconducting gap Δ.

Chapter 5

Conclusions and outlook

In this thesis, we investigated different aspects of parafermion modes. From fermionic lattice models to fractional quantum Hall models, we explored different aspects of parafermions that can be used as smoking gun signatures in experiments. Below, we give a short summary of each chapter's result. At the end we give an outlook with the future directions we hope to explore.

Summary of the main results of chapter 2, "Quantum dots as Parafermion detectors"

In this chapter, we proposed that quantum dots can be useful tools to probe the presence of parafermionic zero modes in strongly correlated topological systems. Local measurements of quantum dot properties such as the local density of states and the dot's occupancy can discern trivial from topological phases and even tell different topological phases apart from each other.

We illustrated this by considering a model of a quantum dot coupled to strongly correlated 1D model with a topological phase displaying $\mathbb{Z}_4$ parafermionic edge zero modes [12]. Our DMRG calculations showed that the QD properties can map the phase diagram of the topological system in a one-to-one correspondence with the phase diagram obtained by tracking the ground state degeneracy and the opening and closing of energy gaps. In fact, using the QD as a probe has a clear advantage in discerning $\mathbb{Z}_4$ and $2 \times \mathbb{Z}_2$ phases from each other, as they share general features in terms of ground state degeneracy and gap sizes.

The peak height in the QD LDOS as a function of the QD onsite energy ϵ_d can be used to distinguish the two topological phases from each other and from the trivial one. The main mechanism leading to the LDOS peaks is the "leaking" of edge PZMs from the chain to the QD. This leaking is stronger for the $2 \times \mathbb{Z}_2$ phase, which resembles the case of QD-Majorana coupled systems [109, 110] and allows a clear distinction of the $\mathbb{Z}_4$ phase, which, in turn shows a strong pinning of the QD LDOS value.

In order to understand better the QD signatures of the $\mathbb{Z}_4$ phase, we calculated the first order correction to the topological ground state due to the coupling to the QD. These analytical results nicely match the DMRG numerics and confirm the presence of a parafermionic state localized in the QD site for ϵ_d values corresponding to the peaks in the LDOS.

Moreover, the dot charge occupancy $\langle n_d \rangle$ as a function of ϵ_d can also be used to differentiate the different topological phases in the system. Not only the two topological phases have distinct $\langle n_d \rangle$ vs ϵ_d curves from the trivial one but the $\mathbb{Z}_4$ phase shows a a discontinuity around $\epsilon_d = -U_d/2$, which does is not present in the trivial and $2 \times \mathbb{Z}_2$ phases.

These results indicate that quantum dots can be effectively used as parafermion detectors. Their ability to distinguish between the different phases, together with the relatively direct experimental access to the dot's local properties, bring interesting prospects in the use of QDs as a tool in the search of parafermionic zero modes.

Summary of the main results of chapter 3, "Fermionic $\mathbb{Z}_3$ parafermion"

In this chapter, we proposed a family of purely one-dimensional fermionic models which map into a Kitaev-like chain of $\mathbb{Z}_3$ parafermions. Similarly to the case of Majorana zero modes, the system has a topological phase with exponentially localized $\mathbb{Z}_3$ parafermionic modes at its ends.

A key element in the proposed models is the presence of strong, Hubbard-like, repulsive interactions of strength U_H on each site of the fermionic chain, effectively restricting the local Hilbert space to a t–J model-like basis of zero and singly occupied (spinful) fermionic states. Within this basis, an exact the mapping of the parafermion chain to a fermionic model is obtained. Even though the mapping is exact only in the $U_H \to \infty$ limit, we showed the parafermionic phase is present even for moderate values of the interaction in the range $U_H/t \gtrsim 10$.

Although this mapping produces nonphysical parity-breaking terms, we suggested that such terms can be understood as a mean-field reduction of a parity-preserving three-body interaction term. In fact, we established that this rather exotic three-body, spin-flipping interaction term is directly responsible for the existence of a $\mathbb{Z}_3$ topological phase with parafermionic edge modes. More importantly, we showed the ground state of the resulting Hamiltonian does have a well-defined parity and cannot be understood as a combination of symmetry-broken $\mathbb{Z}_2$ Majorana modes.

The existence of a topological phase in the fermionic models is strongly implied by the three-fold degenerate ground states with gapless edge states and their properties such as indistinguishability by local operators, and protection against disorder and $\mathbb{Z}_3$-symmetry-preserving impurities. In this regard, we should note that similar parafermionic modes have been referred to as "nontopological parafermions" [14] or the "poor man's

parafermion" [48] in previous studies.

Our DMRG calculations showed topological phase transitions as a function of several parameters. The phase transitions can be characterized by different metrics such as many-body gap closings and openings, changes in the ground-state degeneracy, and peaks in the entanglement entropy. These calculations confirmed the topological equivalency of the fermionic models and the parafermion chain and provide a way to probe the robustness of the topological phase against one-body terms such as on-site Zeeman field in the z direction and changes in the chemical potential. In particular, we show that an in-plane (xy) magnetic field can produce phase transitions depending on the angle θ between x and y components. This produces a threefold anisotropy in the energy gap and ground-state degeneracy with θ stemming from the expected $\mathbb{Z}_3$ symmetry of the original fermionic Hamiltonian.

Moreover, the FPF-SF confirms the exponential localization of the parafermionic modes deep in the topological regime for both H_I and H_{II} models. As the system approaches the phase transition, the FPF-SF becomes more delocalized as the edge modes located at opposite ends of the chain overlap with each other. Such finite-size effects turn out to be very relevant for small chains (less than ~ 100 sites).

Summary of the main results of chapter 4, "Overlap of parafermion bound states in Fractional Quantum Hall"

In this chapter, we have analyzed the relevance of subleading finite-size effects to the effective description of parafermion bound states existing in a pair of FQH channels with FM-SC-FM interfaces.

We derived a dilute bi-instanton gas approximation and demonstrated that the outcomes are compatible with high-order parafermion interactions in the effective model. We found a relation between the coupling parameters and the microscopic constants, which reveals that many-body parafermion interaction terms can be observed in small systems and manifest themselves in characteristic oscillations of the ground state energy level splitting as a function of chemical potential or system size.

The bi-instanton approximation is also compatible with Monte Carlo simulations. We highlight that the agreement between analytical and numerical methods indicates the existence of high-order interactions that cannot be explained by previous results. Far from being a mere hindrance, these subleading terms, which do not exist in the case of Majorana bound states, can give rise to novel phases and mechanisms that lie beyond the usual description of parafermion chains.

Outlook

Parafermion in condensed matter is still a young and exciting field in topological condensed matter. As such, it is filled with open questions about the nature of states and their properties. In the future, we want to understand better fermionic models that have a parafermionic edge state, be it topological or not. In particular, the fermionic $\mathbb{Z}_3$ parafermion model we proposed has its topological nature not wholly determined. Although heavily implied, an in-depth study using both iDMRG [120] and time-dependent methods [143] is necessary to confirm its topology and braiding. Another issue with the $\mathbb{Z}_3$ model is that the FPF-SF comes from a non-local operator (the FPF operator, d, depends on string operators). It is unclear how this local/non-local relation is associated with the "bulk-boundary condition" of usual topological systems.

To end, another system that hosts parafermion states is Kondo devices [15, 16, 144]. In this thesis, we didn't explore such systems. Current experiments have already manufactured the devices theoretically predicted to host anyons (Majorana fermion, Fibonnaci, parafermion) [145–147]. It is imperative to look more for such devices to understand better the properties of the hosted anyons and how to manipulate them.

Appendix A

A short introduction to bosonization.

In this appendix, we introduce the concept of bosonization that is used throughout the text when we need to treat fractional quantum hall systems. This appendix covers only the elementary concepts of bosonization. Bosonization is a tool with some nuances, for a detailed account see Refs. [104–106, 148–151].

Right and left moving fields

We start with a low-energy Hamiltonian defined near the Fermi point, k_F, in a 1D system,

$$H_F = \sum_k \epsilon(k) c_k^\dagger c_k. \tag{A.1}$$

In the vicinity of k_F, we can define two new annihilation operators (and their creation counterparts), α_k and β_k,

$$\begin{aligned} \alpha_k &= c_{k_F+k} \qquad \alpha_{-k} = c_{-k_F-k}, \\ \beta_k &= c^\dagger_{k_F-k} \qquad \beta_{-k} = c^\dagger_{-k_F+k}. \end{aligned} \tag{A.2}$$

Around k_F we can rewrite the Hamiltonian as integral over a region $-\Lambda$ and Λ, which implies a cutoff energy of $v_F\Lambda$, where v_F is the Fermi velocity. The non-interacting Hamiltonian takes the form

$$H_F = \int \frac{dk}{2\pi}\, v_k \left(\alpha_k^\dagger \alpha_k + \beta_k^\dagger \beta_k\right), \tag{A.3}$$

In real space, we can separate an annihilation operator in the slow right (left) moving field operators ψ_R (ψ_L)[1],

$$c_x = \psi_R(x) e^{ik_F x} + \psi_L(x) e^{-ik_F x}, \tag{A.4}$$

[1]Equation A.4 should have a factor of $1/\sqrt{a}$ with an associated to the system's dimension. To simplify we choose a length unit such that a=1 and we ignore this factor.

is easy to see that these slow-moving fields obey the following anti-commutation relations

$$\begin{aligned} \{\psi_{R(L)}(x), \psi^\dagger_{R(L)}(x')\} &= \delta(x-x'), \\ \{\psi_R(x), \psi^\dagger_L(x')\} &= 0. \end{aligned} \tag{A.5}$$

Applying a Fourier transformation, we can relate Eqs. (A.2) and (A.5),

$$\begin{aligned} \psi_R &= \textstyle\int_{k>0} \frac{dk}{2\pi}\ e^{ikx}\alpha_k + e^{-ikx}\beta^\dagger_k, \\ \psi_L &= \textstyle\int_{k<0} \frac{dk}{2\pi}\ e^{ikx}\alpha_k + e^{-ikx}\beta^\dagger_k. \end{aligned} \tag{A.6}$$

More generally, the time dependence is obtained by multiplying α and β by $e^{-iv_F|k|t}$. We can define the complex variable $z = -i(x - v_F t) = v_F\tau - ix$ and we obtain the following mode expansion,

$$\begin{aligned} \psi_R(z) &= \textstyle\int_{k>0} \frac{dk}{2\pi}\ e^{-kz}\alpha_k + e^{kz}\beta^\dagger_k, \\ \psi_L(\bar{z}) &= \textstyle\int_{k<0} \frac{dk}{2\pi}\ e^{k\bar{z}}\alpha_k + e^{-k\bar{z}}\beta^\dagger_k. \end{aligned} \tag{A.7}$$

Since positive wavevectors are separated by roughly $2k_F$ from the negative ones, the right and left moving modes are separated. Because of this, we can write two well-defined densities J_R and J_L such that the total density n_{tot} is equal to $J_R + J_L$.

$$J_R(x) = \psi^\dagger_R(x)\psi_R(x), \qquad J_L(x) = \psi^\dagger_L(x)\psi_L(x). \tag{A.8}$$

In this thesis, we are interested in the edge of two-dimensional fractional quantum Hall insulators. We can start looking into a similar model, the edge of a two-dimensional topological insulator with counter-propagating modes (and opposite spins) [106]. This system was shown to have Majorana when in close proximity to a superconductor [152]. The topological insulator's edge can be described by the time-reversal invariant Hamiltonian

$$H_F = -iv_F \int dx\ {}^*_*\psi^\dagger_R \partial_x \psi_R {}^*_* - {}^*_*\psi^\dagger_L \partial_x \psi_L {}^*_*, \tag{A.9}$$

where the ψ_R (ψ_L) have spin up (down). In order to avoid divergences, due to the introduction of infinite states (in the Dirac sea), we consider the normal ordering operator

$${}^*_*\psi^\dagger_{R(L)} \partial_x \psi_{R(L)} {}^*_* = \psi^\dagger_{R(L)} \partial_x \psi_{R(L)} - \left\langle \psi^\dagger_{R(L)} \partial_x \psi_{R(L)} \right\rangle, \tag{A.10}$$

in which we subtract the divergent expectation value that arises from the infinite Dirac sea.

Bosonic fields

The idea behind bosonization is that we can express fermionic fields in terms of bosonic ones. For that, let's take one step back and consider a simple bosonic Hamiltonian of a harmonic string,

$$H_b = \frac{v_s}{2\pi}\int dx \ \left[(\Pi(x))^2 + (\partial_x\phi(x))^2\right], \tag{A.11}$$

where v_s is the sound speed, and the operators are $\partial_x\phi, \Pi(x)$ are canonically conjugate. The two fields obey the following relations:

$$\begin{gathered}[\partial_x\phi(x), \Pi(x')] = i\delta(x-x') \\ [\phi(x), \phi(x')] = [\Pi(x), \Pi(x')] = 0,\end{gathered} \tag{A.12}$$

The bosonic Hamiltonian, H_b, can be diagonalized using normal bosonic modes b_p, with p the wave vector $p = 2\pi n/L$ ($n \in \mathbb{Z}$) and L the system length. The b operators satisfy the usual bosnic commutation relation $[b_p, b^\dagger_{p'}] = \delta_{p,p'}$. In this basis, the diagonalized Hamiltonian becomes $H_b = v_s\sum_p |p| b^\dagger_p b_p$. Defining a new field $\theta(x)$, such that $\partial_x\theta(x) = \pi\Pi(x)$, we can find the change of basis that diagonalizes H_b,

$$\begin{aligned}\phi(x) &= -\frac{i\pi}{L}\sum_{p\neq 0}\sqrt{\frac{L|p|}{2\pi}}\frac{1}{p}e^{-\alpha|p|/2}e^{-ipx}(b^\dagger_p + b_{-p}), \\ \theta(x) &= \frac{i\pi}{L}\sum_{p\neq 0}\sqrt{\frac{L|p|}{2\pi}}\frac{1}{|p|}e^{-\alpha|p|/2}e^{-ipx}(b^\dagger_p - b_{-p}),\end{aligned} \tag{A.13}$$

where α introduces a finite bandwidth $\Lambda \sim 1/\alpha^2$. Using the bosonic relations, we find

$$\begin{aligned}[\phi(x), \theta(x')] &= \sum_{p\neq 0}\frac{\pi}{Lp}e^{ip(x'-x)-\alpha|p|} \xrightarrow[\alpha\to 0]{L\to\infty} i\int_0^\infty \frac{dp}{p}\sin(p(x'-x)) \\ &= \frac{i\pi}{2}sgn(x'-x).\end{aligned} \tag{A.14}$$

We can define chiral right/left fields, $\varphi_R = \phi - \theta$ and $-\varphi_L = \phi + \theta$. The Heisenberg equations of motion $\partial_t\varphi_{L/R} = i[H_b, \varphi_{L/R}]$, shows that indeed the fields propagate in only one direction.

Now we can introduce the bosonization map between chiral fermionic and chiral

[2]To be precise, it should be considered the limit $\alpha \to 0$, such that we could recover all fermionic anti-commutation relation [104]. Non-zero α, as done in bosonization, introduces a characteristic length in which bosonization works, smaller length scales can't be described with bosonization. This in turn makes bosonization a low-energy theory.

bosonic field[3].

$$\psi_R(x) = \frac{1}{\sqrt{2\pi\alpha}} e^{-i(\phi(x)-\theta(x))}, \qquad \psi_L(x) = \frac{1}{\sqrt{2\pi\alpha}} e^{i(\phi(x)+\theta(x))} \tag{A.15}$$

Here, we omitted Klein factors, operators that connect various N-particle Hilbert spaces, i.e. "ladder operators" which can't be done with only bosonic operators, see Ref [148], and are important for the anti-commutation relations ψ_a, ψ_b=0 and $\psi_L, \psi_R^\dagger = 0$. Normally these operators are simple modifications and do not evolve in time.

To conclude, we can use Eq. (A.15) with the Hamiltonian H_F, Eq. (A.9), to find its bosonized form[4] [106],

$$H_F = \frac{v_F}{2\pi} \int dx \, {}^*_*[\partial_x \theta(x)]^2 {}^*_* + {}^*_*[\partial_x \phi(x)]^2 {}^*_*, \tag{A.16}$$

which is the same as H_b, as long as we identify the Fermi velocity (v_F) with the sound velocity (v_s).

[3]For the proof, see Refs. [104, 148].

[4]It is necessary to take into account the bosonic normal ordering, see Ref. [106]

Appendix B

First-order approximation.

In this appendix, we provide an analytical approach to calculate the first-order correction to the ground state of the $\mathbb{Z}_4$ phase in the presence of the quantum dot.

The starting point is writing the (four-fold degenerate) ground state $|g_j^{(0)}\rangle$ of $H_{\rm pf}$ as $\mathbb{Z}_4$ Fock-parafermion (FPF) states $\{|\,|j\rangle_{pf}\}$, where j is the total FPF number ranging from 0 to 3 [11, 88]. Notice that one can always write these FPF number basis states in terms of (spinful) fermionic operators acting on a vacuum state $|0\rangle$, which corresponds to $k=0$ FPFs [12]. For instance, for the QD FPF states, we choose $|k=1\rangle_d = c^\dagger_{\uparrow,d}|0\rangle_d$, $|k=2\rangle_d = ic^\dagger_{\uparrow,d}c^\dagger_{\downarrow,d}|0\rangle_d$, $|k=3\rangle_d = -ic^\dagger_{\downarrow,d}|0\rangle_d$.

Next, we construct a basis for $H^{(0)} \equiv H_{\rm pf} + H_{\rm QD}$ in the form $|k\rangle_d \otimes |g_j^{(0)}\rangle$ where $|k\rangle_d$ are Fock parafermion states with FPF number k acting on the QD Hilbert space. This gives 16-state basis denoted by $|k\rangle_d \otimes |g_j^{(0)}\rangle$, where k and j are the total FPF number ranging from 0 to 3 each. To simplify the notation we call $|k\rangle_d \otimes |g_j^{(0)}\rangle \equiv |k,j\rangle$.

The ground state $|g_j^{(0)}\rangle$ of a L site chain is written as a single FPF $|f_a\rangle$ together with a $L-1$ site chain $|s_{j-a}^{(L-1)}\rangle$ with total FPF number $j-a$ mod 4,

$$|g_j^{(0)}\rangle = \frac{1}{2}\left(|f_0\rangle \otimes |s_j^{(L-1)}\rangle + |f_1\rangle \otimes |s_{j-1}^{(L-1)}\rangle + |f_2\rangle \otimes |s_{j-2}^{(L-1)}\rangle + |f_3\rangle \otimes |s_{j-3}^{(L-1)}\rangle\right). \quad \text{(B.1)}$$

We also use as a general notation $|n+(k-m)\rangle_d = {d_d^\dagger}^n d_d^m |k\rangle_d$ where $d(d^\dagger)$ is the annihilation (creation) FPF operator that lowers (rises) the FPF number by one [1]. If $k-m<0$ or $n+k-m>3$, this state should be understood as zero. For a parafermion chain the condition $k-m<0$ or $n+k-m>3$ is not valid, since the ground state with total FPF number j is a sum of all FPF states at the first site, Eq. (B.1). Instead, we have a filter function $\eta_n = (4-n)/4$ that arise from applying a FPF operator at the first site of the parafermion chain

$$\langle g^{(0)}_{n+(j-m)}|\, {d_1^\dagger}^n d_1^m\, |g_j^{(0)}\rangle = \frac{4-\max(n,m)}{4}. \quad \text{(B.2)}$$

[1] In terms of fermionic operators they can be written as $d_l = i^{\sum_{p<l}(n_{\downarrow,p}+3n_{\uparrow,p}-2n_{\uparrow,p}n_{\downarrow,p})}c_{\uparrow,l}(1-n_{\downarrow,l}) - c^\dagger_{\uparrow,l}n_{\downarrow,l} + ic^\dagger_{\downarrow,l}n_{\uparrow,l}$ [12].

Now, we consider fermionic operators in terms of Fock-parafermions at a given site l:

$$c_{\uparrow,l} = i^{\sum_{p<l} -N_p+2n_{\uparrow,p}+2n_{\downarrow,p}} \left(d_l - d_l^\dagger d_l^2 - (-1)^{\sum_{p<l} N_p} d_l^{\dagger 3} d_l^2 \right), \tag{B.3}$$

$$c_{\downarrow,l} = i^{\sum_{p<l} -N_p+2n_{\uparrow,p}+2n_{\downarrow,p}} (-i) \left((-1)^{\sum_{p<l} N_p} d_l^3 + d_l^\dagger d_l^2 - d_l^{\dagger 2} d_l^3 \right), \tag{B.4}$$

where N_p is the FPF number operator. Notice the string-like phases appearing in the fermionic operators, which is zero for dot operators ($l=0$). To simplify the notation, the string-phase resulting from $c_{\sigma,1}\,|k,j\rangle$ (which depends on the dot occupation and the FPF number) is denoted as φ_k with $\varphi_0=1, \varphi_1=i, \varphi_2=-1$ and $\varphi_3=-i$.

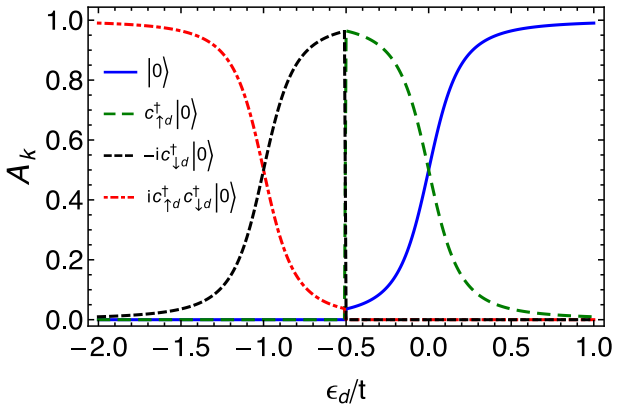

Figure B.1: Calculated ground state components $A_k \equiv \sum_j |\langle k,j|g^{(1)}\rangle|^2$ for each state of the lowest energy doublet in $|g^{(1)}\rangle$ at the dot site. The crossings at $\epsilon_d = -U_d, 0$ mark the points where the ground state has equal weights of two FPF states, indicating PZMs localized in the dot. At the symmetric point, $\epsilon_d = -U_d/2$, the ground state doublet changes, resulting in a discontinuity in A_k.

The next step is to consider the correction to the coupling to the quantum dot $H^{(1)} \equiv H_{\text{pf}-\text{QD}}$ given by Eqs. (2.6) by calculating its matrix elements in the FPF basis $\{|k,j\rangle\}$. After some straightforward algebra, we can derive the Hamiltonian elements we need, namely:

$$\begin{aligned}
c^\dagger_{\uparrow,d} c^\dagger_{\uparrow,1}\,|k,j\rangle = \varphi_k \,[&\eta_1\,|k{+}1,j{-}1\rangle - \eta_2\,|k{+}1,1{+}(j{-}2)\rangle - \\
&-\varphi_k^2\eta_3\,|k{+}1,3{+}(j-2)\rangle - \eta_1\,|2{+}(k-1),j{-}1\rangle + \\
&+\eta_2\,|2{+}(k{-}1),1{+}(j{-}2)\rangle + \varphi_k^2\eta_3\,|2{+}(k{-}1),3{+}(j{-}2)\rangle - \\
&-\eta_1\,|2{+}(k{-}3),j{-}1\rangle + \eta_2\,|2{+}(k{-}3),1{+}(j{-}2)\rangle + \\
&+\varphi_k^2\eta_3\,|2{+}(k{-}3),3{+}(j{-}2)\rangle\big]\,,
\end{aligned} \tag{B.5}$$

$$
\begin{aligned}
c^{\dagger}_{\downarrow,d}c_{\downarrow,1}\left|k,j\right\rangle = \varphi_k\big[&\varphi_k^2\eta_3\left|k{+}3,j{-}3\right\rangle+\eta_2\left|k{+}3,1{+}(j{-}2)\right\rangle-\\
&-\eta_3\left|k{+}3,2{+}(j{-}3)\right\rangle+\varphi_k^2\eta_3\left|2{+}(k{-}1),j{-}3\right\rangle+\\
&+\eta_2\left|2{+}(k{-}1),1{+}(j{-}2)\right\rangle-\eta_3\left|2{+}(k{-}1),2{+}(j{-}3)\right\rangle-\\
&-\varphi_k^2\eta_3\left|3{+}(k{-}2),j{-}3\right\rangle-\eta_2\left|3{+}(k{-}2),1{+}(j{-}2)\right\rangle+\\
&+\eta_3\left|3{+}(k{-}2),2{+}(j{-}3)\right\rangle\big]\ ,
\end{aligned}
\tag{B.6}
$$

$$
\begin{aligned}
c^{\dagger}_{\uparrow,d}c^{\dagger}_{\uparrow,1}\left|k,j\right\rangle = \varphi_k^3\big[&\eta_1\left|k{+}1,j{+}1\right\rangle-\eta_2\left|k{+}1,2{+}(j{-}1)\right\rangle-\\
&-\varphi_k^2\eta_3\left|k{+}1,2{+}(j{-}3)\right\rangle-\eta_1\left|2{+}(k{-}1),j{+}1\right\rangle+\\
&+\eta_2\left|2{+}(k{-}1),2{+}(j{-}1)\right\rangle+\varphi_k^2\eta_3\left|2{+}(k{-}1),2{+}(j{-}3)\right\rangle-\\
&-\eta_1\left|2{+}(k{-}3),j{+}1\right\rangle+\eta_2\left|2{+}(k{-}3),2{+}(j{-}1)\right\rangle+\\
&+\varphi_k^2\eta_3\left|2{+}(k{-}3),2{+}(j{-}3)\right\rangle\big]\ ,
\end{aligned}
\tag{B.7}
$$

$$
\begin{aligned}
c^{\dagger}_{\downarrow,d}c^{\dagger}_{\downarrow,1}\left|k,j\right\rangle = \varphi_k^3\big[&\varphi_k^2\eta_3\left|k{+}3,j{+}3\right\rangle+\eta_2\left|k{+}3,2{+}(j{-}1)\right\rangle-\\
&-\eta_3\left|k{+}3,3{+}(j{-}2)\right\rangle+\varphi_k^2\eta_3\left|2{+}(k{-}1),j{+}3\right\rangle+\\
&+\eta_2\left|2{+}(k{-}1),2{+}(j{-}1)\right\rangle-\eta_3\left|2{+}(k{-}1),3{+}(j{-}2)\right\rangle-\\
&-\varphi_k^2\eta_3\left|3{+}(k{-}2),j{+}3\right\rangle-\eta_2\left|3{+}(k{-}2),2{+}(j{-}1)\right\rangle+\\
&+\eta_3\left|3{+}(k{-}2),3{+}(j{-}2)\right\rangle\big]\ .
\end{aligned}
\tag{B.8}
$$

We can also derive the diagonal terms in $H^{(0)}$ involving dot operators, which we write schematically as

$$
(n_{\uparrow,d}+n_{\downarrow,d})\left|k,j\right\rangle = \left|1{+}(k{-}1),j\right\rangle+\left|2{+}(k{-}2),j\right\rangle-\left|3{+}(k{-}3),j\right\rangle\ , \tag{B.9}
$$

$$
n_{\uparrow,d}n_{\downarrow,d}\left|k,j\right\rangle = \left|2{+}(k{-}2),j\right\rangle-\left|3{+}(k{-}3),j\right\rangle\ . \tag{B.10}
$$

The corrected ground state $\{|g^{(1)}\rangle\}$ are the eigenvectors associated with the four-lowest eigenvalues of $H^{(0)}+H^{(1)}$ in the $\{|k,j\rangle\}$ FPF basis. These $|g^{(1)}\rangle$ states are divided in two doublets, with energy splitting less than t_d/t. Each doublet are composed of two dot FPF states (either $|0\rangle_d, c^{\dagger}_{d\uparrow}|0\rangle_d$ or $ic^{\dagger}_{d\uparrow}c^{\dagger}_{d\downarrow}|0\rangle_d, -ic^{\dagger}_{\downarrow}|0\rangle_d$) together with a sum of all states in the chain.

The resulting corrected states are then used in Eq. (2.8) to obtain an approximation for the dot LDOS $\tilde{\rho}_d(0)$, where we sum over the doublets with lowest energy. In general, this means we sum over only one doublet. Nonetheless, as shown in Fig. 2.6, the total LDOS obtained by the approximation nicely matches the one calculated from DMRG. This is valid even when the dot's interaction is large, showing the approximation' stability. The main artifact of the approximation is that, due to the doublet splitting, it yields a spin-

polarized LDOS, while DMRG gives the correct unpolarized LDOS.

The origin of the artifact is illustrated in Fig. B.1, which shows the components $A_k \equiv \sum_j |\langle k, j|g^{(1)}\rangle|^2$ of each state inside the ground state doublet as a function of ϵ_d. For $\epsilon_d < -U_d/2$ the doublet with non-zero spectral weights is spin down polarized while for $\epsilon_d > U_d/2$ the spin up polarization prevails.

Interestingly, Fig. B.1 shows that the components of states inside the doublet are equal precisely at $\epsilon_d = 0$ and $\epsilon_d = -U_d$. At these points, the state in the dot corresponds to a parafermionic mode fully localized at the quantum dot. Moving away from those points, the parafermion becomes split between dot and chain, that translates into an imbalance of spectral weights.

Appendix C

$\mathbb{Z}_3$ Fermionization

In this appendix, we derive the map between $\mathbb{Z}_3$ parafermion space and $t-J$ space. We use a similar construct done for $\mathbb{Z}_4$ parafermion [12]. We also stress that the map we use is *non-local* and therefore at first sight is not clear if it would preserve the topological phase, see for instance the Jordan-Wigner transformation of Ising model (non topological) to Kitaev chain (topological). This is explored in depth in Chapter 3.

Even though the model we derive in this appendix is fermionic, due to its properties, it cannot be analyzed using standard zero-energy spectral function. To solve this issue, we derive a Fock-parafermion spectral function for a general case.

Fermionization

In order to find a representation of the parafermionic Hamiltonian Eq. (3.6), $H_{pf} = -J\sum_{j=1}^{L-1}\psi_j\chi_{j+1}^\dagger + \text{H.c.}$, and its dangling parafermions in terms of fermionic operators, it is useful to consider FPF operators [11, 12]. These operators act in the space of states with a well-defined Fock-parafermion number, as described in the introduction for the $\mathbb{Z}_n$ case. Each parafermion can be described in terms of creation ($d^\dagger$) or annihilation (d) operators, which, respectively, increase and decrease the FPF number, as:

$$\psi_j = \ d_j\omega^{N_j} + d_j^{\dagger 2}, \qquad\qquad \chi_j = \ d_j + d_j^{\dagger 2}, \tag{C.1}$$

where $N_j = d_j^\dagger d_j + d_j^{\dagger 2}d_j^2$ is the number of FPFs and can be either 0, 1 or 2. Because of Eq. (C.1), FPF operators must satisfy relations similar to parafermions [11];

$$\begin{gathered} d_j d_l = \omega\ d_l d_j, \quad d_j d_l^\dagger = \omega\ d_l^\dagger d_j, \quad \text{for } l<j \\ d^3 = d^{\dagger 3} = 0 \\ d_j^{\dagger m}d_j^m + d_j^{3-m}d_j^{\dagger 3-m} = 1 \quad \text{for } m = 1,2 \end{gathered} \tag{C.2}$$

In order to represent operator d in a fermionic representation, we choose a mapping

between FPF number and fermionic number basis such that each state in the t–J fermionic basis [116] ($|\mathrm{E}\rangle, \tilde{c}^\dagger_\uparrow|\mathrm{E}\rangle$, and $\tilde{c}^\dagger_\downarrow|\mathrm{E}\rangle$, with $|\mathrm{E}\rangle$ a vacuum state) corresponds to one state in the FPF number basis ($|0\rangle, |1\rangle, |2\rangle$). This mapping can be summarized as

$$\begin{gathered} |2\rangle \xrightarrow{d} |1\rangle \xrightarrow{d} |0\rangle \xrightarrow{d} \emptyset \\ \tilde{c}^\dagger_\downarrow|\mathrm{E}\rangle \xrightarrow{d} \tilde{c}^\dagger_\uparrow|\mathrm{E}\rangle \xrightarrow{d} |\mathrm{E}\rangle \xrightarrow{d} \emptyset. \end{gathered} \tag{C.3}$$

With this in mind, it is straightforward to a find a representation of FPF operators, $d = \tilde{c}_\uparrow + \tilde{c}^\dagger_\uparrow \tilde{c}_\downarrow$. It is also easy to see that Eq (C.3) satisfies all FPF operator relations. However, since the FPF operators operate in real space (sites in a chain), we need to consider Jordan-Wigner (JW) string factors for both FPF operators and fermionic operators [11, 12]:

$$d_j = \omega^{\sum_{p<j} N_p} \left[(-1)^{\sum_{p<j} n_p} \tilde{c}_{\uparrow,j} + \tilde{c}^\dagger_{\uparrow,j} \tilde{c}_{\downarrow,j} \right], \tag{C.4}$$

$$d_j^2 = \omega^{\sum_{p<j} 2N_p} \left[(-1)^{\sum_{p<j} n_p} \tilde{c}_{\downarrow,j} \right], \tag{C.5}$$

where n_p is the occupation number (0 or 1) of site p and $N_p = n_{\uparrow,p} + 2n_{\downarrow,p}$.

An important consequence of these strings is that FPF operators have two distinct long-range behaviors, namely (i) a JW-like string which depends on the FPF number N_p applied uniformly to terms and (ii) a JW string which depends on the fermionic occupation n_p applied only on single fermion operators. This is more distinct than in the case of $\mathbb{Z}_4$ parafermions where all terms have the same parity and string factor [1]. This means that, apart from the expected Jordan-Wigner string, the Hamiltonian is local in the FPF space (although nonlocal in the fermionic basis), allowing one to derive local quantities that identify the edge states.

The parafermion operators χ_j and ψ_j can be easily written in terms of the usual fermionic operators as

$$\begin{aligned} \chi_j &= \omega^{\sum_{p<j} N_p} \left[(-1)^{\sum_{p<j} n_p} [\tilde{c}_{\uparrow,j} + \tilde{c}^\dagger_{\downarrow,j}] + \tilde{c}^\dagger_{\uparrow,j} \tilde{c}_{\downarrow,j} \right], \\ \psi_j &= \omega^{\sum_{p<j} N_p} \left[(-1)^{\sum_{p<j} n_p} [\omega \tilde{c}_{\uparrow,j} + \tilde{c}^\dagger_{\downarrow,j}] + \omega^2 \tilde{c}^\dagger_{\uparrow,j} \tilde{c}_{\downarrow,j} \right]. \end{aligned} \tag{C.6}$$

[1] The problem arises in the $\mathbb{Z}_3$ case mainly because there is no single fermionic operator connecting the up and down states. By contrast, in the case of $\mathbb{Z}_4$ parafermions, two sequential FPF numbers are connected by a single fermionic operator, eliminating the problem.

In particular, we have the dangling parafermion modes written as:

$$\begin{aligned}\chi_1 =&\tilde{c}_{\uparrow,1}+\tilde{c}^\dagger_{\downarrow,1}+\tilde{c}^\dagger_{\uparrow,1}\tilde{c}_{\downarrow,1},\\ \psi_L =&\omega^{\sum_{p<L}N_p}\left[(-1)^{\sum_{p<L}n_p}[\omega\tilde{c}_{\uparrow,L}+\tilde{c}^\dagger_{\downarrow,L}]+\omega^2\tilde{c}^\dagger_{\uparrow,L}\tilde{c}_{\downarrow,L}\right].\end{aligned} \tag{C.7}$$

Notice that ψ_L contains information of the fermionic occupation in the central chain sites. This means that the edge modes are affected by the bulk states via Jordan-Wigner strings. While this also occurs in the $\mathbb{Z}_4$ case [12], the difference here is that the strings are not applied uniformly in every term, due to absence of a well-defined parity of the operators.

Using the above relations (C.6), we can express the Hamiltonian H_{pf} in terms of fermionic operators:

$$\begin{aligned}H_{pf} =& -J\sum_{j=1}^{L-1}\psi_j\chi^\dagger_{j+1}+\text{H.c.}\\ =& -J\sum_{j=1}^{L-1}\left[(-1)^{\sum_{p<j}n_p}[\tilde{c}_{\uparrow,j}-i\tilde{c}^\dagger_{\downarrow,j}]+i\tilde{c}^\dagger_{\uparrow,j}\tilde{c}_{\downarrow,j}\right]\\ &\times\left[(-1)^{\sum_{p<j+1}n_p}[\tilde{c}^\dagger_{\uparrow,j+1}+i\tilde{c}_{\downarrow,j+1}]-i\tilde{c}^\dagger_{\downarrow,j+1}\tilde{c}_{\uparrow,j+1}\right]+\text{H.c.},\end{aligned} \tag{C.8}$$

which is equal to H_{II} when $t=\Delta=W_3=W_4=J$.

FPF spectral function derivation

In this section, we show that the FPF spectral function for a $\mathbb{Z}_M$ parafermion chain with two dangling parafermions described by Eq. (3.6) is given by $\mathcal{A}_j=2\pi\frac{2}{M^2}(\delta_{1,j}+\delta_{L,j})$. In this appendix only we consider $\omega=e^{2i\pi/M}$. In this section we use a generalization of the ground state shown in Appendix D for $M\geq 2$.

We start with the FPF spectral function, defined by Eq. (3.17). We can write it as

$$\mathcal{A}_j(E')=\frac{2\pi}{N_{gs}}\sum_{|\varphi\rangle|g\rangle}\delta(E'+E_\varphi-E_0)|\langle\varphi|\,d_j\bar{\omega}^{N_j}\,|g\rangle\,|^2+\delta(E'-E_\varphi+E_0)|\langle\varphi|\,\bar{\omega}^{N_j}d_j^\dagger\,|g\rangle\,|^2, \tag{C.9}$$

where we sum over all ground states $|g\rangle$ and divide by its degeneracy n_{gs}. The state $|\varphi\rangle$ is an eigenstate of the Hamiltonian with energy E_φ. As we show later, it is important to consider $d_j\bar{\omega}^{N_j}$ [2] instead of just d_j due to symmetry of the spectral function. While the former has a symmetric zero-energy spectral function along the chain, the latter will have

[2] Another option is to consider $d_j\bar{\omega}^{N_j/2}$ which will also have a symmetric zero-energy spectral function. The biggest difference is a scaling factor and should not affect how the edge states are localized.

the zero-energy spectral function on the first site, $j=1$, $(M-1)^2$ times larger than on the last site, $j=L$.

For a generic chain with L sites, the ground state of H_{pf} for $\mathbb{Z}_M$ parafermions with total FPF number i [88], Eq. (1.27) is given by

$$|g_i^L\rangle = \frac{1}{\sqrt{M^{L-1}}} \sum_{\substack{\{N_j\} \text{ such that} \\ \sum_j N_j = i \ mod \ M}} \bigotimes_{j=1}^{L} |N_j\rangle, \tag{C.10}$$

which, in turn, can be written in terms of a chain with $L-1$ sites and a single site at one of the ends or a single site at position s and two chains with $s-1$ and $L-s$ sites:

$$|g_i\rangle = \frac{1}{\sqrt{M}} \sum_{k=0}^{M-1} |f_{i-k}\rangle \otimes |g_k^{L-1}\rangle \tag{C.11}$$

$$|g_i\rangle = \frac{1}{\sqrt{M}} \sum_{k=0}^{M-1} |g_k^{L-1}\rangle \otimes |f_{i-k}\rangle \tag{C.12}$$

$$|g_i\rangle = \frac{1}{M} \sum_{a=0}^{M-1} \sum_{k=0}^{M-1} |g_a^{s-1}\rangle \otimes |f_{i-k}\rangle \otimes |g_{-a+k}^{L-s}\rangle\,, \tag{C.13}$$

It is straightforward to see that at positions $j=1, L$ we have a sum over $M-1$ different powers of ω, and its absolute value is always 1. This leads to $|\,\langle g_{i-1}^L|\, d_j \bar{\omega}_j^N\, |g_i^L\rangle\,| = 1/M^2$. In the bulk, Eq. (C.13), we need to consider the FPF commutation relations, Eq. (C.2).

Applying d_j at $|g_i\rangle$, with j in the bulk, does not only decrease the FPF number in one but also adds a phase that depends on the FPF number that precedes it,:

$$d_j \bar{\omega}^N |g_i\rangle = \frac{1}{M} \sum_{a=0}^{M-1} \sum_{k=0}^{M-1} \omega^{a-i+k+1}\, |g_a^{j-1}\rangle \otimes d\, |f_{i-k}\rangle \otimes |g_{-a+k}^{L-j}\rangle\,, \tag{C.14}$$

such that $\langle g_{i-1}|\, d_j \bar{\omega}^{N_j}\, |g_i\rangle \propto \sum_{a=0}^{M-1} e^{2\pi i a/M} = 0$. The same procedure can be done for $\bar{\omega}_j^N d_j^\dagger$ and yields the same result. Therefore, the spectral function, at zero energy, of a $\mathbb{Z}_M$ parafermion chain is given by

$$\begin{aligned} \mathcal{A} = \frac{2\pi}{N_{gs}} \sum_{|\varphi\rangle |g\rangle} |\,\langle\varphi|\, d_j \bar{\omega}^{N_j}\, |g\rangle\,|^2 + |\,\langle\varphi|\, \bar{\omega}^{N_j} d_j^\dagger\, |g\rangle\,|^2, \\ = 2\pi \frac{2}{M^2} \left(\delta_{1,j} + \delta_{L,j}\right) \end{aligned} \tag{C.15}$$

We also note that using only d_j instead of $d_j \bar{\omega}^{N_j}$ leads to an asymmetry between sites 1 and L which does not make sense in terms of how the parafermions are localized. This fact is unrelated with the fermionic basis (and its long-range interaction) and happens in "pure" parafermion models [88]. In addition, the phase factor $\bar{\omega}_j^N$ is not unique. A factor

such as $\omega^{N_j/2}$ would also work, albeit it introduces an additional scale factor related with the parafermion chain length. Other powers of ω_j^N might also work but they are not universal, i.e., they would depend on the value of M of the $\mathbb{Z}_M$ parafermion.

Appendix D

Mean-field derivation

In this appendix, we use mean-field arguments to obtain the Hamiltonian H_{II}, Eq. (3.7), of Chapter 3 starting from H_I, Eq. (3.4). The arguments illustrated here can be used to generate a family of Hamiltonians with H_I the "parent" Hamiltonian. The calculations, below, bear some resemblance to the s-wave BCS theory in which we substitute the expectation value $\langle c^\dagger_\uparrow(x)c^\dagger_\downarrow(x)\rangle \to \Delta(x)$, without calculating the function $\Delta(x)$ selfconsistently. Here, however, we substitute the expectation value of a string operator to the proper operator.

We start with the spin-up terms in Eq. (3.4):

$$\begin{aligned}\tilde{c}^\dagger_{\uparrow,i-1}\tilde{c}_{\downarrow,i-1}\tilde{c}^\dagger_{\uparrow,i}\tilde{c}_{\downarrow,i}\tilde{c}^\dagger_{\uparrow,i+1}\tilde{c}_{\downarrow,i+1} \approx \\ \langle\tilde{c}^\dagger_{\uparrow,i-1}\tilde{c}_{\downarrow,i-1}\tilde{c}^\dagger_{\uparrow,i}\rangle\tilde{c}_{\downarrow,i}\tilde{c}^\dagger_{\uparrow,i+1}\tilde{c}_{\downarrow,i+1} + \langle\tilde{c}^\dagger_{\uparrow,i-1}\tilde{c}_{\downarrow,i-1}\tilde{c}_{\downarrow,i}\rangle\tilde{c}^\dagger_{\uparrow,i}\tilde{c}^\dagger_{\uparrow,i+1}\tilde{c}_{\downarrow,i+1} + \\ \tilde{c}^\dagger_{\uparrow,i-1}\tilde{c}_{\downarrow,i-1}\tilde{c}^\dagger_{\uparrow,i}\langle\tilde{c}_{\downarrow,i}\tilde{c}^\dagger_{\uparrow,i+1}\tilde{c}_{\downarrow,i+1}\rangle + \tilde{c}^\dagger_{\uparrow,i-1}\tilde{c}_{\downarrow,i-1}\tilde{c}_{\downarrow,i}\langle\tilde{c}^\dagger_{\uparrow,i}\tilde{c}^\dagger_{\uparrow,i+1}\tilde{c}_{\downarrow,i+1}\rangle\end{aligned} \tag{D.1}$$

where we use the commutation relation $[\tilde{c}^\dagger_{\uparrow,i},\tilde{c}_{\downarrow,j}]=\delta_{i,j}\tilde{c}^\dagger_{\uparrow,i}\tilde{c}_{\downarrow,i}$ arising from the $t-J$ model requirement of exclusion of double occupancy states.

Assuming a spatially isotropic and $SU(2)$-symmetric spin, the expectation values in Eq. (D.1) should be proportional to $(-1)^{\sum_{p<i}n_p}$. Indeed this can be seen by calculating the expectation value $\langle\tilde{c}^\dagger_{\uparrow,i-1}\tilde{c}_{\downarrow,i-1}\tilde{c}^\dagger_{\uparrow,i}\rangle$ for the ground state of H_{II} in the case of $t=\Delta=W_3=W_4$ (when it is mapped exactly to H_{pf}). In order to compute the trifermion expectation value, we go to the Fock-parafermion basis:

$$\langle\tilde{c}^\dagger_{\uparrow,j-1}\tilde{c}_{\downarrow,j-1}\tilde{c}^\dagger_{\uparrow,j}\rangle=\langle(-1)^{\sum_{p<j}n_p}d^\dagger_{j-1}d^2_{j-1}\omega^{N_j}d_jd^{\dagger 2}_j\rangle, \tag{D.2}$$

and since we are at zero temperature, the expectation value will be the average over the ground states. We can check if this expectation value can be different from zero by considering the $\mathbb{Z}_3$ parafermion ground state of H_{pf} with L sites and total Fock-

parafermion number i given by [88]

$$|g_i^L\rangle = \frac{1}{\sqrt{3^{L-1}}} \sum_{\substack{\{N_j\} \text{ such that} \\ \sum_j N_j = i \ mod\ 3}} \bigotimes_{j=1}^{L} |N_j\rangle, \tag{D.3}$$

which, in turn, can be written in terms of a chain with $L-2$ sites and two sites at one of the ends or two sites at position s and $s+1$ together with two chains with $s-2$ and $L-s-1$ sites:

$$\begin{aligned} |g_i\rangle &= \frac{1}{\sqrt{3}} \sum_{k=0}^{2} \sum_{l=0}^{2} |f_{i-k}\rangle \otimes |f_{k-l}\rangle \otimes |g_l^{L-2}\rangle \\ |g_i\rangle &= \frac{1}{\sqrt{3}} \sum_{k=0}^{2} \sum_{l=0}^{2} |g_l^{L-2}\rangle \otimes |f_{i-k}\rangle \otimes |f_{k-l}\rangle \\ |g_i\rangle &= \frac{1}{3} \sum_{a=0}^{2} \sum_{k=0}^{2} \sum_{l=0}^{2} |g_a^{s-2}\rangle \otimes |f_{i-k}\rangle \otimes |f_{k-l}\rangle \otimes |g_{-a+l}^{L-s}\rangle , \end{aligned} \tag{D.4}$$

where $|f_i\rangle$ is the state of a single site with FPF number f_i, such that $\langle f_j| d^k |f_i\rangle = \delta_{j,i-k}$ for $k \leq i$ and zero otherwise. When we apply $d_{j-1}^\dagger d_{j-1}^2 \omega^{N_j} d_j d_j^{\dagger 2}$ on $|g_i\rangle$ the only nonzero terms are sums with $i-k=2$ and $k-l=0$. Because of the structure of the ground state we can compute the expectation value of Eq. (D.2):

$$\begin{aligned} &\langle g_i| (-1)^{\sum_{p<j} n_p} d_{j-1}^\dagger d_{j-1}^2 \omega^{N_j} d_j d_j^{\dagger 2} |g_i\rangle \\ =&\frac{1}{9} \sum_{a,k,l} \langle g_a^{j-2}| (-1)^{\sum_{p<j-1} n_p} |g_a^{j-2}\rangle \langle f_{i-k}| d^\dagger d^2 (-1)^n |f_2\rangle \langle f_{k-l}| \omega^N d d^{\dagger 2} |0\rangle \\ =&-\frac{\omega}{9} \sum_a \langle g_a^{j-2}| (-1)^{\sum_{p<j-1} n_p} |g_a^{j-2}\rangle = \frac{\omega(-1)^{j-1}}{3^j} \end{aligned} \tag{D.5}$$

where we used Eq. (D.3) to calculate the sum of the string factors,

$$\sum_a \langle g_a^{j-2}| (-1)^{\sum_{p<j-1} n_p} |g_a^{j-2}\rangle = (-1/3)^{j-2}. \tag{D.6}$$

This means that this correlation decays away from the first site $j=1$. This does not imply that there is no parafermion in H_I as we consider only one way of pairing the operators. To recover the expression of H_3, we need to substitute the average value of the string by its operator, $\langle (-1)^{\sum_{p<j} n_p} \rangle \to (-1)^{\sum_{p<j} n_p}$, and we obtain

$$H^{(6)}_{MF} = - W_{MF} \sum_{j}^{L-1} (-1)^{\sum_{p<j} n_p} \Big[(\tilde{c}_{\uparrow,j} + \tilde{c}^{\dagger}_{\downarrow,j}) \tilde{c}^{\dagger}_{\downarrow,j+1} \tilde{c}_{\uparrow,j+1} + \ \tilde{c}^{\dagger}_{\uparrow,j} \tilde{c}_{\downarrow,j} (\tilde{c}^{\dagger}_{\uparrow,j+1} + \tilde{c}_{\downarrow,j+1}) \Big] + \text{H.c.} \tag{D.7}$$

which is the similar to Equation (3.7) for an infinite chain, i.e., without edges.

Appendix E

Mathematical details of Instanton Calculation.

In this appendix, we provide some mathematical details used in the main text. We provide a rigorous definition and a step-by-step derivation of the instanton zero-mode that is important for understanding the calculations.

One instanton zero-mode

To avoid divergences in Eq. (4.35), we need to consider the zero mode of $\hat{F}$ separately[1]. We can do this, by expanding the fluctuation η in Fourier modes

$$\eta(x,\tau) = \sum_n \eta_n f_n(x,\tau) \qquad \int dx \int d\tau |f_n(x,\tau)|^2 = 1, \tag{E.1}$$

and we understand $n = (k, i\omega)$ to be the fourier transform of position and time. The eigenvalue equation is

$$[-\partial_\tau^2 - \nu^2\partial_x^2 + \frac{4\Delta\nu}{\xi}\sin(2n\phi_{sol}(\tau))]f_n(x,\tau) = \lambda_n f_n(x,\tau), \tag{E.2}$$

We can take care of the zero mode, by taking out the integral of the zero mode in the path integral measure. The zero mode equation $\hat{F}f_z = 0$ is satisfied by $\partial_t\phi_{sol}(\tau)$, therefore the space-idependent zero energy solution will be $f_z(\tau) = c\partial_t\phi_{sol}(\tau)$, for a normalization constant given by

$$\int dx \int d\tau [\partial_t\phi_{sol}(\tau)]^2 = \frac{\pi\nu S_0}{n} = \frac{1}{c^2}\int dx \int d\tau |f_z|^2 = \frac{1}{c^2}, \qquad c = \sqrt{\frac{n}{\pi\nu S_0}}. \tag{E.3}$$

[1]To simplify, we assume the instanton case $\epsilon = 1$ and we omit ϵ in the next calculation.

The zero mode corresponds to the soliton's invariance over a time translation of its center. This can be seen as

$$\begin{aligned}\phi(x,\tau) &= \phi_{sol}(\tau) + \sum_n \eta_n f_n(x,\tau) \\ &= \phi_{sol}(\tau) + \eta_z f_z(\tau) + \sum_{n\neq z} \eta_n f_n(x,\tau) \\ &= \phi_{sol}(\tau) + \sqrt{\frac{n}{\pi\nu S_0}}\eta_z \partial_\tau \phi_{sol} + \sum_{n\neq z} \eta_n f_n(x,\tau) \\ &= \phi_{sol}(\tau + \sqrt{\frac{n}{\pi\nu S_0}}\eta_z) + \sum_{n\neq z} \eta_n f_n(x,\tau) + o(\eta_z^2) \end{aligned} \tag{E.4}$$

From the soliton solution, integrating over the zero mode η_z is the same as integrating over the instanton time center τ_0, so

$$\int d\eta_z \approx \sqrt{\frac{\pi\nu S_0}{n}} \int_{-T/2}^{T/2} d\tau_0. \tag{E.5}$$

Therefore, we obtain the relation used in Eq. (4.35)

$$\int \mathcal{D}[\eta] = \mathcal{N} \int \prod_n d\eta_n = \mathcal{N}\sqrt{\frac{\pi\nu S_0}{n}} \int_{-T/2}^{T/2} d\tau_0 \int \prod_{n\neq z} d\eta_n = T\sqrt{\frac{\pi\nu S_0}{n}} \int \mathcal{D}'[\eta] \tag{E.6}$$

Bibliography

[1] A Yu Kitaev, Unpaired majorana fermions in quantum wires, Physics-Uspekhi **44**, 131 (2001).

[2] Chetan Nayak, Steven H. Simon, Ady Stern, Michael Freedman, and Sankar Das Sarma, Non-abelian anyons and topological quantum computation, Rev. Mod. Phys. **80**, 1083–1159 (2008).

[3] Ady Stern and Netanel H. Lindner, Topological quantum computation—from basic concepts to first experiments, Science **339**, 1179–1184 (2013).

[4] Sankar Das Sarma, Michael Freedman, and Chetan Nayak, Majorana zero modes and topological quantum computation, Npj Quant. Inf. **1**, 15001 EP – (2015), review Article.

[5] David Aasen, Michael Hell, Ryan V. Mishmash, Andrew Higginbotham, Jeroen Danon, Martin Leijnse, Thomas S. Jespersen, Joshua A. Folk, Charles M. Marcus, Karsten Flensberg, and Jason Alicea, Milestones toward majorana-based quantum computing, Phys. Rev. X **6**, 031016 (2016).

[6] Paul Fendley, Parafermionic edge zero modes in z n -invariant spin chains, J. Stat. Mech. **2012**, P11020 (2012).

[7] Jason Alicea and Paul Fendley, Topological phases with parafermions: Theory and blueprints, Annu. Rev. Condens. Matter Phys. **7**, 119–139 (2016).

[8] Netanel H. Lindner, Erez Berg, Gil Refael, and Ady Stern, Fractionalizing majorana fermions: Non-abelian statistics on the edges of abelian quantum hall states, Phys. Rev. X **2**, 041002 (2012).

[9] David J. Clarke, Jason Alicea, and Kirill Shtengel, Exotic non-abelian anyons from conventional fractional quantum hall states, Nature Comm. **4**, 1348 EP – (2013), article.

[10] Abolhassan Vaezi, Superconducting analogue of the parafermion fractional quantum hall states, Phys. Rev. X **4**, 031009 (2014).

[11] Emilio Cobanera and Gerardo Ortiz, Fock parafermions and self-dual representations of the braid group, Phys. Rev. A **89**, 012328 (2014).

[12] Alessio Calzona, Tobias Meng, Maura Sassetti, and Thomas L. Schmidt, $\mathbb{Z}_4$ parafermions in one-dimensional fermionic lattices, Phys. Rev. B **98**, 201110(R) (2018).

[13] Aaron Chew, David F. Mross, and Jason Alicea, Fermionized parafermions and symmetry-enriched majorana modes, Phys. Rev. B **98**, 085143 (2018).

[14] Leonardo Mazza, Fernando Iemini, Marcello Dalmonte, and Christophe Mora, Non-topological parafermions in a one-dimensional fermionic model with even multiplet pairing, Phys. Rev. B **98**, 201109(R) (2018).

[15] D. B. Karki, Edouard Boulat, Winston Pouse, David Goldhaber-Gordon, Andrew K. Mitchell, and Christophe Mora, $\mathbb{Z}_3$ parafermion in the double charge-kondo model, arXiv 10.48550/arXiv.2210.04937 (2022).

[16] Guangjie Li, Elio J. König, and Jukka I. Väyrynen, Topological symplectic kondo effect, arXiv 10.48550/arXiv.2210.16614 (2022).

[17] Raphael L. R. C. Teixeira and Luis G. G. V. Dias da Silva, Quantum dots as parafermion detectors, Phys. Rev. Res. **3**, 033014 (2021).

[18] Raphael L. R. C. Teixeira and Luis G. G. V. Dias da Silva, Edge $\mathbb{Z}_3$ parafermions in fermionic lattices, Phys. Rev. B **105**, 195121 (2022).

[19] Raphael L. R. C. Teixeira, Andreas Haller, Roshni Singh, Amal Mathew, Edvin G. Idrisov, Luis G. G. V. Dias da Silva, and Thomas L. Schmidt, Overlap of parafermionic zero modes at a finite distance, Phys. Rev. Res. **4**, 043094 (2022).

[20] Steven R. White, Density-matrix algorithms for quantum renormalization groups, Phys. Rev. B **48**, 10345 (1993).

[21] U. Schollwöck, The density-matrix renormalization group, Rev. Mod. Phys. **77**, 259–315 (2005).

[22] Ulrich Schollwöck, The density-matrix renormalization group in the age of matrix product states, Ann. Phys. **326**, 96 – 192 (2011), january 2011 Special Issue.

[23] Önder Gül, Yuval Ronen, Si Young Lee, Hassan Shapourian, Jonathan Zauberman, Young Hee Lee, Kenji Watanabe, Takashi Taniguchi, Ashvin Vishwanath, Amir Yacoby, and Philip Kim, Andreev reflection in the fractional quantum hall state, Phys. Rev. X **12**, 021057 (2022).

[24] Frank Wilczek, Quantum mechanics of fractional-spin particles, Phys. Rev. Lett. **49**, 957–959 (1982).

[25] J. Nakamura, S. Liang, G. C. Gardner, and M. J. Manfra, Direct observation of anyonic braiding statistics, Nat. Phys. **16**, 931–936 (2020).

[26] H. Bartolomei, M. Kumar, R. Bisognin, A. Marguerite, J.-M. Berroir, E. Bocquillon, B. Plaçais, A. Cavanna, Q. Dong, U. Gennser, Y. Jin, and G. Fève, Fractional statistics in anyon collisions, Science **368**, 173–177 (2020).

[27] Roger S. K. Mong, David J. Clarke, Jason Alicea, Netanel H. Lindner, Paul Fendley, Chetan Nayak, Yuval Oreg, Ady Stern, Erez Berg, Kirill Shtengel, and Matthew P. A. Fisher, Universal topological quantum computation from a superconductor-abelian quantum hall heterostructure, Phys. Rev. X **4**, 011036 (2014).

[28] Jason Alicea, New directions in the pursuit of majorana fermions in solid state systems, Rep. Prog. Phys. **75**, 076501 (2012).

[29] Adrian Hutter and Daniel Loss, Quantum computing with parafermions, Phys. Rev. B **93**, 125105 (2016).

[30] E. M. Stoudenmire, David J. Clarke, Roger S. K. Mong, and Jason Alicea, Assembling fibonacci anyons from a $\mathbb{Z}_3$ parafermion lattice model, Phys. Rev. B **91**, 235112 (2015).

[31] Emilio Cobanera, Jascha Ulrich, and Fabian Hassler, Changing anyonic ground degeneracy with engineered gauge fields, Phys. Rev. B **94**, 125434 (2016).

[32] Eduardo H Fradkin and Leo P. Kadanoff, Disorder variables and para-fermions in two-dimensional statistical mechanics, Nucl. Phys. B **170**, 1–15 (1980).

[33] N. Read and E. Rezayi, Beyond paired quantum hall states: Parafermions and incompressible states in the first excited landau level, Phys. Rev. B **59**, 8084–8092 (1999).

[34] Jelena Klinovaja, Amir Yacoby, and Daniel Loss, Kramers pairs of majorana fermions and parafermions in fractional topological insulators, Phys. Rev. B **90**, 155447 (2014).

[35] Yahya Alavirad, David Clarke, Amit Nag, and Jay D. Sau, $\mathbb{Z}_3$ parafermionic zero modes without andreev backscattering from the 2/3 fractional quantum hall state, Phys. Rev. Lett. **119**, 217701 (2017).

[36] Solofo Groenendijk, Alessio Calzona, Hugo Tschirhart, Edvin G. Idrisov, and Thomas L. Schmidt, Parafermion braiding in fractional quantum hall edge states with a finite chemical potential, Phys. Rev. B **100**, 205424 (2019).

[37] Noam Schiller, Eyal Cornfeld, Erez Berg, and Yuval Oreg, Predicted signatures of topological superconductivity and parafermion zero modes in fractional quantum hall edges, Phys. Rev. Res. **2**, 023296 (2020).

[38] Lukasz Fidkowski and Alexei Kitaev, Topological phases of fermions in one dimension, Phys. Rev. B **83**, 075103 (2011).

[39] Xiao-Gang Wen, Symmetry-protected topological phases in noninteracting fermion systems, Phys. Rev. B **85**, 085103 (2012).

[40] Jelena Klinovaja and Daniel Loss, Parafermions in an interacting nanowire bundle, Phys. Rev. Lett. **112**, 246403 (2014).

[41] Jelena Klinovaja and Daniel Loss, Time-reversal invariant parafermions in interacting rashba nanowires, Phys. Rev. B **90**, 045118 (2014).

[42] A. Alexandradinata, N. Regnault, Chen Fang, Matthew J. Gilbert, and B. Andrei Bernevig, Parafermionic phases with symmetry breaking and topological order, Phys. Rev. B **94**, 125103 (2016).

[43] Luiz H. Santos and Taylor L. Hughes, Parafermionic wires at the interface of chiral topological states, Phys. Rev. Lett. **118**, 136801 (2017).

[44] Davide Rossini, Matteo Carrega, Marcello Calvanese Strinati, and Leonardo Mazza, Anyonic tight-binding models of parafermions and of fractionalized fermions, Phys. Rev. B **99**, 085113 (2019).

[45] Udit Khanna, Moshe Goldstein, and Yuval Gefen, Parafermions in a multilegged geometry: Towards a scalable parafermionic network, Phys. Rev. B **105**, L161101 (2022).

[46] Fan Zhang and C. L. Kane, Time-reversal-invariant Z_4 fractional josephson effect, Phys. Rev. Lett. **113**, 036401 (2014).

[47] Adam S. Jermyn, Roger S. K. Mong, Jason Alicea, and Paul Fendley, Stability of zero modes in parafermion chains, Phys. Rev. B **90**, 165106 (2014).

[48] C L Kane and Fan Zhang, The time reversal invariant fractional josephson effect, Physica Scripta **T164**, 014011 (2015).

[49] Yuval Vinkler-Aviv, Piet W. Brouwer, and Felix von Oppen, $\mathbb{Z}_4$ parafermions in an interacting quantum spin hall josephson junction coupled to an impurity spin, Phys. Rev. B **96**, 195421 (2017).

[50] C. Fleckenstein, N. Traverso Ziani, and B. Trauzettel, $\mathbb{Z}_4$ parafermions in weakly interacting superconducting constrictions at the helical edge of quantum spin hall insulators, Phys. Rev. Lett. **122**, 066801 (2019).

[51] Kyrylo Snizhko, Reinhold Egger, and Yuval Gefen, Measurement and control of a coulomb-blockaded parafermion box, Phys. Rev. B **97**, 081405(R) (2018).

[52] Katharina Laubscher, Daniel Loss, and Jelena Klinovaja, Majorana and parafermion corner states from two coupled sheets of bilayer graphene, Phys. Rev. Res. **2**, 013330 (2020).

[53] Ettore Majorana, Teoria simmetrica dell'elettrone e del positrone, Il Nuovo Cimento (1924-1942) **14**, 171 (1937).

[54] Samoil M. Bilenky, Neutrinos: Majorana or dirac?, Universe **6**, 10.3390/universe6090134 (2020).

[55] N. Read and Dmitry Green, Paired states of fermions in two dimensions with breaking of parity and time-reversal symmetries and the fractional quantum hall effect, Phys. Rev. B **61**, 10267–10297 (2000).

[56] N Read, Paired fractional quantum hall states and the ν=5/2 puzzle, Physica B: Cond. Matt. **298**, 121–128 (2001).

[57] V. J. Emery and S. Kivelson, Mapping of the two-channel kondo problem to a resonant-level model, Phys. Rev. B **46**, 10812–10817 (1992).

[58] P. Coleman, L. B. Ioffe, and A. M. Tsvelik, Simple formulation of the two-channel kondo model, Phys. Rev. B **52**, 6611–6627 (1995).

[59] Jason Alicea, Majorana fermions in a tunable semiconductor device, Phys. Rev. B **81**, 125318 (2010).

[60] Yuval Oreg, Gil Refael, and Felix von Oppen, Helical liquids and majorana bound states in quantum wires, Phys. Rev. Lett. **105**, 177002 (2010).

[61] Roman M. Lutchyn, Jay D. Sau, and S. Das Sarma, Majorana fermions and a topological phase transition in semiconductor-superconductor heterostructures, Phys. Rev. Lett. **105**, 077001 (2010).

[62] Tudor D. Stanescu, Roman M. Lutchyn, and S. Das Sarma, Majorana fermions in semiconductor nanowires, Phys. Rev. B **84**, 144522 (2011).

[63] V. Mourik, K. Zuo, S. M. Frolov, S. R. Plissard, E. P. A. M. Bakkers, and L. P. Kouwenhoven, Signatures of majorana fermions in hybrid superconductor-semiconductor nanowire devices, Science **336**, 1003–1007 (2012).

[64] Stevan Nadj-Perge, Ilya K. Drozdov, Jian Li, Hua Chen, Sangjun Jeon, Jungpil Seo, Allan H. MacDonald, B. Andrei Bernevig, and Ali Yazdani, Observation of majorana fermions in ferromagnetic atomic chains on a superconductor, Science **346**, 602–607 (2014).

[65] M.-T. Deng, S. Vaitiekėnas, E. Prada, P. San-Jose, J. Nygård, P. Krogstrup, R. Aguado, and C. M. Marcus, Nonlocality of majorana modes in hybrid nanowires, Phys. Rev. B **98**, 085125 (2018).

[66] R. M. Lutchyn, E. P. A. M. Bakkers, L. P. Kouwenhoven, P. Krogstrup, C. M. Marcus, and Y. Oreg, Majorana zero modes in superconductor–semiconductor heterostructures, Nat. Rev. Mat. **3**, 52–68 (2018).

[67] Karsten Flensberg, Felix von Oppen, and Ady Stern, Engineered platforms for topological superconductivity and majorana zero modes, Nat. Rev. Mat. **6**, 944–958 (2021).

[68] Hao Zhang, Dong E. Liu, Michael Wimmer, and Leo P. Kouwenhoven, Next steps of quantum transport in majorana nanowire devices, Nature Communications **10**, 5128 (2019).

[69] Sasa Gazibegovic and et. al., Retraction note: Epitaxy of advanced nanowire quantum devices, Nature **604**, 786–786 (2022).

[70] Hao Zhang and et. al., Retraction note: Quantized majorana conductance, Nature **591**, E30–E30 (2021).

[71] Jennifer Sills and H. Holden Thorp, Editorial expression of concern, Science **373**, 500–500 (2021).

[72] Morteza Aghaee and et. al., Inas-al hybrid devices passing the topological gap protocol, arXiv 10.48550/arXiv.2207.02472 (2022).

[73] P. Jordan and E. Wigner, Über das paulische äquivalenzverbot, Zeitschrift für Physik **47**, 631–651 (1928).

[74] T. E. O'Brien, P. Rożek, and A. R. Akhmerov, Majorana-based fermionic quantum computation, Phys. Rev. Lett. **120**, 220504 (2018).

[75] Meng Cheng, Roman M. Lutchyn, and S. Das Sarma, Topological protection of majorana qubits, Phys. Rev. B **85**, 165124 (2012).

[76] Fei-Lei Xiong, Hon-Lam Lai, and Wei-Min Zhang, Manipulating majorana qubit states without braiding, Phys. Rev. B **104**, 205417 (2021).

[77] Daniel Litinski and Felix von Oppen, Braiding by majorana tracking and long-range cnot gates with color codes, Phys. Rev. B **96**, 205413 (2017).

[78] Alejandro M. Lobos, Roman M. Lutchyn, and S. Das Sarma, Interplay of disorder and interaction in majorana quantum wires, Phys. Rev. Lett. **109**, 146403 (2012).

[79] İ. Adagideli, M. Wimmer, and A. Teker, Effects of electron scattering on the topological properties of nanowires: Majorana fermions from disorder and superlattices, Phys. Rev. B **89**, 144506 (2014).

[80] Haining Pan and S. Das Sarma, Physical mechanisms for zero-bias conductance peaks in majorana nanowires, Phys. Rev. Res. **2**, 013377 (2020).

[81] Sankar Das Sarma and Haining Pan, Disorder-induced zero-bias peaks in majorana nanowires, Phys. Rev. B **103**, 195158 (2021).

[82] S. Das Sarma, Jay D. Sau, and Tudor D. Stanescu, Splitting of the zero-bias conductance peak as smoking gun evidence for the existence of the majorana mode in a superconductor-semiconductor nanowire, Phys. Rev. B **86**, 220506(R) (2012).

[83] S. Ostlund, Incommensurate and commensurate phases in asymmetric clock models, Phys. Rev. B **24**, 398–405 (1981).

[84] Iman Mahyaeh, Jurriaan Wouters, and Dirk Schuricht, Phase diagram of the $\mathbb{Z}_3$-Fock parafermion chain with pair hopping, SciPost Phys. Core **3**, 011 (2020).

[85] A. S. Mastiukova, D. V. Kurlov, V. Gritsev, and A. K. Fedorov, Free fock parafermions in the tight-binding model with dissipation, arXiv 10.48550/arXiv.2203.03554 (2022).

[86] Murod S. Bahovadinov, Wouter Buijsman, Aleksey K. Fedorov, Vladimir Gritsev, and Denis V. Kurlov, Many-body localization of $\mathbb{Z}_3$ fock parafermions, arXiv (2022).

[87] G. Camacho, J. Vahedi, D. Schuricht, and C. Karrasch, Disorder effects in the $\mathbb{Z}_3$-fock parafermion chain, arXiv 10.48550/arXiv.2210.02901 (2022).

[88] Fernando Iemini, Christophe Mora, and Leonardo Mazza, Topological phases of parafermions: A model with exactly solvable ground states, Phys. Rev. Lett. **118**, 170402 (2017).

[89] Shinsei Ryu, Andreas P Schnyder, Akira Furusaki, and Andreas W W Ludwig, Topological insulators and superconductors: tenfold way and dimensional hierarchy, New J. Phys. **12**, 065010 (2010).

[90] Florian Schäfer, Takeshi Fukuhara, Seiji Sugawa, Yosuke Takasu, and Yoshiro Takahashi, Tools for quantum simulation with ultracold atoms in optical lattices, Nature Reviews Physics **2**, 411–425 (2020).

[91] Aurélien Fabre, Jean-Baptiste Bouhiron, Tanish Satoor, Raphael Lopes, and Sylvain Nascimbene, Laughlin's topological charge pump in an atomic hall cylinder, Phys. Rev. Lett. **128**, 173202 (2022).

[92] Z. Iftikhar, A. Anthore, A. K. Mitchell, F. D. Parmentier, U. Gennser, A. Ouerghi, A. Cavanna, C. Mora, P. Simon, and F. Pierre, Tunable quantum criticality and super-ballistic transport in a "charge" kondo circuit, Science **360**, 1315–1320 (2018).

[93] T. K. T. Nguyen and M. N. Kiselev, Thermoelectric transport in a three-channel charge kondo circuit, Phys. Rev. Lett. **125**, 026801 (2020).

[94] Gil-Ho Lee, Ko-Fan Huang, Dmitri K. Efetov, Di S. Wei, Sean Hart, Takashi Taniguchi, Kenji Watanabe, Amir Yacoby, and Philip Kim, Inducing superconducting correlation in quantum hall edge states, Nat. Phys. **13**, 693–698 (2017).

[95] Yonatan Cohen, Yuval Ronen, Wenmin Yang, Daniel Banitt, Jinhong Park, Moty Heiblum, Alexander D. Mirlin, Yuval Gefen, and Vladimir Umansky, Synthesizing a ν=2/3 fractional quantum hall effect edge state from counter-propagating ν=1 and ν=1/3 states, Nat. Commun. **10**, 1920 (2019).

[96] M. Hashisaka, T. Jonckheere, T. Akiho, S. Sasaki, J. Rech, T. Martin, and K. Muraki, Andreev reflection of fractional quantum hall quasiparticles, Nat. Commun. **12**, 2794 (2021).

[97] P. Glidic, O. Maillet, A. Aassime, C. Piquard, A. Cavanna, U. Gennser, Y. Jin, A. Anthore, and F. Pierre, Cross-correlation investigation of anyon statistics in the $\nu = 1/3$ and 2/5 fractional quantum hall states, arXiv 10.48550/arXiv.2210.01054 (2022).

[98] R. B. Laughlin, Anomalous quantum hall effect: An incompressible quantum fluid with fractionally charged excitations, Phys. Rev. Lett. **50**, 1395–1398 (1983).

[99] L. Saminadayar, D. C. Glattli, Y. Jin, and B. Etienne, Observation of the $e/3$ fractionally charged laughlin quasiparticle, Phys. Rev. Lett. **79**, 2526–2529 (1997).

[100] X.G. Wen, *Quantum Field Theory of Many-Body Systems:From the Origin of Sound to an Origin of Light and Electrons: From the Origin of Sound to an Origin of Light and Electrons*, Oxford Graduate Texts (OUP Oxford, 2004).

[101] Maissam Barkeshli and Xiao-Liang Qi, Topological nematic states and non-abelian lattice dislocations, Phys. Rev. X **2**, 031013 (2012).

[102] Meng Cheng, Superconducting proximity effect on the edge of fractional topological insulators, Phys. Rev. B **86**, 195126 (2012).

[103] Torsten Karzig, Falko Pientka, Gil Refael, and Felix von Oppen, Shortcuts to non-abelian braiding, Phys. Rev. B **91**, 201102 (2015).

[104] T. Giamarchi and Oxford University Press, *Quantum Physics in One Dimension*, International Series of Monogr (Clarendon Press, 2004).

[105] A.O. Gogolin, A.A. Nersesyan, and A.M. Tsvelik, *Bosonization and Strongly Correlated Systems* (Cambridge University Press, 2004).

[106] Thomas L. Schmidt, Bosonization for fermions and parafermions, The European Physical Journal Special Topics **229**, 621–636 (2020).

[107] Martin Leijnse and Karsten Flensberg, Scheme to measure majorana fermion lifetimes using a quantum dot, Phys. Rev. B **84**, 140501(R) (2011).

[108] Dong E. Liu and Harold U. Baranger, Detecting a majorana-fermion zero mode using a quantum dot, Phys. Rev. B **84**, 201308(R) (2011).

[109] E. Vernek, P. H. Penteado, A. C. Seridonio, and J. C. Egues, Subtle leakage of a majorana mode into a quantum dot, Phys. Rev. B **89**, 165314 (2014).

[110] David A. Ruiz-Tijerina, E. Vernek, Luis G. G. V. Dias da Silva, and J. C. Egues, Interaction effects on a majorana zero mode leaking into a quantum dot, Phys. Rev. B **91**, 115435 (2015).

[111] Elsa Prada, Ramón Aguado, and Pablo San-Jose, Measuring majorana nonlocality and spin structure with a quantum dot, Phys. Rev. B **96**, 085418 (2017).

[112] Ida E. Nielsen, Karsten Flensberg, Reinhold Egger, and Michele Burrello, Readout of parafermionic states by transport measurements, Phys. Rev. Lett. **129**, 037703 (2022).

[113] Matthew Fishman, Steven R. White, and E. Miles Stoudenmire, The ITensor Software Library for Tensor Network Calculations, SciPost Phys. Codebases , 4 (2022).

[114] Qing-feng Sun and Hong Guo, Kondo resonance in a multiprobe quantum dot, Phys. Rev. B **64**, 153306 (2001).

[115] Roberto Bondesan and Thomas Quella, Topological and symmetry broken phases of z n parafermions in one dimension, J. Stat. Mech. **2013**, P10024 (2013).

[116] C. D. Batista and G. Ortiz, Generalized jordan-wigner transformations, Phys. Rev. Lett. **86**, 1082–1085 (2001).

[117] Ye Zhuang, Hitesh J. Changlani, Norm M. Tubman, and Taylor L. Hughes, Phase diagram of the Z_3 parafermionic chain with chiral interactions, Phys. Rev. B **92**, 035154 (2015).

[118] Z.-X. Gong, M. F. Maghrebi, A. Hu, M. L. Wall, M. Foss-Feig, and A. V. Gorshkov, Topological phases with long-range interactions, Phys. Rev. B **93**, 041102(R) (2016).

[119] Wing Chi Yu, Chen Cheng, and P. D. Sacramento, Energy bonds as correlators for long-range symmetry-protected topological models and models with long-range topological order, Phys. Rev. B **101**, 245131 (2020).

[120] I. P. McCulloch, Infinite size density matrix renormalization group, revisited, arXiv 10.48550/arXiv.0804.2509 (2008).

[121] Yin-Chen He, D. N. Sheng, and Yan Chen, Obtaining topological degenerate ground states by the density matrix renormalization group, Phys. Rev. B **89**, 075110 (2014).

[122] Takahiro Morimoto, Hiroshi Ueda, Tsutomu Momoi, and Akira Furusaki, F_3 symmetry-protected topological phases in the su(3) aklt model, Phys. Rev. B **90**, 235111 (2014).

[123] X. S. Wang, Arne Brataas, and Roberto E. Troncoso, Bosonic bott index and disorder-induced topological transitions of magnons, Phys. Rev. Lett. **125**, 217202 (2020).

[124] Wei Li, Andreas Weichselbaum, and Jan vonDelft, Identifying symmetry-protected topological order by entanglement entropy, Phys. Rev. B **88**, 245121 (2013).

[125] Sidney Coleman, *Aspects of Symmetry: Selected Erice Lectures* (Cambridge University Press, 1985).

[126] A I Vaĭnshteĭn, Valentin I Zakharov, Viktor A Novikov, and Mikhail A Shifman, ABC of instantons, Soviet Physics Uspekhi **25**, 195–215 (1982).

[127] R. Rajaraman, *Solitons and Instantons: An Introduction to Solitons and Instantons in Quantum Field Theory*, North-Holland personal library (North-Holland Publishing Company, 1982).

[128] Chun Chen and F. J. Burnell, Tunable splitting of the ground-state degeneracy in quasi-one-dimensional parafermion systems, Phys. Rev. Lett. **116**, 106405 (2016).

[129] Nicholas Manton and Paul Sutcliffe, *Topological Solitons*, Cambridge Monographs on Mathematical Physics (Cambridge University Press, 2004).

[130] Alexander Altland and Ben D. Simons, *Condensed Matter Field Theory*, 2nd ed. (Cambridge University Press, 2010).

[131] N.S. Manton, An effective lagrangian for solitons, Nucl. Phys. B **150**, 397–412 (1979).

[132] E.B. Bogomolny, Calculation of instanton-anti-instanton contributions in quantum mechanics, Phys. Lett. B **91**, 431–435 (1980).

[133] Jean Zinn-Justin and Ulrich D. Jentschura, Multi-instantons and exact results i: conjectures, wkb expansions, and instanton interactions, Ann. Phys. **313**, 197–267 (2004).

[134] Mithat Ünsal, Theta dependence, sign problems, and topological interference, Phys. Rev. D **86**, 105012 (2012).

[135] Tatsuhiro Misumi, Muneto Nitta, and Norisuke Sakai, Resurgence in sine-gordon quantum mechanics: exact agreement between multi-instantons and uniform wkb, J. High Energ. Phys. **2015** (9), 157.

[136] N. Regnault and Th. Jolicoeur, Quantum hall fractions for spinless bosons, Phys. Rev. B **69**, 235309 (2004).

[137] Iman Mahyaeh, Jurriaan Wouters, and Dirk Schuricht, Phase diagram of the z3-fock parafermion chain with pair hopping, SciPost Physics Core **3**, 011 (2020).

[138] Jurriaan Wouters, Fabian Hassler, Hosho Katsura, and Dirk Schuricht, Phase diagram of an extended parafermion chain, SciPost Physics Core **5**, 008 (2022).

[139] Z. Bajnok, L. Palla, G. Takács, and F. Wágner, The k -folded sine-gordon model in finite volume, Nucl. Phys. B **587**, 585–618 (2000).

[140] Chun Chen, *Topological Superconductivity And Superfluidity In Quasi-One-Dimensional Quantum Systems*, Ph.D. thesis, University of Minnesota (2017).

[141] Linas Bitkevicius, *Numerical Computation of the Mass of a Quantum Sine-Gordon Solitonin (1+1) dimensions*, Master's thesis, Imperial College London (2011).

[142] C. R. Dean, A. F. Young, P. Cadden-Zimansky, L. Wang, H. Ren, K. Watanabe, T. Taniguchi, P. Kim, J. Hone, and K. L. Shepard, Multicomponent fractional quantum hall effect in graphene, Nat. Phys. **7**, 693–696 (2011).

[143] A J Daley, C Kollath, U Schollwöck, and G Vidal, Time-dependent density-matrix renormalization-group using adaptive effective hilbert spaces, J. Stat. Mech. **2004**, P04005 (2004).

[144] Cheolhee Han, Zubair Iftikhar, Yaakov Kleeorin, Anne Anthore, Frédéric Pierre, Yigal Meir, Andrew K Mitchell, and Eran Sela, Fractional entropy of multichannel kondo systems from conductance-charge relations, Phys. Rev. Lett. **128**, 146803 (2022).

[145] Ian Affleck and Andreas W. W. Ludwig, Exact conformal-field-theory results on the multichannel kondo effect: Single-fermion green's function, self-energy, and resistivity, Phys. Rev. B **48**, 7297–7321 (1993).

[146] V. J. Emery and S. Kivelson, Mapping of the two-channel kondo problem to a resonant-level model, Phys. Rev. B **46**, 10812–10817 (1992).

[147] Pedro L. S. Lopes, I. Affleck, and E. Sela, Anyons in multichannel kondo systems, Phys. Rev. B **101**, 085141 (2020).

[148] Jan von Delft and Herbert Schoeller, Bosonization for beginners - refermionization for experts, Ann. der Physik **510**, 225–305 (1998).

[149] D. Sénéchal, An introduction to bosonization, eprint arXiv:cond-mat/9908262 (1999).

[150] E Miranda, Introduction to bosonization, Braz. J. Phys. **33**, 3–35 (2003).

[151] C. L. Kanel, Lectures on bosonization, eprint (2005).

[152] Liang Fu and C. L. Kane, Josephson current and noise at a superconductor/quantum-spin-hall-insulator/superconductor junction, Phys. Rev. B **79**, 161408 (2009).